Alma Mater Studiorum – Università di Bologna

DOTTORATO DI RICERCA IN

Scienze Biochimiche e Biotecnologiche

Ciclo XXIX

Settore Concorsuale di afferenza: 03/D1
Settore Scientifico disciplinare: CHIM/08

TITOLO TESI

Characterization of pharmaceutically relevant systems through surface plasmon resonance and circular dichroism spectroscopies

Presentata da: Edoardo Fabini

Coordinatore Dottorato

Prof. Santi Mario Spampinato

Relatore

Prof. Carlo Bertucci

Esame finale anno 2017

Characterization of pharmaceutically relevant systems through surface plasmon resonance and circular dichroism spectroscopies

Edoardo Fabini

“Only the atoms and the void are real”

– Democritus (460 – 370 BC.)

Contents

List of Publications

The present dissertation is based on the following papers:

I) E. Fabini, G. M. Lanchoti Fiori, D. Tedesco, N. P. Lopes, C. Bertucci. *Surface plasmon resonance and circular dichroism characterization of cucurbitacins binding to serum albumins for early pharmacokinetic profiling*.J. Pharm. Biomed. Anal. 122 (2016) 166–172. Doi: http://dx.doi.org/10.1016/j.jpba.2016.01.051.

II) E. Fabini, B. Zambelli, L. Mazzei, S. Ciurli, C. Bertucci. *Surface plasmon resonance and isothermal titration calorimetry to monitor the Ni(II)-dependent binding of Helicobacter pylori NikR to DNA*. Anal. Bioanal. Chem. (2016); 408(28): 7971–7980. Doi: 10.1007/s00216-016-9894-0.

III) D. Tedesco, E. Fabini, V. Barbakadze, M. Merlani, R. Zanasi, B. Chankvetadze and C. Bertucci. *Stopped-Flow Enantioselective HPLC-CD Analysis and TD-DFT Stereochemical Characterization of Methyl Trans-3-(3,4-Dimethoxyphenyl)Glycidate.* Chirality. (2015); 27(12): 914–8. Doi: 10.1002/chir.22539

IV) A. Peserico, A. Germani, P. Senese, A. J. B., V. Di Virgilio, R. Fittipaldi, E. Fabini, C. Bertucci, G. Varchi, M. P. Moyer, G. Carretti, A. Del Rio and C. Simone *A SMYD3 Small-Molecule Inhibitor Impairing Cancer Cell Growth.* J. Cell. Physiol. (2015); 230: 2447–2460. Doi: 10.1002/jcp.24975

V) C. Bertucci, D. Tedesco, E. Fabini, A. M. Di Pietra, F. Rossi, M. Garagnani, E. Del Borrello, V. Andrisano). *Determination of levamisole and tetramisole in seized cocaine samples by enantioselective high-performance liquid chromatography and circular dichroism detection.* J. Chrom. A (2014) 1363: 150–154. Doi: http://dx.doi.org/10.1016/j.chroma.2014.07.069

VI) U. H. Danielson, E. Fabini. *Monitoring drug-serum protein interactions for early ADME prediction through Surface Plasmon Resonance technology.* J. Pharm. Biomed. Anal. (2017). Accepted for publication 26 Mar 2017 Doi: 10.1016/j.jpba.2017.03.054

Articles were reprinted and adapted with permission from the publisher.

“I don’t know what I want but I know how to get it”

– Never mind the bollocks, here’s the Sex Pistol

Abstract

Studying biological interactions at a molecular level is crucial to rationally interpret pathophysiological conditions. Several analytical techniques have been engaged to elucidate different aspects of biological systems and, depending on the research question, medicinal chemists need to select the most tailored problem-solving approach. Among all possibilities, surface plasmon resonance (SPR) and circular dichroism (CD) spectroscopies offer intriguing potential. They can investigate both structural and functional aspects of biological targets and provide in return highly informative data output. In the present dissertation SPR and CD spectroscopies were employed to study different pharmaceutically relevant systems. The interaction between plant derivative Cucurbitacin, and serum albumins from different species (human and rat) was characterized with a combination of SPR direct binding assay and CD competition studies. Interestingly, two different binding profiles emerged. An extended SPR experimental set-up has been employed to investigate the interaction between the transcription factor from *Helycobacter pylori* NikR and the operator region of the urease promoter, revealing an isomerization of the protein–dsDNA complex occurring over time. SPR analysis was also employed to monitor the binding of Histone H4 residue to the methylation pocket of the epigenetic regulator SMYD3 in the presence of a selected small molecule (BCI-121). Results support *in silico* and *in cellulo* findings, confirming competition for the same binding site. CD detection was employed in combination with high performance liquid chromatography to achieve a full stereochemical characterization of Trans-3-(3,4-Dimethoxyphenyl)Glycidate enantiomers and to identify and quantify leva- and dexa-misole content in seized street cocaine samples. Studies reported in this dissertation highlighted how SPR and CD contribute to increase scientific knowledge on selected biological systems related to the field of life science. Moreover, assays developed here pose the basis for future inhibitors' screening, which could eventually lead to the discovery of new chemical entities endowed with therapeutic properties.

“*tune in, turn on, drop out”*

– Timothy Leary

Introduction

Introduction

New awareness in life science made us realize that complex, non-communicable, diseases cannot be described by simplified pharmacological models and, in many cases, correlation with unique ligand–receptor binding events results sub-optimal[1-3]. In this scenario, receptors can be regarded just as small effectors in a complex network of communication, and interactions with different ligands can either trigger or quench specific activities. Nonetheless, it is fair to state that drug discovery is still based on the profound knowledge of the biological system we want to modulate, and to the thorough inspection of the entire set of actors involved in the network. This is arguably the best strategy to produce a solid, rationally design, therapeutic strategy. Advancement in technology has made available for medicinal chemists increasingly sophisticated analytical techniques that allow detailed description of biomechanisms and biostructures. Therefore, among all options available, the operator has now to make the decision on how and when take advantage of the most appropriate methods to answer different questions across many biological systems.

Spectroscopy is the study of how matter interacts with any portion of the electromagnetic spectrum[4]. Scientists have been investigating for centuries how physicochemical environments influence electromagnetic radiations and different spectroscopic-based techniques have been developed. Among them, surface plasmon resonance (SPR) and circular dichroism (CD) offer intriguing experimental approaches for both structural and dynamic characterization. SPR-based analysis is steadily gaining recognition in both academia and industry in view of their versatility and highly informative data output. Typical analysis can detect thermodynamic and kinetic parameters of binding events employing just

few µg of biomaterial. CD spectroscopy is a well-established analytical technique for structural characterization of molecules either free or bound, in solution. In many cases can be considered the best option to elucidate binding modes, if crystals structures are not available.

The present dissertation includes a collection of experimental works in which SPR and CD were employed to elucidate significant aspects of pharmaceutically relevant systems. Basic concepts and principles of biochemistry and pharmaceutical analysis are also illustrated.

The introductive **Chapter 2** briefly describes how the concept of ligand–receptor interaction evolved during the last centuries, and how it has been linked to the insurgence of physiologic effects. Modern comprehension of living organisms prompted the birth of refined receptor theories able to better-forecast affinity–activity relationship with respect to classic models. These innovative approaches, take into consideration the complexity of the open-system physiology and the constant fluctuations of substances in different body compartments. However, no theory can be tested without analytical platforms able to directly measure quantities in a molecularly scaled system. To this scope, examples of the both classical and more recently developed analytical methodologies are illustrated in **chapter 3.** This latter introduces the main area of operation, structural and functional characterization of bioactive compounds, and will set the framework for the introduction of SPR and CD technologies. **Chapter 4** and **chapter 5** feature description of CD and SPR in term of detection principle, instrumentation available, experimental set up and data analysis. It is important to note that only information relevant for the experimental investigations included in this

dissertation are provided; while, for in depth description, readers are referred to excellent literature throughout the text.

Following the introductive section, the present dissertation will include extracts from studies published in peer-reviewed journals and will highlight how the state-of-the-art was taken over by further investigations through the analytical technologies SPR and CD. Original articles were adapted and reprinted with permission from the publishers. All SPR and CD results were obtained from experiments carried out during the course of the PhD program. However, each manuscript comprehends different analytical approaches and a complete description of all the trials performed will results out of the scope of the present dissertation. Nevertheless, they will be mentioned and commented to better frame how and where SPR and CD were employed. Readers that wish to consult material and methods for the analytical methodologies other than SPR and CD can directly refer to the original articles.

In the first extract, **chapter 6,** SPR biosensing and CD spectroscopy were employed to characterize the interaction of naturally occurring triterpenoids – Cucurbitacins – with serum albumin form different species for early ADME profiling. The binding of exogenous and endogenous compounds to serum proteins can impact their distribution volume, an issue that needs to be carefully assessed in translational medicine. Despite cucurbitacins can be considered as high affinity binders towards rat and human serum albumin, two different affinities and binding mode were identified in the two different species. **Chapter 7** includes an extensive SPR analysis of the interaction between the transcription factor from Helycobacter Pylori NikR and its dsDNA target sequence, the promoter region of the urease operator – OP_{ureA}. The extended experimental set-up employed, in combination

with isothermal titration calorimetry (ITC) data, resulted extremely useful to uncover a high affinity binding in the presence of Nickel in the environment. Moreover, the method developed could be useful to screen for inhibitors of a protein–DNA interaction, which are usually hard to screen for, thus they were previously defined as undruggable. In **chapter 8** a stopped-flow enantioselective high performance liquid chromatography-circular dichroism detection (HPLC-CD) methods was developed for the separation of methyl trans-3-(3,4-Dimethoxyphenyl) Glycidate enantiomers. Then, by combination with time-dependent density functional theory (TD-DFT) calculation, a full stereochemical characterization of the eluted fractions was achieved. The application of CD detection was also described in **chapter 10**, where levamisole and tetramisole presence in seized cocaine samples was revealed and quantified by the same experimental set-up. In this instance the selectivity of the detection method allowed monitoring dexamisole and levamisole in complex mixture as street drug samples. The extract presented in **chapter 9,** highlights the use of SPR biosensing to support molecular docking and *in cell* inhibition assay for an oncogenic target, SMYD3. In this study, a small molecule was selected through virtual screening and then tested for effectiveness in a selected cell line. The binding of the small molecule to SMYD3 methylation pocket was confirmed, indirectly, through a competition in solution assay.

Chapter 11 is a brief conclusion that will summarize all the findings and will indicate some of the future perspectives hinted by the present dissertation.

1. How *in vitro* affinity correlates with *in vivo* activity?

How *in vitro* affinity correlates with *in vivo* activity?

Every physiological and pathological effect stems from a well-defined interaction between two or more chemical entities. Humanity unconsciously knew this paradigm for millennia, and despite molecules were something far beyond knowledge in ancient times, it was known that assumption of natural products could produce well-defined physiological effects[5].

In his book from 1690 – Essay concerning human understanding – John Locke wrote:

> *'Did we but know the mechanical affections of the particles of rhubarb, hemlock, opium and a manywe should be able to tell beforehand that rhubarb will purge, hemlock kill and opium make a man sleepy…'*

now we can see that those 'mechanical affections' described by John Locke are nothing but the 'chemical interactions' as we intend them in the present days. However, neither description of their intrinsic nature nor comprehension of their mechanism of action was attempted.

The first breakthrough came from Emil Fisher in 1896, when he introduced the lock-and-key theory[6]. This model implies that pathophysiological effects are due to invisible microscopic events taking place within human body and these events are produced by the encounter of two physical entities granted with the same specificity and distinctiveness as the ones showed by the key and its lock. In 1908,

Paul Ehrlich coined the iconic expression *"corpora non agunt nisi fixata"*. This aphorism means "molecules can't exert their [physiological] effect unless they are [physically] bound [to the receptor]". Ehrlich conducted pioneeristic studies on arsenic derivatives for syphilis treatment; his research clearly proved that small chemical modifications of organic molecules could modulate both therapeutic and undesired effects, producing the first example of structure-activity relationship (SAR) study[7]. Following Ehrlich discoveries, in 1950, R. P. Stephenson formulated the first theoretic descriptions of biomolecular interactions. He introduced the concept of active and non-active conformation of an enzyme/receptor and discerned the *in vitro* binding affinity from the *in vivo* activity[8].

The groundwork of Fisher, Ehrlich, Stephenson and their contemporary colleagues, had provided medicinal chemists with a new, great, pharmacological tool: Equilibrium dissociation constant (K_D). K_D is by definition the concentration of ligand necessary to occupy 50 % of receptor population in a steady state condition that is when the total concentration of each reactant remains constant over time. It is considered the cornerstone of drug discovery: the tighter the ligand binds its target in an *in vitro* assay, the higher its efficacy can be in an *in vivo* system. Similarly, steady state inhibition constant K_i and parameter IC_{50} describe the half-maximal inhibitory concentration in enzymatic assays, in which dimming of a given biological activity is monitored while sequentially adding inhibitor at increasing concentrations.

Major goal for medicinal chemists can be considered the identification, either from natural compounds or commercially available databases, of favorite molecular structure able to bind the desired target with low-to-moderate affinity.

Subsequently, through synthetic chemistry the scaffold is modified in order to achieve higher efficient binders to bring to pre-clinical and clinical trials. During this process the guidelight is K_D (or K_i) value for the ligand–analyte complex; increasing stability indicates modifications improved binding efficiency and could potentially improved *in vivo* activity.

However, despite being the *conditio sine qua non* for efficacy, K_D and K_i values measured for several bimolecular complexes fails to quantitatively correlate with *in vivo* activity, and the relationship observed in many cases is rather qualitative[9] (Fig. 1a). This ambiguous behavior can be sought in the nature of physiological systems; there is no body compartment, no tissue nor cells that rests in a perfect steady state condition. Physiology is a dynamic process, and we know that drug concentration fluctuates both locally and globally within human body.

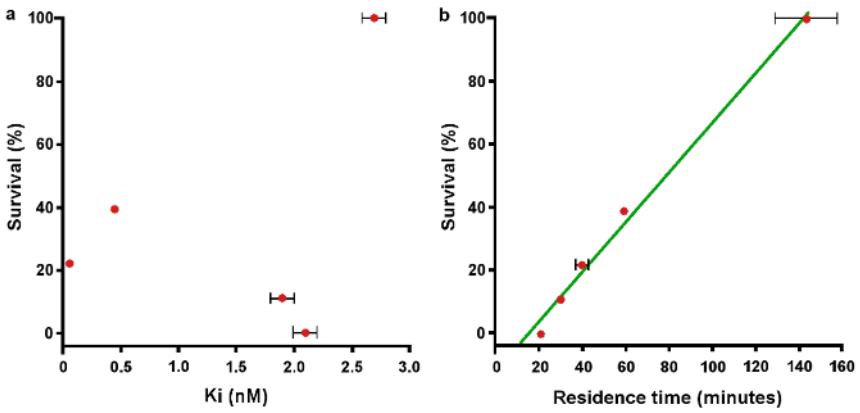

Figure 1 | In vivo efficacy often depends on drug-target residence time. The relationship between the residence time of a series of FabI enoyl-reductase inhibitors and in vivo activity. The plots presented here show the percent survival of mice 10 days after they were infected with the bacterium Francisella tularensis and then treated with the inhibitors. **a** | Correlation of percent survival with the inhibition constant (*Ki*). **b** | Correlation of percent survival with inhibitor residence time. (Figure is adapted with permission from ref [10]).

Once entered circulatory stream, compounds undergo a complex network of interactions that comprehend many different binding partners along with the primary one. In the open system of *in vivo* pharmacology (Fig. 2b), multiple steps such as absorption, distribution and clearance affect the local concentration of ligand that arrives at the receptor-harboring tissue and consequently the rate of encounter with its primary target[10]. Therefore, individual rate constants defining the steady state affinity value ($K_D = k_{off} / k_{on}$) acquire new significance, and dissociative half-lives of the multiple complexes need to be assessed and interpreted.

K_D values are usually determined in closed systems (Fig. 2a); therefore, the time-dependent variation of compound concentration is not always taken into account. Residence time (τ) can provides further insight on the affinity–activity relationship. τ expresses the time ligand is associated with the receptor and can be directly obtained as the reciprocal function of the dissociation rate constant ($\tau = 1/k_{off}$) of a bimolecular complex (Fig. 2c). It has been demonstrated that for many biological systems, τ better describes the *in vivo* potency of a drug with respect to steady state affinity measurements[9, 10] (Fig 1b). Slow dissociating complexes can exists beyond the complete excretion of the ligand from the body and the related physiological effect can lengthen considerably; moreover, in many cases higher τ reflects higher selectivity thus less toxicity. Excellent materials reporting the significance of residence time for efficacy and selectivity can be found in many excellent articles throughout the literature[11-15]. Residence time gains even more relevance when receptor isomerization is considered. In this situation after the first encounter between the two binding partners to form the first complex ($R + L \Rightarrow RL$), a rearrangement leads to a more stable conformation ($RL \Rightarrow RL^*$) that cannot

directly dissociates into the first two interactants. In this case, the term k_{off} is composed of microscopic rate constants associated with both forward and reverse steps in receptor isomerization, $k_{off} = k_{off1}k_{off2}/(k_{off1} + k_{on2} + k_{off2})$[10] (Fig 2d).

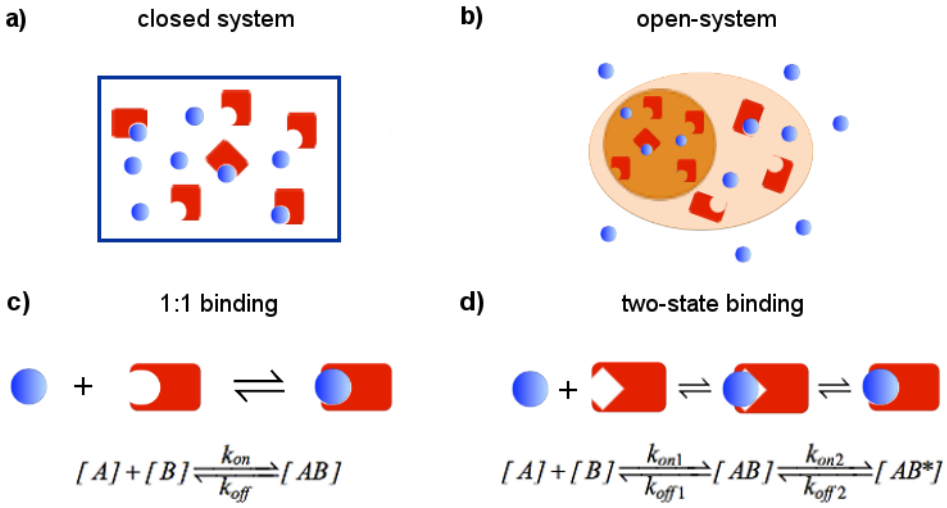

Figure 2 | Representative illustration of ligand–receptor kinetic interactions. Receptor is depicted as a red square and the ligand as a blue circle. (**a**) In a closed system concentration of all interactants remain constant over the time required for the experiment, therefore a real condition of equilibrium can be established. (**b**) Conversely, in the open-system, fluctuation dominates and distribution, metabolism, and clearance all affect the concentration of drug in the receptor-harboring tissue. This does not allow reaching a true steady-state condition. (**c**) Classic scheme of a reversible 1:1 binding mechanism, with associated forward and backwards reaction constants k_{on} and k_{off}. (**d**) Scheme for a two-step binding mechanism, where receptor isomerization occurs. Two additional forward/backward rate constants are present, k_{on2} and k_{off2}, that accounts for the conformational switch of the bimolecular complex.

This behavior was detected while studying the interaction between the transcription factor from *helycobacter pylori* – *Hp*NikR and the dsDNA of the urease operator – OP_{ureA} (*see chapter 7*). Upon binding to OP_{ureA} in presence of four Ni(II) equivalents, *Hp*NikR showed a behavior consistent with an induced-fit

mechanism, where its structure rearranges over time to form a more stable complex with the dsDNA sequence. The conformational rearrangement of the *Hp*NikR– OP_{urea} complex over time was linked to a physiologic adjustment of the bacteria to high Nickel content in the environment[16].

Nevertheless, no chemical interaction can be seen by unaided eye, and analytical techniques are necessary to directly or indirectly interrogate binding events at molecular level.

3. Analytical techniques allow structural and functional characterization of biological systems

Analytical techniques allow structural and functional characterization of biological systems

Biological systems have always being questioned through different approaches. The common objective is to identify specific features of the target and define its biological role in a precise network of communications. Afterwards, pharmacological hypothesis are proposed and scrupulous experiments are designed to test their consistency. From data analysis, structure-activity relationships are sketched and iterative processes of trials and errors can eventually lead to the discovery of new chemical entities endowed with therapeutic properties.

The advent of molecular biology freed scientists from the burden of laboriously collect milligrams of bioactive materials from living organisms able to spontaneously create it. Current technology allows biological targets to be efficiently produced and retrieved from engineered microorganisms programmed to express determined exogenetic material[17-19]. Pharmaceutical science greatly benefited from this revolution and at present day, in many instances, we possess enough material so that detailed bioanalyses can be carried out.

Biological targets can be scrutinized at different levels; however, we can mainly profile their structural and functional features. Structural characterizations aim to define the tridimensional space of macromolecules, so structure-based drug discovery can be carried out. In this scenario, analytical techniques usually capture snap-shots of the receptor/enzyme alone or in combination with endogenous/exogenous ligands. The insight they provide can guide modifications of chemical scaffolds, based on new hot spots discovered within binding sites, or aids to rationalize biorecognition events through visualization of chemical environments.

On the other hand, functional characterization aims to profile their behavior with respect to the interaction with different binding partners. Initial biorecognition studies are usually carried out in cell-free assays to define thermodynamic and kinetic parameters of the ligand–receptor reaction. Subsequently, same binding events are probed on *in vivo* systems, to check for translation of primary affinity into a more physiologically-like setting.

Throughout the years a vast plethora of analytical approaches have been employed for structural and functional characterization. Each technique is engaged to uncover specific aspects of the biorecognition process and early drug discovery undoubtedly benefits from their complementary and synergy. As a representative sample of all the available options it worth to mention equilibrium dialysis[20-22], analytical ultracentrifugation[23, 24], ultrafiltration[25], affinity capillary electrophoresis (ACE)[26, 27], nuclear magnetic resonance (NMR)[28-30], circular dichroism (CD)[31-34] and fluorescence spectroscopies[35-37], quartz crystal microbalance (QCM)[38, 39], high-performance affinity liquid chromatography (HPALC)[40, 41], X-ray crystallography [42, 43], mass spectrometry (MS)[44-46], small angle light scattering (SAXS)[47], surface acoustic wave (SAW)[48] and surface plasmon resonance (SPR)-based biosensors[49-51], isothermal titration calorimetry (ITC)[52-54], cryo-electronic microscopy (cryo-EM)[55, 56] and microscale thermophoresis (MST)[57-59].

X-ray crystallography can be considered the chief technique in the structural field. It has been successfully employed for the structural characterization of thousands of biomolecular structures and for the establishment of modes of action of many ligand–receptor systems[43]. Recently, cryo-EM has emerged as an alternative approach[56]. Cryo-EM measures electron diffraction patterns of biomolecules embedded in a cryogenic media, without requiring pre-staining or

fixation of any kind. Therefore, images can be collected in specimen natural environments without risking alteration of the overall molecular structure. Also MS has been employed to resolve many macromolecular structures both at the primary and at higher orders; moreover, combination with limited proteases digestion enables identification of unknown protein through fragments analysis[45].

For thermodynamic characterization, ITC is considered the most suited technique in view of its ability to directly measure enthalpy (ΔH) of ligand–receptor binding events and stoichiometry (n) and stability (K_D) of binary complexes in solution. The heat released or absorbed during a reaction is measured upon titration of one of the two interactants, usually protein or DNA, with increasing concentration of the other, usually a small organic molecule. Nonetheless, it requires high material consumption a condition that is not always easy to achieve during early stages of drug discovery[54]. MST can characterize ligand–receptor affinity in a vast array of situations including solubilized membrane proteins, provided that on of the two binding partners is fluorescently labeled or intrinsically fluorescent. Measurements are directly related to the movement of particles in a thermal gradient: every shift due to the variation of hydrodynamic range or to a conformational rearrangement upon association between molecules can be detected and used to quantify binding events[57]. Other techniques such as SPR, QCM and SAW allow extrapolation of reactions kinetic parameters applying continuous flow of analyte/buffer over an immobilized interactant[60, 61]. They all possess the ability to detect interactions in real-time, generating association/dissociation traces that can be analyzed through application of theoretic binding models. Each technology exploits different physical transducers: SPR monitors the shift of refractivity at the surface of a biosensor chip, QCM measures changes in the vibration frequency of a quartz crystal and

SAW detect perturbation in frequency and amplitude of acoustic waves. As common features they quantified K_D, k_{on}, k_{off} and thermodynamic parameters.

More recently, *in silico* techniques started providing additional tools for both structural and functional studies. Computational chemistry can be employed to simulate 3D environments of proteins and calculate free energy of reactions, hence aiding to understand biomechanisms and prioritize favorite chemical structures[62-64]. Whenever dealing with huge libraries of molecules, as in the present era of combinatorial chemistry and fragment-based drug discovery, virtual screening can drastically reduce time needed for optimization of compounds, easing the rational-design of molecules by synthetic chemists[65].

Circular dichroism (CD) and surface plasmon resonance (SPR) spectroscopies are two detection methods particularly intriguing for biochemical analyses; they can provide both structural and functional information depending on the experimental set up employed for the study. SPR detection emerged as an efficient approach to obtain large amounts of information about binding processes. Simple, automated and fast assays provide good throughput, versatility and highly informative data output, rendering the methodology particularly suited for early drug discovery[61]. CD analysis can be considered the élite technology to study conformation of bioactive molecules in solution either bound or free. Intrinsic chirality of nature lends well itself to CD analysis; asymmetric disposition of atoms can be interrogated to elucidate binding modes and stereoselectivity, even when previous crystal structure or *in silico* models are not available[66].

In the following sections, these two analytical methodologies are presented in details and their principal features thoroughly described.

4. Circular dichroism spectroscopy (CD)

Detection principle

The branch of spectroscopy that studies the interaction of ultraviolet and visible light with matter is called UV-vis spectroscopy and energy of the associated electromagnetic radiation is responsible for transitions of electrons from ground states to excited states[67-70] (Fig 3).

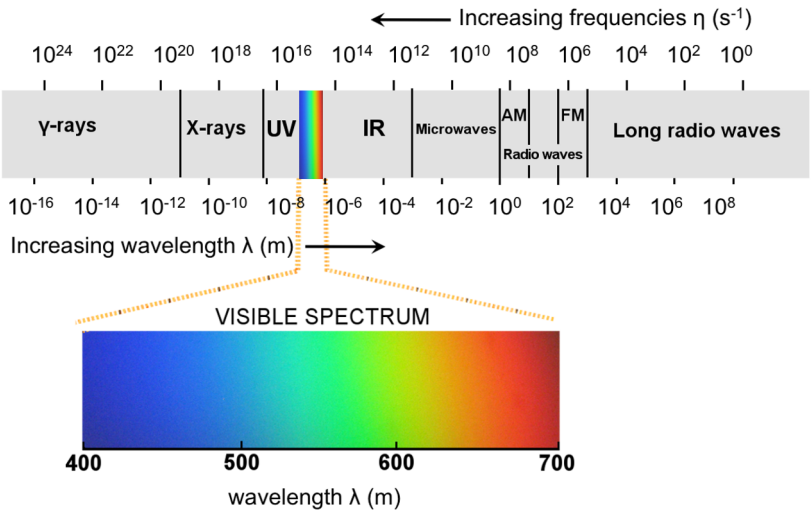

Figure 3 | Graphical representation of the whole electromagnetic spectrum. The colored inset depicts the region where visible light is located. Different molecular transitions are associated with different energies: **γ-rays** nuclear, **x-rays** core level electrons; **UV-vis** valence electrons; **IR=infrared** molecular vibrations; **Microwaves** molecular rotations, electron spin; **Radio waves** nuclear spin; (Adapted with permission from ref [67]).

According to quantum theory, only specific groups of atom posses the correct spatial arrangement to interact with UV-vis light and only some specific electronic transitions in them are allowed. Chemical groups possessing these specific features are defined chromophores and are responsible of colors displayed by organic and inorganic molecules.

Usually, light sources as the sun or incandescent light bulbs, generate unpolarized electromagnetic radiation, meaning they produce an incoherent random mixture of transverse waves (Electric and Magnetic) propagating in space with multiple frequencies, wavelengths and directions. Some devices, defined polarizers, can polarize the electromagnetic radiation to the extent it propagates only in one direction, i.e. oscillates only over one plane[71, 72] (Fig. 4).

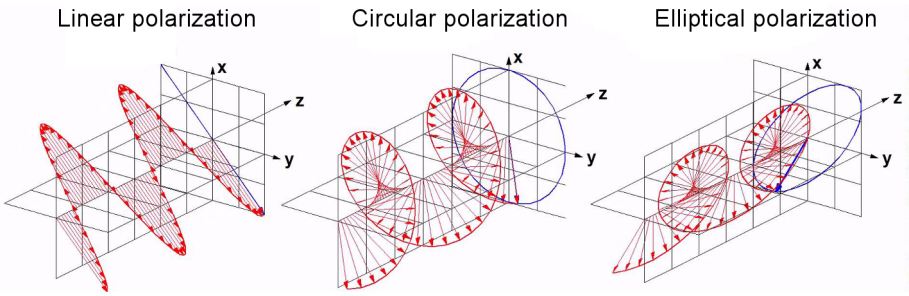

Figure 4 | Depiction of the electronic component of the electromagnetic radiation propagating in space. Linear, circular and elliptical polarization states are presented.

Circular polarization is a polarization state wherein the electric field of the wave has a constant magnitude but its direction rotates in a fix plane perpendicular to the direction of the wave propagation[73] (Fig 4). The rate of this rotation remains constant in time, and the shape of the resulting light vector describes a helix. Circularly polarized light can be right-handed circularly polarized light, if the vector rotates clockwise, or left-handed circularly polarized light if the vector rotates counterclockwise, with respect to an observer towards which the light is directed.

Linearly polarized light is usually produced by combination of two perpendicular electromagnetic waves of the same amplitude and frequency

propagating in phase relative to one another. Optical elements, termed quarter-wave plate, are able to converts linearly polarized light in circularly polarized light, and vice versa[74]. In a quarter-wave plate, one of the linear components of the beam will slow with respect to the other, so that they are one quarter-wave out of phase and a beam of either left- or right-circularly polarized light is produced.

When right and left circularly polarized lights are shone through a transparent chamber containing a chiral sample, they can be absorbed differently due to the intrinsic asymmetry of atoms disposition in the molecule[73]. Direct measurements of the unequal absorption produce CD spectra, while measuring the ellipticity [θ] of the emerging light results in optical rotatory dispersion spectra (ORD).

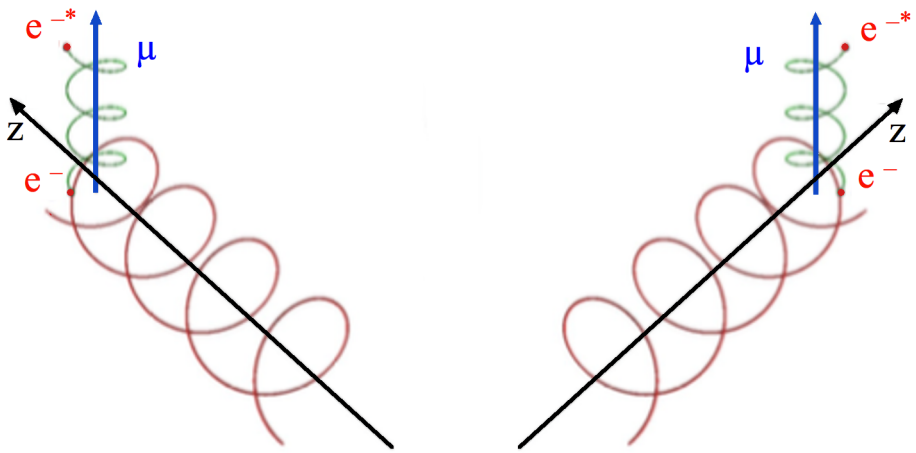

Figure 5 | Graphical representation of the interaction of light with a helical charge displacement. (redesigned from ref. [75]). (**a**) Left-handed helical charge displacement interacts preferentially with right circularly polarized light resulting in negative CD. (**b**) Right-handed helical charge displacement interacts preferentially with left circularly polarized light resulting in positive CD.

The different interaction, at atomic level, resides in the charge displacement upon absorption of the radiation (Fig. 5). The motion of the excited electrons from the ground state to the excited state generates a helical electric field that can be left or right handed depending on the spatial arrangement of atoms around the chromophore. Circularly polarized light has a similarly helical electric field, and preferential interactions occur between the two helical fields: left handed charge displacement interacts preferentially with right circularly polarized light, right handed charge displacement with left circularly polarized light[75] (Fig. 5).

AS a consequence, CD spectra of pure enantiomers differ in sign, but not in magnitude, while non-chiral molecules or racemic mixtures will not show any CD signal[73, 76] (Fig. 6).

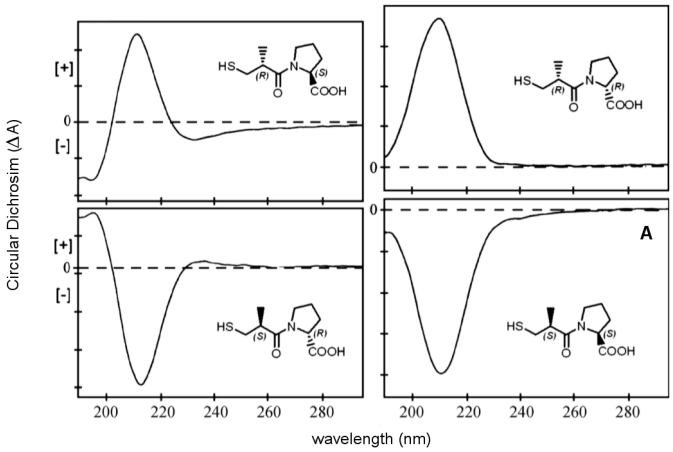

Figure 6 | Representative CD spectra of captopril A (1-[(2S) 3-mercapto-2-methylpropionyl]-(S)-proline) **and its stereoisomers**. A clear mirror-image relationship between absorption bands appear for the two couple of enantiomers. Adapted and modified from Ref [76].

Lambert-Beer law describes the differential absorption of right and left circularly polarized light:

$$\Delta A = A_L - A_R = \varepsilon_L cl - \varepsilon_R cl = (\varepsilon_L - \varepsilon_R)cl = \Delta\varepsilon cl \qquad (1)$$

where $\Delta\varepsilon$ is the molar differential extinction coefficient. ORD and CD have the same quantum information content; therefore, $\Delta\varepsilon$ and $\theta°$ are intimately connected according to the relationship:

$$[\theta] \cong 3300\,\Delta\varepsilon \qquad (2)$$

A CD spectrum is the plot of $\Delta\varepsilon$ over a range of wavelengths while ORD is the plot of the ellipticity. Both of them provide valuable insight on chirality; yet, the former is by far the most employed in view of its lower tendency to be affected by light artifacts and its direct wavelengths-correspondence with absorption bands. Although CD phenomenon can occur throughout the entire spectra of electromagnetic radiation, the ones related to valence electrons absorption are the most relevant to the study of organic molecules. This form of circular dichroism is defined as electronic circular dichroism (ECD).

Instrumentation

Spectropolarimeters are the instruments employed to assess chiral properties of molecules. They are derived from classic spectrophotomers with the addition of devices suited for the production, modulation and detection of circularly polarized light. In principle, a CD spectrum of a molecule can be measured in two separate

experiments: the sample is irradiated first with one and then with the other beam of circularly polarized light, and the differential absorption is recorded. However, from an experimental point of view, the best mode is through polarization modulation[77]. With this technique circularly polarized light, is gradually switched through all the ellipticities between 0 ° and ± 180°, through harmonic variations of the potential alternate current (AC) voltage on electro-optic modulators. This modulator is inserted into the workflow of the spectropolarimeter**,** before the sample chamber. The other typical components of a spectroplarimeter are described below:

• Light source: generally a combination of deuterium and tungsten lamps, able to produce light ranging from 150 nm up to 800 nm.

• Monochromator: usually a prism or a diffraction grating that allows the passage of only a narrow wavelength range (called spectral bandwidth). The orientation of the prism/grating dictates the wavelength of the emerging light.

• Polarizer: usually a Rochon polarizer producing pure polarized light.

• Photon electron modulator: through application of alternate current voltage modulates the handedness of the circularly polarized light directed to the sample chamber.

• Sample chamber: Cells made of fused silica to circumvent the UV-absorbing impurities of glass. This area can be thermostated.

• Detector: usually a photomultiplier or a photodiode array device, whose signals are amplified and directed to a recorder or computer. Absorbance data are processed as a function of incident wavelength to give an absorption spectrum.

A graphical representation is shown in figure 7.

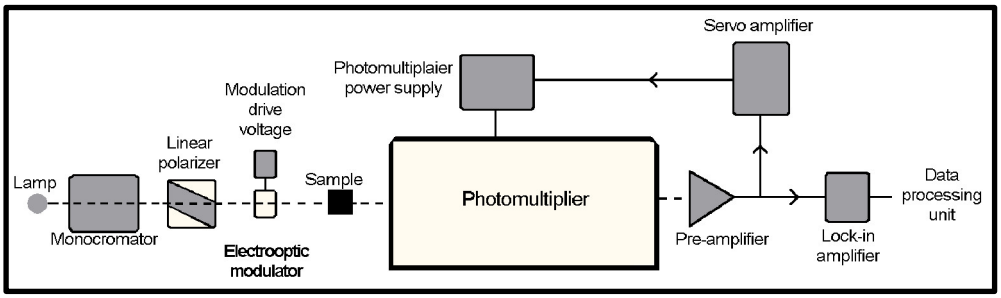

Figure 7 Graphical representation of a spectropolarimeter. (Adapted from reference [77]).

Experimental set-up

CD effects are strictly related to UV-vis light absorption of the sample; therefore experimental optimizations aim to minimize artifacts arising from other sources of absorption, dispersion and diffraction of the incident light.

The utmost consideration should be given to the sample composition. Firstly, chemical species need to be fully solubilized; if otherwise, recorded absorbance might be due to light scattering, i.e. events related to the fine dispersion of particles in solution rather then electronic transition in the chromophore moisture[68, 78]. Then, it is important to choose the proper buffer. As general rule, buffer composition should be kept as simple as possible, however in some circumstances additives cannot be left out. Small organic molecules might demand non-polar solvents to

aid solubilization, while biomolecules, as proteins and DNA, usually need salts and proper buffering agents. Requirements are more flexible for small molecules, while it is sometimes impossible to remove precise components from macromolecules media if their functionality wants to be preserved. As far as the protein is the main concern some alternatives can be explored, and salt and buffer might be changed to favor spectroscopic properties[79]. Spectroscopic contribution of common buffers and salts are reported in table 1.

Since absorbance is governed by the Lambert-beer law, its amplitude can be modulated according to the length (l) of the sample cell. If this parameter is reduced sufficiently, and the protein concentration can be kept high enough, problems due to solvent absorption might be overcome. Additionally, the range of wavelength for the measurement has to be carefully assessed according to the chromophore we want to excite. Different chemical groups absorb in different regions of the UV-vis spectra, therefore different structural features are probed at different energies.

	Absorbance (50 mM solution in 0.02 cm pathlength)			
COMPONENT	180 nm	190 nm	200 nm	210 nm
NaCl	> 0.5	> 0.5	0.02	0
NaF	0	0	0	0
$NaClO_4$	0	0	0	0
Boric acid	0	0	0	0
Na borate (pH 9.1)	0.3	0.09	0	0
Na_2HPO_4	> 0.5	> 0.3	0.05	0
NaH_2PO_4	0.15	0.01	0	0
Na acetate	> 0.5	> 0.5	0.17	0.03
Tris/H_2SO_4 (pH 8.0)	> 0.5	0.24	0.13	0.02
HEPES/Na^+(pH 7.5)	> 0.5	> 0.5	0.5	0.37
MES/Na^+(pH 6.0)	> 0.5	0.29	0.29	0.07

Table 1. Absorption of selected buffer components in the UV region. (Data from ref [79]).

However, it is difficult to make measurements much below 190 nm, partly because the intensity of the radiation falls off in this region, but also because N_2 used for purging the sample compartment, optical devices and aqueous solvents absorb significantly[78].

To check how strongly the chemical environment contributes to the overall absorbance, a blank sample, containing all but the molecules whose absorption wants to be measured, is run before the actual measurement take place.

Along with sample-related considerations, also instrument setting can improve quality of the CD analysis. Parameters that can be adjusted are listed below:

• Bandwidth: The bandwidth is a measure of the precision with which a monochromator selects light of a chosen wavelength. Increasing the bandwidth will allow more light to fall on the sample and hence on the photomultiplier, but will decrease the ability to resolve spectral bands. The bandwidth should be less than or equal to 1 nm for routine CD studies, but values down to 0.1 nm are useful, particularly to resolve fine structure in the near UV spectrum of proteins.

• Time constant and scan rate: The time constant is a measure of the time over which the CD data are averaged and will depend on the precise mode of operation of the instrument.

• Number of scans: Increasing the number of scans will improve the signal/noise (S/N) ratio; the S/N ratio is proportional to the square root of the number of scans.

However, a universal guideline can't be proposed, and parameters needs to be set on case-by-case basis, taking into account any limitations imposed by the stability of the sample under the conditions employed, and the performances of the instrument.

One relevant experimental set up concerning CD spectroscopy is its combination with liquid chromatography (HPLC-CD), as experimentally illustrated in the present dissertation (*chapter 10*) and in literature[80-82]. The hyphenation of a separation technique (HPLC) with a chiral detection system (CD), allows recognition of optically active samples among crowded UV-absorbing mixtures. This methodology was successfully employed to determine the enantiomeric composition of tetramisole enantiomers in seized cocaine samples, where the direct selective monitoring of levamisole and dexamisole through CD detection was enabled even in the presence of possible interferences[81].

Moreover, HPLC-CD system offers the possibility to exploit on-line detection approach. This is achieved by trapping a chromatographic peak into a tailored CD sample chamber so that its CD spectrum can be measured over a range of wavelengths. This provides a valuable analytical tool that allows determination of CD spectra for compounds directly eluting from a chromatographic run and avoid the time-consuming step of collecting and dry out pure enantiomers for complete CD characterization. This latter approach revealed its suitability for the stereochemical characterization of different chemical species and in the present dissertation was applied to elucidate chirooptic properties of trans-glycidate enantiomers [82, 83] *(see chapter 8)*.

Data output and analysis

Generally, a CD signal will be detected if a molecule shows chiral features, i.e. the molecule is optically active[84]. Reasons behind optical activity can be one of the following:

• A chromophore is intrinsically chiral because of its chemical structure. For instance a Carbon atom with 4 different substituents

• The chromophore is covalently bound to a chiral centre in the molecule

• The chromophore lies in an asymmetric environment dictated by the overall structure of the molecule.

All these properties cause the electronic transition from the ground states to the excited states to be affected by an asymmetric disposition of electronic clouds in

the chemical environment; hence, chiral light beams (helices light vectors show their own chirality) will favor some transitions over others.

CD will appear in correspondence of absorption bands; therefore, they are easily ascribed to specific chromophoric groups. For instance, peptide bond absorbs below 240 nm ($\pi \rightarrow \pi^*$ transition centered around 190 nm and $n \rightarrow \pi^*$ transition around 220 nm), aromatic amino acid absorbs in the range 260 – 320 nm, and other coordinated systems found in many organic molecules such as flavons and chlorophyll will absorbs up to the near infrared region. Generally, the wider is the coordinate system of chromophores, the longer will be the wavelength of absorption (Benzene 255nm, Naphthalene 286nm, Anthracene 375nm; Naphthacene 477nm)[68].

Chirality is intrinsically related to bioactive molecules: life building blocks and actuators are very often chiral such as L-aminoacids and D-sugars. As a result, macromolecules will show their own chiral signatures, due to the highly ordered 3D disposition of small chiral blocks in the macromolecules' structure[85, 86]. CD spectra and X-ray crystals for several proteins have been obtained and correlated, so that many CD reference databases are now available. By means of algorithms, these databases can be consulted to quantitatively estimated content of secondary structures from the CD spectra measured in solution[85, 87]. CD spectra aroused by common secondary structures habitually found in protein are displayed in figure 8.

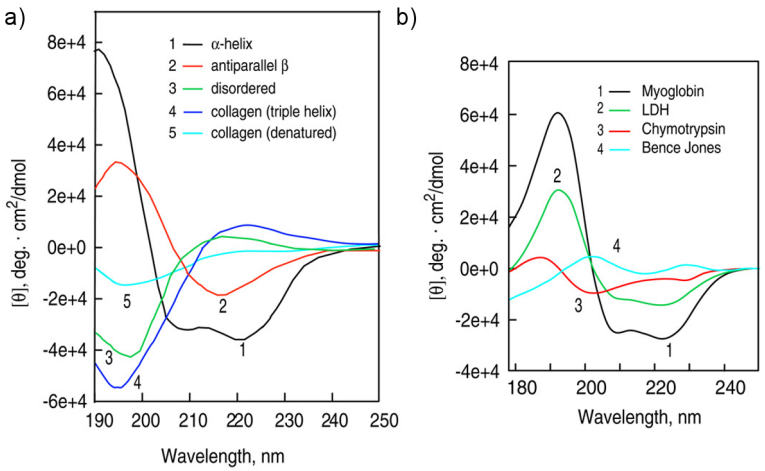

Figure 8 | (**a**) CD spectra of poly-L-lysine and placental collagen in different conformations. poly-L-lysine: 1 (black) α-helical; 2 (red) antiparallel β-sheet; 3 (green) extended conformations. Placental collagen: 4 (blue) native triple-helical and 5 (cyan) denatured forms. (**b**) CD spectra of representative proteins with varying conformations: 1 (black) sperm whale myoglobin; 2 (green) chicken heart lactate dehydrogenase; 3 (red) bovine α-chymotrypsin and 4 (cyan) human Bence Jones protein REI light chain, which is a human immunoglobulin light chain of κ type. (Reprinted with permission from ref. [87]).

Despite main application area for secondary structures analysis can be considered quality control of protein production (batch-to-batch assessment of protein folding), it can also provide valuable information on biologic processes.

In the wake of some diseases, crucial proteins can mutate their physiologic folding and pathologic conditions can emerge. This was observed for the Amyloid beta protein that switches its conformation from mainly alpha-helix to mainly beta-sheets in high-water-content media over time[88] or the refolding of prion proteins induced by phosphorilation[89]. Monitoring these events in the presence or absence of specific compounds can indicate if any delay in the conformational switched occurred, thus forecasting therapeutic properties[90].

Other molecules that do not normally show CD spectra, can gain optical activity if constrained into a fixed conformation due for example to the inclusion into a chiral protein binding site. This peculiar form of CD is defined as induced circular dichroism (ICD) and can be a useful tool for monitoring ligand–receptor binding events[91] (Fig. 9). Non-chiral molecules that gain ICD upon specific binding with proteins can be employed as markers for that binding site, and their ICD can be monitored to extrapolate unique information on the absolute configuration of chiral molecules as well as the orientation of molecules relative to each other within the host-guest complex[66, 92, 93].

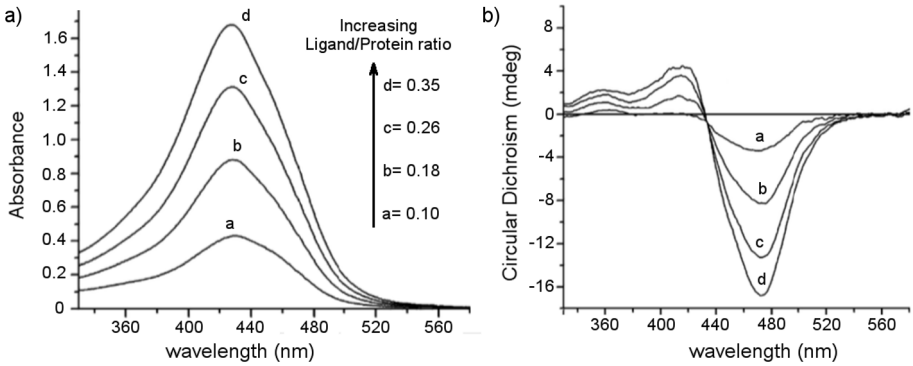

Figure 9 | Example of induced circular dichroism (ICD). UV/vis (**a**) and circular dichroism (**b**) spectra of curcumin–AGP complex in solution at different ligand/protein ratios (cell length 1 cm, conentration of AGP 130 μM, T= 15 °C). Ligand protein rations are indicated in the figure. The more curcumine bounds to AGP to form the complex, the greater the intenstity if the ICD bands become. Reprinted and adapted with permission from ref [92].

Moreover, careful data analysis can provide invaluable tool to determine binding strength and direct or indirect competition for a determined binding site. This approach was particularly useful for the characterization of Cucurbitacins–Serum albumin molecular interaction *(see chapter 6)*[94] where two different binding

modes were identified for the triterpenoids binding to serum protein from rat and human. This behavior is an indication of a potential different pharmacokinetic profile of the compound when tested in different animal models, an issue that needs to be carefully assessed in translational medicine.

Finally, it is important to mention that combination of experimental CD analysis with quantum chemical calculations, based on time-dependent density functional theory (TD-DFT), can provide additional information on stereochemistry[82]. UV and CD spectra can be predicted through *in silico* analysis and compared to experimental measurements to assign absolute configurations to CD profiles. This method demonstrates to be valid over a wide range of bioactive molecules and in this dissertation resulted useful for the assignment of the absolute configuration of two enantiomers contained in samples obtained from root extracts of different species of comfrey and bugloss *(see chapter 8)*.

5. Surface plasmon resonance spectroscopy

This chapter is based on: H. U. Danielson, **E. Fabini** "Monitoring drug–serum proteins interaction for early ADME prediction through Surface Plasmon Resonance based technology" (2017) Journal of Pharmaceutical and Biomedical Analysis – Accepted for publication 26 Mar 2017–

Doi: 10.1016/j.jpba.2017.03.054

Detection principle and optical configuration

The optical phenomenon of SPR occurs when a beam of plane-polarized light hits the surface of a thin, electron-rich, metal layer placed at the interface between two media of different refractive indices ($n_1 \neq n_2$)[95]. At a specific angle of incidence (θ), under condition of total internal reflection (TIR), the photons of the light are able to excite the (nearly) free electron gas of the metal, causing excitation of surface plasmons. This plasmon state is a highly delocalized state resulting in a resonant, non-radiative, wave at the interface between the metal and the dielectric medium[95] (Fig 10).

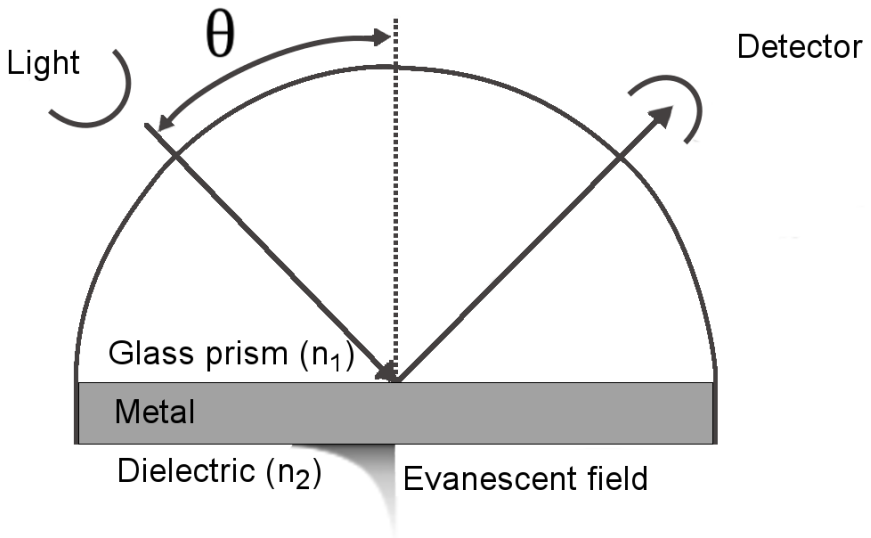

Figure 10. Illustration of optical configuration for the excitation of surface plasmons in metals (the configuration illustrated here is termed Kretschmann).

This wave has an evanescent nature, with a penetration depth around 300 nm in the sample chamber. In this condition, the photons–plasmons coupling dissipate

energy and the intensity of the reflected light recorder by a detector attenuates, resulting into a sharp minimum in the angle-dependent reflectance. This is, experimentally, the primary recorded quantity[96].

If all parameters such as wavelength, intensity of light and temperature are kept constant, the angle θ at which the excitation of surface plasmons occurs is solely based on the refractivity. When the refractive index of the media n_2 is perturbed, for instance as consequence of mass accumulating at the immediate proximity of the metal layer, the angle θ shifts, and the position of the dip minimum shifts accordingly.

In commercially available SPR biosensors that employ the Kretschmann configuration, the metal is a 50 nm thick gold layer, and the two media are a glass prism (n_1) and the solution flowing in the microfluidic cartridge (n_2), respectively[97]. In a typical SPR experiment, a biological target (ligand) is tethered to the surface of a sensor chip, through chemical modification of the gold film facing the fluidic side, and the analyte is injected over the surface, free in solution (Fig 11).

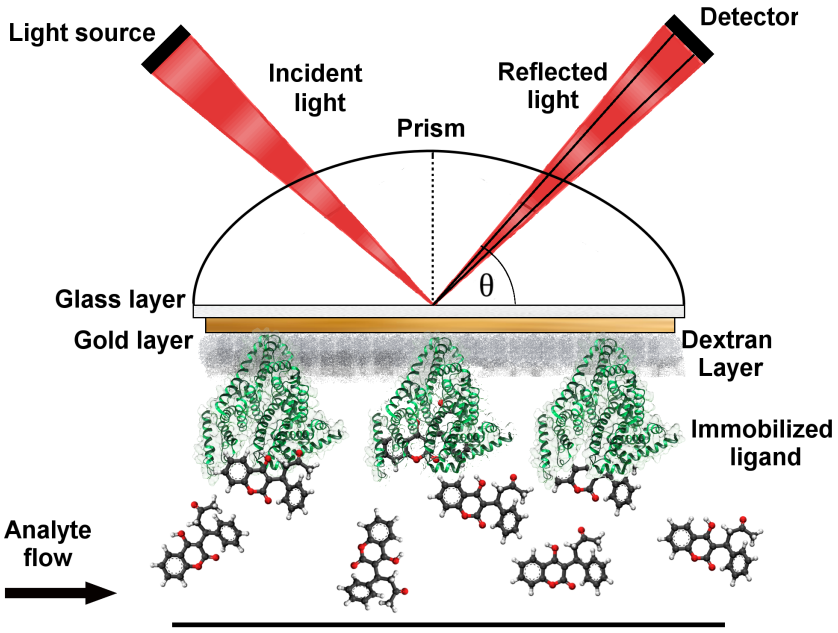

Figure 11 | Schematic representation of the SPR detection principle. The SPR angle Θ, when all other parameters are kept constant, is dependent only on the refractive index of the solution in proximity of the functionalized surface. Upon interaction between the analyte and the ligand, the refractivity at the surface changes, resulting in changes in Θ. The magnitude can be directly correlated to the amount of complex formed.

As a consequence of the ligand–analyte interaction, refractivity of the media n_2 changes, equilibrium condition is perturbed and a response arises. This response is quantified, typically plotted as the change in refractivity (refractivity/response units, RU) over time resulting in a sensorgram (Fig. 12).

A shift of 1 RU corresponds approximately to a change in surface density of 1 pg/mm^2 and a consequent variation of 0.0001° of the SPR angle θ. This allows direct quantification of complex formation[98, 99]. The close dependence between the amount of material bound to the surface, and the shift of the SPR angle θ, has been

demonstrated to be valid, with excellent approximation, regardless of the chemical species involved[100].

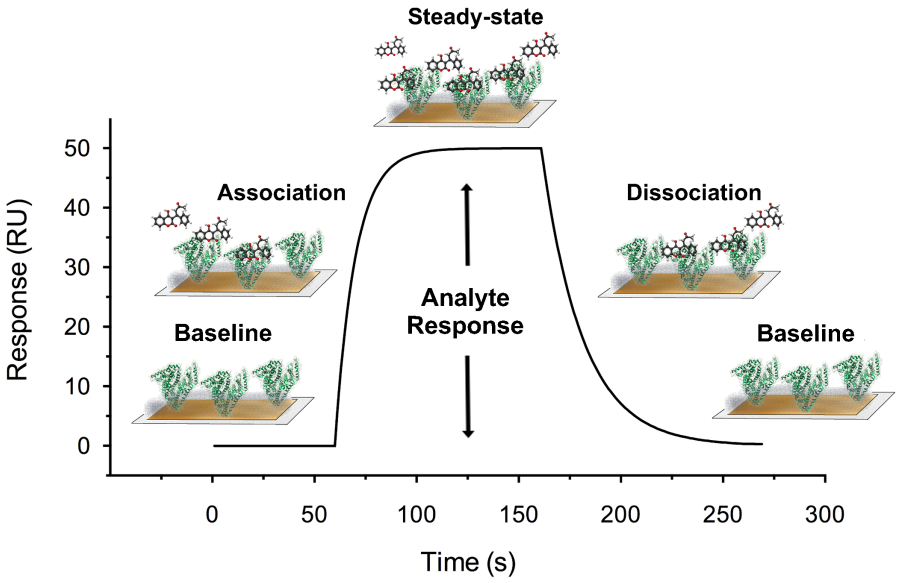

Figure 12 | Typical data output from an SPR experiment. The real-time interaction curve, named sensorgrams, represents an accurate description of the interaction between the tethered ligand and free-flowing analyte. Non-linear regression analysis of sensorgram shapes can be used to extrapolate the rate of association (k_{on}) and dissociation (k_{off}) of the binding event. Responses (expressed in response units – RU), reached at steady-state can be used to construct the isotherm of binding and determine the equilibrium dissociation constant K_D of the ligand–analyte complex.

Instrumentation

Different optical configurations have been employed to investigate molecular binding events through SPR phenomena. The so-called Kretschmann configuration was used to develop a vast array of SPR platforms, both in the traditional and in the imaging (SPRi) format[51, 101-104]. More recently, an alternative SPR configuration, termed localized SPR (LSPR) has emerged. With this mode, SPR is generated on the surface of a nanoparticle rater than a metal film, endowing completely new spectroscopic properties to the metal depending on nanoparticle composition, size, shape, orientation and local dielectric environment. Thanks to the miniaturization potential, LSPR-based devices are viewed as affordable, portable and easy-to-use tool for point-of-care testing[105, 106]. Nonetheless, to discuss the present thesis BIAcore-related instrumentations are the most relevant and therefore they will be presented in details.

In BIAcore platforms (Kretschmann configuration), the gold layer of the sensor is typically functionalized with a dextran hydrogel, resulting in a three-dimensional support available for the immobilization through chemical modification. This provides a flexible support for various methods of immobilization of proteins or other molecules used to define the sensor surface. Moreover, it constitutes a coat that prevents non-specific adsorption of molecules[107, 108]. To meet different experimental requirements, various commercial sensor surfaces have been developed, each one tailored to exploit different immobilization chemistries. For a complete overview of all sensor chips available, please refer to the BIAcore surfaces handbook [BR-1005-71 AB 05/2008].

A microfluidic system creates a series of flow channels wherein different ligands can be immobilized. This forms a sensor chip surface, with multiple

detection spots. An accurate, automated device ensures the inclusion of the sensing surface into the system and a close contact between the fluidics and the optical detection unit. This compartment is precisely thermostated and not directly accessible for the operator during the experiment. Analyte solutions are delivered to the surface by automated injection, and a liquid handling system that precisely controls the flow of buffer and samples. Depending on the platform employed, fluidics, sensitivity and throughput might vary, with top quality products possessing adequate characteristics for fragment library screening. Material consumption is typically very low, and for a complete analysis, only a few micrograms of both the ligand and the analyte are required[109].

SPR experiments

A complete SPR experiment requires two main steps: 1) the immobilization of one of the two interactants on the sensing surface, termed *preparative step*, and 2) the investigation of a given interaction through real-time monitoring, termed *analytical step*.

Immobilization – preparative step

The immobilization procedure can be considered the most challenging part of the experimental set-up, since the ligand needs to retain its biological activity upon anchorage to the surface. Given the wide variation in molecular properties, no generally applicable immobilization method has emerged. Rather different approaches may be needed in order to reach the required activity[110]. In this thesis, the description is limited to the amine coupling and the affinity capture procedures,

representative of the strategies employed to carry on the different experiments. A complete description of all the available techniques can be found in the handbook of surface plasmon resonance.

Amine coupling procedure is based on the formation of a covalent bond between the primary amines exposed on the surface of the ligand (i.e. Lysine) and the carboxyl groups of the carboxylated dextran surface (Fig. 13).

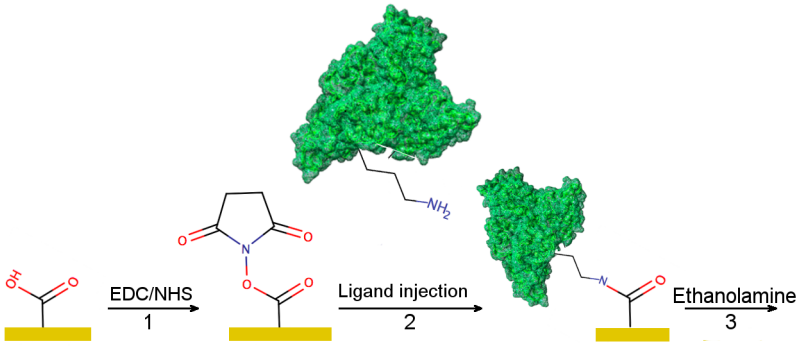

Figure 13 | Representative scheme for amine coupling procedure, with the three basic steps: 1) activation with EDC/NHS, 2) ligand injection and 3) deactivation of the surface.

The ligand needs to be dissolved into a weakly acidic, low ionic strength solution -1 pH unit below the pI of the ligand – to achieve enough electrostatic concentration at the dextran layer, before the linking reaction takes place. Exploiting the negative charges on the acidic groups of the surface and the positive charges of the residues of the ligand, the two chemical entities are drawn near in space. The whole procedure comprises three sequential steps, the *activation* of the surface, the *injection* of the ligand and the *deactivation* of the residual active groups on the surface. The first step consists in the injection of a mixture of 1-

Ethyl-3-(3-dimethylaminopropyl) carbodiimide (EDC) and N-Hydroxysuccinimide (NHS**)** that generates active esters, then through a nucleophilic attack, the primary amines of the protein substitute the esters forming a stable amide bond. Since the reaction leaves some unreacted esters, they need to be quenched. This is achieved through the *deactivation* step, which is performed with Ethanolamine.

Amine coupling is usually able to guarantee high immobilization levels and highly stable sensor chip surfaces. However, the sometimes-harsh conditions needed for the pre-concentration step may affect the ligand activity, and if Lysines are close to the active site of the protein may hamper its functionality. This approach was employed to prepare human and rat serum albumin sensing surfaces *(chapter 6)*.

Immobilization procedure through affinity capture approach relies on the affinity between a capture molecule, covalently attached to the surface (ex. antibody, streptavidin), and the target molecules, which is injected, captured and then used as ligand. The capture molecule recognizes either a tag or a specific epitope of the target molecule, with an affinity able to guarantee enough complex stability to perform an experiment (Fig. 14).

This approach bears some advantages over the classical amine coupling procedure. Even though the immobilization level is usually less than what can be achieved through amine coupling, and the ligand can leak from the surface over a long period, the procedure can be performed in proteins' natural buffer. Furthermore, with this procedure we can orient the ligand on the surface, ensuring that the active sites are exposed and available for the reaction. This overcomes the intrinsic heterogeneity at the surface introduced by the amine coupling. This

approach was employed for SMYD3 and OP_{ureA} immobilizations *(see experimental section)*.

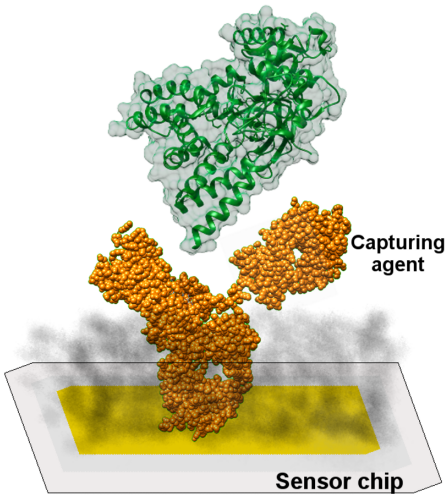

Figure 14 | Illustration of the affinity capture procedure. The capturing molecule (antiGST antibody in this istance) is covalently attached to the surface and the ligand (GST) is capture through high-affinity binding.

Interaction analysis – analytical step

The most-employed approach to perform SPR-based interaction analyses is to anchor the protein on the polymer and to flow the low-molecular-weight analyte over it. This represents a typical direct binding-assay, where different compounds are probed against the same target. Nevertheless, other assay formats have been developed and established.

For instance, in-solution competition can be performed to see if compounds compete for the same binding site on the surface[111, 112]. For instance, large molecules (e.g., proteins), which possess an intrinsically high SPR signal, can

compete with small molecules (e.g., therapeutic agents), which feature low SPR signal; SPR responses are lowered considerably when small molecules bind stronger than large molecules, providing a tool to rank inhibition capacity for selected compounds and qualitatively estimate their inhibition capacity. This approach was useful to support molecular biology in a drug discovery project concerning the epigenetic target SMYD3 project *(chapter 9)* and to confirm the suitability of the SPR assay to test inhibition of the *Hp*NikR–OP_{ureA} interaction *(chapter 7)*.

The experimental conditions are optimized by selecting a suitable buffer and regeneration conditions, the latter needed for slowly dissociating complexes. The concentration range of the analyte needs to be carefully selected, as it is dependent on both the solubility of the compound and its affinity for the ligand. Ideally, the range should cover concentrations comprise between $0.1 \cdot K_D$ and $10 \cdot K_D$. Whenever possible, it is important to include a positive and a negative control in a binding assay. This is to avoid artifacts due to unrelated phenomena that produce a change in refractivity, such as unspecific adsorption to the chip surface or to the protein scaffold, which results in an SPR signal. Careful experimental design and data analysis is crucial for success[113].

There are two main injection modes to performed an interaction analysis using SPR-based biosensors 1) Multi-cycle injections or 2) Single-cycle injections[114] (Fig. 15).

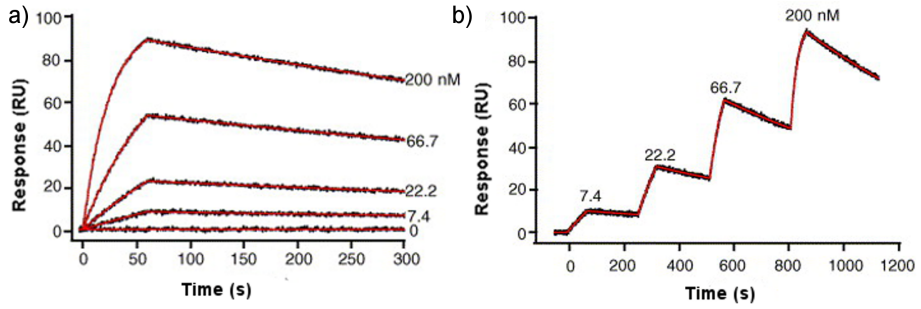

Figure 15 | Representative sensorgrams of (**a**) classical multi cycle injection and (**b**) single cycle kinetic titration (Adapted with permission from ref. [114].

Multi-cycle injection procedure consists in a series of analyte dilutions delivered over the functionalized surface in a separate mode, with each interaction cycle recorded separately. Subsequently, sensorgrams produced by the different concentrations are aligned at the injection start event, overlaid and displayed together in the same graph. For slow dissociating complex is necessary to introduce a regeneration step at the end of the dissociation event to ensure that all binding sites on the surface are available for the next cycle. Otherwise, the partial occupation could interfere with the next analyte series, affecting the overall results. It is important to consider that the regeneration step must leave the functionality of the ligand unaltered in order to guarantee the reproducibility of the interaction among different cycles.

Single-cycle injection: Sometimes the regeneration conditions are hard to optimize for the interaction monitored, because of the instability of the ligand on the surface or the intrinsic properties of the complex that is formed. An alternative approach has been developed to overcome these problems – the single-cycle

injection. It consists in a series of analyte dilutions delivered sequentially over the surface, without regeneration between injections. Data analysis software that takes into consideration the gradual occupation of binding sites during the run, allow accurate determination of kinetic and thermodynamic parameters. Moreover, tightly bound complexes, usually characterized by slow dissociation kinetics, are easy to analyze since the time required for a complete experiment decrease significantly and hard regeneration conditions can be avoided.

5.4. Data evaluation

Different aspects of the (bio)molecular interaction can be studied depending on the final goal of the analysis, the quality of the data and the intrinsic behavior of the two binding partners[113, 115-117]. Since the amplitude of the SPR signal is directly correlated to the change in mass at the sensor surface, the molecular weights of the chemical species involved impose a limitation on the maximal theoretical response achievable for the system under investigation. Comparison of the maximal theoretical and experimental responses can provide information on the apparent binding capacity (often termed the "activity") of the immobilized ligand and on the stoichiometry of the interaction according to the equation (3):

$$R_{max} = MW_{analyte} / MW_{ligand} \cdot RU_{immobilized} \cdot n \qquad (3)$$

where R_{max} is maximal response of the system, $MW_{analyte}$ and MW_{ligand} the molecular weight of the analyte and ligand respectively, $RU_{immobilized}$ is the amount of ligand tethered to the surface and n the stoichiometry of the analyte–ligand reaction.

Plotting responses at steady state against the injected concentrations results in a classical dose-response curve[118] (Fig. 16). The steady state affinity (K_D) for the analyte–ligand complex can be estimated by non-linear regression analysis of the data set according to the following equation (4):

$$R = \sum_i \frac{R_{max\,i} \cdot (C / K_{D_i})}{1 + C / K_{D_i}} \qquad (4)$$

where C is the analyte concentration, and K_D is the equilibrium dissociation constant. For a single-site interaction, $i = 1$, and for multiple binding sites $i = n$, where n is the stoichiometry of the reaction imposed by the number of available binding sites.

Time required to reach the equilibrium for a given reaction is mostly dependent on the dissociation rate k_{off} of the complex; therefore, is not always possible to achieve a steady state condition during the length of an injection, especially at low compound concentrations. However, since responses at equilibrium are not affected by rate of diffusion and they do not account for complex and ambiguous reaction profiles, this approach can sometimes overcome intrinsic limitations of a kinetic fitting procedure[98]. The interaction between serum albumins (SA) and cucurbitacins benefited from steady state affinity analysis rather than kinetic evaluation *(see chapter 6)*. The fast nature of the binding event hampered the quantification of rate constants, providing however a qualitative estimation.

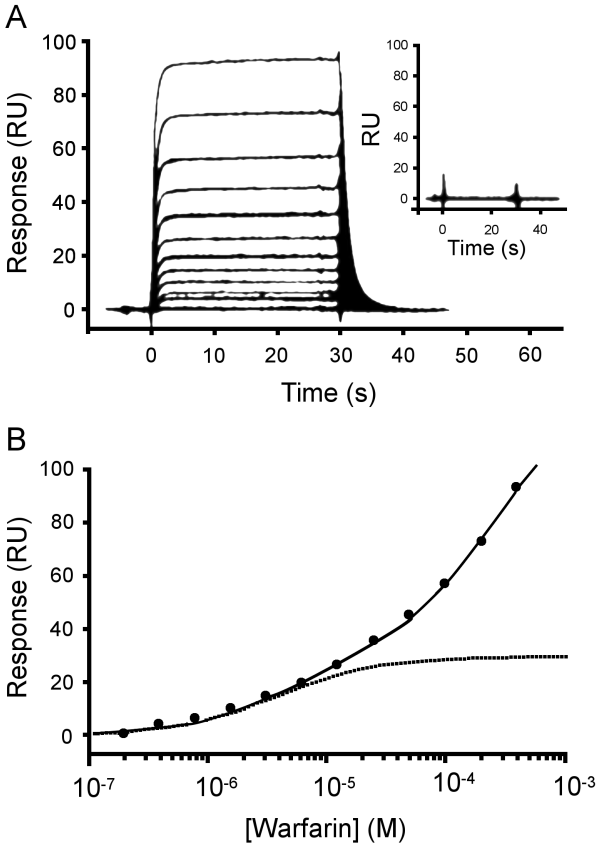

Figure 16 | Representative sensorgrams showing typical Warfarin/HSA interaction over a wide range of concentrations. (**a**) Overlaid sensorgrams obtained from replicate injections of warfarin (0.2 – 400 μM) over HSA-functionalized surface. (Inset) Responses collected from the reference surface. (**b**) Response at equilibrium plotted versus warfarin concentration. The solid line depicts the fit of the data to a theoretic model describing two independent-sites reaction, while the dashed line represents the saturation point of the high-affinity site. The fit yields equilibrium dissociation constants of 3.8 and 273 μM for the high-and low-affinity sites, respectively. Reprinted with permission from reference [118].

Global non-linear regression analysis of a set of sensorgrams at different analyte concentrations can be used to estimate the rate constants for association (k_{on}) and dissociation (k_{off}) events. Computational methods are used to fit theoretic

binding modes to the experimental data and statistical tools are employed to assess their consistency. Some of the most common binding modes are reported here:

a) 1:1 binding (eq. 5):

$$A + B \underset{k_{off}}{\overset{k_{on}}{\rightleftharpoons}} AB \qquad (5)$$

with an overall rate equation for the forward and backward reaction represented by Eq. 5.1:

$$\frac{d[AB]}{dt} = k_{on} \cdot [A] \cdot [B] - k_{off}[AB] \qquad (5.1)$$

and an equilibrium dissociation constant describes by Eq. 5.2:

$$K_D = {k_{off}}/{k_{on}} \qquad (5.2)$$

where k_{on} is the association rate constant ($M^{-1}\ s^{-1}$) and k_{off} is the dissociation rate constant (s^{-1}).

b) Heterogeneous binding, with two independent reactions occurring in parallel (eq. 6):

$$\begin{aligned} A + B_1 &\underset{k_{off_1}}{\overset{k_{on_1}}{\rightleftharpoons}} AB_1 \\ A + B_2 &\underset{k_{off_2}}{\overset{k_{on_2}}{\rightleftharpoons}} AB_2 \end{aligned} \qquad (6)$$

that can be described as the sum of two independent reactions occurring in parallel, each one of them described by a simple 1:1 mechanism with its associated rate equations. This model yields two different sets of k_{on} and k_{off} and two different values of K_D.

c) Two-step reaction, which entails a conformation rearrangement after the first initial encounter between the two interactants, leading to a more stable conformation (eq. 7):

$$A + B \underset{k_{off_1}}{\overset{k_{on_1}}{\rightleftharpoons}} AB \underset{k_{off_2}}{\overset{k_{on_2}}{\rightleftharpoons}} AB^* \qquad (7)$$

The rate equations for the two reactions are described by Eq. 7.1 and Eq. 7.2:

$$\frac{d[AB]}{dt} = (k_{on_1} \cdot [A] \cdot [B] - k_{off_1} \cdot [AB]) - (k_{on_2}[AB] - k_{off_2} \cdot [AB^*]) \qquad (7.1)$$

$$\frac{d[AB^*]}{dt} = (k_{on_2} \cdot [AB] - k_{off_2} \cdot [AB^*]) \qquad (7.2)$$

with an associated equilibrium dissociation constant, that needs to take into account both reactions, described by Eq. 7.3:

$$K_D = \frac{k_{off_1}}{k_{on_1}} \cdot \frac{k_{off_2}}{k_{off_2} + k_{on_2}} \qquad (7.3)$$

where k_{on1} (M^{-1} s^{-1}) and k_{off1} (s^{-1}) are the association rate constant and the dissociation rate constant for the first biding event, and k_{on2} (s^{-1}) and k_{off2} (s^{-1})

represent the kinetic rate constants for the switching to a more stable AB* complex.

Statistical tool χ^2 describes the dispersion of experimental data around the theoretic interaction and as a rule of thumb is should be less than 10% of the R_{max} for a reliable fit. Residual plots are a graphical image of the χ^2, and by visually inspecting them systematic deviations can be recognized and the accuracy of the fitting procedure graded.

Whenever kinetic information on biorecognition events wants to be acquired a high degree of precision in the experimental design is compulsory. To get reliable data from the fitting procedure is essential to assess behavior of the system under investigation: all interactions have to be strictly related to analyte–ligand binding events and avoid artifacts arising from unspecific adsorption to the surface, mass transport limitations or rebinding effects.

Unspecific binding to the surface is mostly related to precipitation of the analyte during the injection, or to the intrinsic charge-dependent interaction with the slightly acidic carboxymethyl dextran layer of the chip. Mass transport limitation (MTL) occurs when the diffusion of the analyte from the bulk solution to the immediate proximity of the surface, where it can bind the ligand, is too slow with respect to the association event (k_{on}). In this instance, diffusion will be the limiting step for the complex formation rather than on-rate. MTL regard mostly protein–protein interactions; macromolecules have limited diffusion rates compared to small molecules for which this factor is usually negligible. In the present dissertation an extensive assessment of the MTL contribution to the interaction between transcription factor *Hp*NikR and dsDNA sequence OP_{ureA} was

conducted and all the experimental details used to minimizing it are presented *(chapter 7)*.

Although there are several fitting models available, which also accounts for artifacts-related deviations, choice of which apply should be carefully evaluated and if otherwise suggested should be kept as simple as possible, i.e. 1:1 reversible binding.

An extended experimental set-up can improve comprehensions for mechanisms deviating from a classical 1:1 binding event and discern them in real multi-components interactions mechanism or poorly designed experiments[119-121]. In the present dissertation an extended experimental procedure was employed to characterize the interaction between the *Hp*NikR and OP_{ureA} where shape of sensorgrams shed light was indicative of a two-step binding mechanism rather than heterogeneous binding to the surface *(chapter 7)*[16].

Overall, kinetic analysis can provide valuable information that otherwise will be lost by the measurement of a simple condition of equilibrium. The possibility to distinguish general affinity into its individual components ($K_D = k_{off} / k_{on}$), provide an important tool to construct more complete structure-activity relationship. Synthesis can be conducted to enhance desired futures with more accuracy, for example: a tight binder with a slow k_{off} will ensure longer residence time (τ) over its receptor and therefore will lengthen its effect while possibly reducing its off-target toxicity[50]. Moreover, multi-component sensorgrams can be deconvoluted into their individual components giving an insight in biorecognition events endowed with exclusive conformational rearrangements.

6. Surface plasmon resonance and circular dichroism characterization of cucurbitacins binding to serum albumins for early pharmacokinetic profiling

(Edoardo Fabini, Giovana Maria Lanchoti Fiori, Daniele Tedesco, Norberto Peporine Lopes, Carlo Bertucci). Journal of Pharmaceutical and Biomedical Analysis (2016) 122:166–172.

Doi: http://dx.doi.org/10.1016/j.jpba.2016.01.051.

Abstract

Cucurbitacins are a group of tetracyclic triterpenoids, known for centuries for their anticancer and antiinflammatory properties, which are being actively investigated over the past decades in order to elucidate their mechanism of action. In perspective of being used as therapeutic molecules, an early pharmacokinetic characterization is highly desirable. Usually, pharmacokinetic data are first collected on animal models and later translated to humans; therefore, an *in vitro* characterization of the interaction with carrier proteins from different species can help forecast distribution volumes in the two different hosts. In the present study, the interactions of cucurbitacins E and I with human and rat serum albumins (HSA and RSA) were investigated by means of surface plasmon resonance (SPR)-based optical biosensing and circular dichroism (CD) spectroscopy. Active HSA and RSA sensor chip surfaces were prepared through an amine coupling immobilization protocol, and the equilibrium dissociation constants (K_D) for the different cucurbitacins-serum albumins complexes were then determined by SPR analysis. Further information on the binding of cucurbitacins to serum albumins was obtained by CD competition experiments with biliverdin, a specific marker binding to subdomain IB of HSA. SPR data unveiled a previously unreported binding event between CucI and HSA; the determined binding affinities of both compounds were slightly higher for RSA with respect to HSA, even though all the compounds can be ranked as high-affinity binders for both carriers. CD analysis showed that the two cucurbitacins modify the binding of biliverdin to serum albumins through opposite allosteric modulation (positive for HSA, negative for RSA), confirming the need for caution in the translation of pharmacokinetic data across species.

Introduction

Cucurbitacins (Cuc) are a class of highly oxygenated, tetracyclic triterpenoids primarily isolated from the plant family of Cucurbitacee. The cytotoxicity of cucurbitacins has been known for centuries and the elucidation of their mechanism of action is an active topic of research; several biological and pharmacological activities have been reported, proposing cucurbitacins as potential anti-cancer, anti-inflammatory and anti-microbial agents[122-125]. For instance, cucurbitacin E (CucE, Fig. 17) disrupts the F-actin cytoskeleton, inhibiting the growth of human prostate carcinoma PC-3 cells[126], and displays anti-angiogenesis activity in human umbilical vascular endothelial cells by suppressing the VEGFR2-mediated Jak2–STAT3 signaling pathway[127]; cucurbitacin I (CucI, Fig. 17), the deacetylated form of CucE, induces apoptosis in Sézary syndrome cells through the inhibition of the same pathway[128] and displays cardioprotective properties through the suppression of the tissue growth factor-mediated signaling pathways in hypertrophic cardiomyocytes[129].

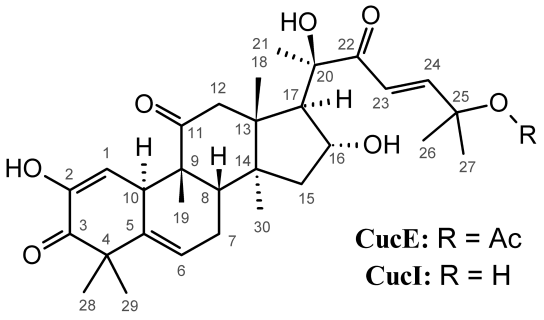

Figure 17 | Chemical structure of CucE and CucI.

In view of the potential use of cucurbitacins as therapeutic agents, binding studies with carrier proteins, and in particular with serum albumins, are highly desirable in order to better characterize their distribution and bioavailability for their primary targets, and therefore understand their pharmacological behavior.

Human serum albumin (HSA) is the most abundant protein carrier in blood serum[130] HSA possesses the ability to bind to several different classes of compounds, both endogenous and exogenous, modulating their properties such as solubility, availability, toxicity and stability[130]. Several techniques have been successfully applied to characterize the binding properties of HSA, e.g. equilibrium dialysis, high-performance affinity chromatography and fluorescence spectroscopy to name a few[20, 131-135]. Among these, circular dichroism (CD)[33, 136] spectroscopy offers the analytical advantages given by its trademark sensitivity to chirality, allowing the investigation of binding events through the phenomenon of induced circular dichroism (ICD)[91]. The ICD signals of specific high-affinity markers for the binding sites of HSA can therefore be exploited to characterize the binding of other analytes by means of competition studies in solution[66, 137].

Optical biosensors based on surface plasmon resonance (SPR) have also been employed during the last years in order to study the interaction between small molecules and proteins[138-141]. In a typical SPR experiment, one of the two binding partners is chemically attached to the surface of a sensor chip (ligand), while the other is free to flow in solution (analyte) and is thus able to interact with the ligand. The response *(R)*, given in arbitrary resonance units (RU), is dependent on the refractive index of the chip surface, which varies proportionally to the change in mass due to the association and/or dissociation of the binding complex between

ligand and analyte. This technique offers advantages over the conventional solution-based techniques:

(a) The interaction between two molecules can be monitored without the need of any labeling, obtaining binding information about unmodified reactants and avoiding the possibility to alter the binding properties[142].

(b) Sensor chips can be used for several cycles of analysis without compromising their functionality, therefore increasing the throughput of the technique[49].

(c) Unlike other equilibrium-based techniques, the interaction can be monitored in real time, providing more detailed information about the binding process[143].

The latter feature is of particular interest when monitoring biological systems, especially when dealing with carrier proteins, since the kinetics of binding greatly influences the pharmacokinetic properties of the bound molecules[118].

During pre-clinical and clinical trials, animal models are routinely used to test the binding properties and the consequent bloodstream distribution of new drug candidates in order to extrapolate pharmacokinetic data for the human body[144].

Though HSA and rat serum albumin (RSA) share a high degree of homology in their amino acid sequences, differences in their binding properties has already been known for long time[145]. Therefore, the investigation of the binding differences among serum albumins from different species becomes of great importance before extrapolating data for clinical studies in humans. Exploiting the versatility of the experimental setup given by SPR-based biosensors, evaluations on the binding properties of different compounds toward immobilized serum

albumins from different species can be achieved and compared with data obtained from other solution-based affinity techniques.

In the present study, cucurbitacins–serum albumins (Cuc–SA) binding complexes were investigated by means of a combination of SPR-based optical biosensing and CD spectroscopic analysis, with particular focus on the binding of CucE and CucI with HSA and RSA.

Results and discussion

SPR analysis of Cuc–SA interactions

Serum albumins' surfaces preparation and validation

High-efficient immobilization was achieved through amine coupling chemistry. With this procedure HSA is tethered to the dextran coating through its primary amine groups exposed to the surface, i.e. lysine residues, and previous studies have already reported that all major binding sites are readily available and accessible in these conditions[118, 146].

Prior to the immobilization, a pH scouting procedure was performed in order to determine which solution, gave the most stable interactions between the ligand and the chip surface. At pH 5.0, HSA produces a stable and time-dependent interaction, which was optimal to control the immobilization density by setting the adequate injection time at the beginning of the procedure. To confirm the full functionality of produced chip surfaces, naproxen (marker for the Sudlow site II of HSA)[131, 132] and (S)-warfarin (Sudlow site I marker) were used as standard

compounds to assess their affinity toward the HSA surfaces. In all cases, a good concentration–response relationship was observed and the resulting K_D values ($3.6 \cdot 10^{-5}$ M for naproxen and $6.0 \cdot 10^{-6}$ M for (S)-warfarin on the high-density chip surface; $2.5 \cdot 10^{-5}$ M for naproxen and $3.6 \cdot 10^{-6}$ M for (S)-warfarin on the low-density chip surface) were in accordance with previously reported SPR analyses (K_D values in the range $3.0 \cdot 10^{-6}$ to $2.6 \cdot 10^{-5}$ M for naproxen, $3.7 \cdot 10^{-6}$ to $1.4 \cdot 10^{-5}$ M for (S)-warfarin)[118, 146]. The affinity of (S)-warfarin toward the RSA surface was also assessed, yielding a K_D value of $2.3 \cdot 10^{-5}$ M which is in good agreement with literature data[147].

Affinity of Cuc–SA complexes

All interactions reached a steady state condition within few seconds from the analyte injection and all complexes dissociated rapidly as indicated from the square wave shape of the sensorgrams (Fig. 18). Binding events between HSA and Cuc were tested over two sensing surfaces. Reproducing biosensor data on different preparations gives more reliability to the whole analysis by avoiding surface-dependent artifacts.

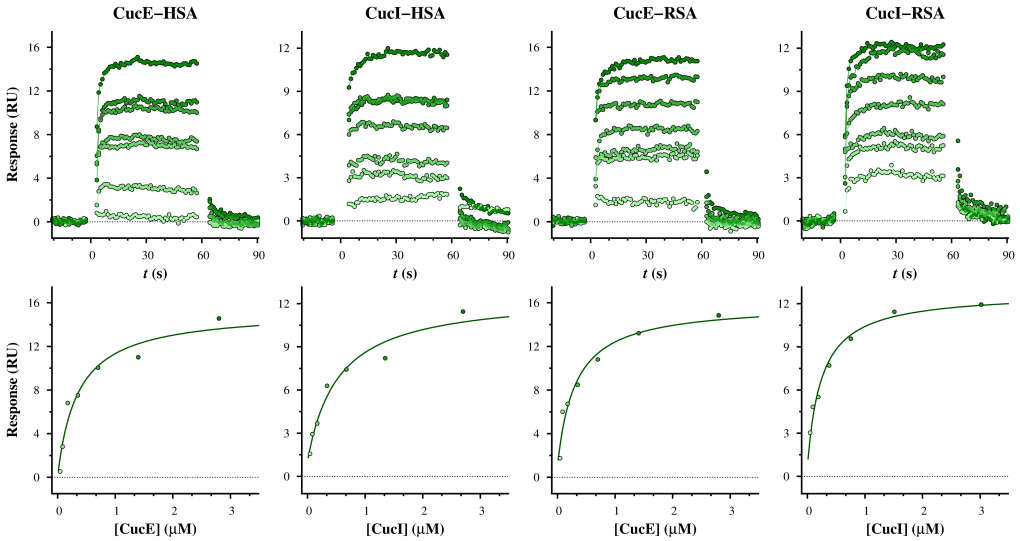

Figure 18 | Representative SPR sensorgrams (*top*) and R_{eq} values fitted to the 1:1 isotherm binding model (*bottom*) for CucE and CucI binding to the high-density HSA and RSA chip surfaces. Increasing concentrations of analyte are denoted by different shades of green (*from light to dark*): 0.05, 0.09, 0.18, 0.35, 0.70, 1.40 and 2.80 μM for CucE–HSA; 0.04, 0.08, 0.17, 0.34, 0.68, 1.35 and 2.70 μM for CucI–HSA; 0.05, 0.09, 0.18, 0.35, 0.70, 1.40 and 2.80 μM for CucE–RSA; 0.04, 0.08, 0.17, 0.34, 0.68, 1.35 and 2.70 μM for CucI–RSA.

Second surface was prepared with reduced HSA immobilization level. In this condition, the R_{max} signals decreases and the signal-to-noise ratio decreases accordingly; however, the influence of non-specific interactions, such as steric hindrance, crowding and aggregation at the functionalized surface, is also reduced allowing to provide cleaner and more reliable sensorgrams[113]. The binding affinity of the CucE–HSA interaction, was determined by independent experiments on both sensor chips, and resulted in an average K_D value of $5.0 \cdot 10^{-7}$ M, which is in good agreement with the literature value of $5.8 \cdot 10^{-7}$ M obtained by solution-based fluorimetry assays[148].

The K_D value for the binding of CucI toward HSA was estimated to be $1.8 \cdot 10^{-6}$ M, suggesting a previously unreported interaction between the two molecules. On the other hand, both CucE and CucI showed higher affinity toward RSA with respect to HSA, with estimated K_D values of $2.9 \cdot 10^{-7}$ M and $2.8 \cdot 10^{-7}$ M, respectively.

The binding percentage of cucurbitacins to serum albumins (expressed as the percent fraction of bound drug, *xb*) was also estimated. The *xb* values were derived from K_D following the procedure described by Rich et al.[118], assuming a physiological serum albumin concentration of 680 μM and a Cuc concentration of 10 μM, which is the standard concentration used in the majority of dialysis studies reported in literature. The corresponding *xb* values indicate that both cucurbitacins can be ranked as high-affinity binders for HSA and RSA. Results for all the analyzed interactions are reported in Table 2.

	K_d (M)	k_{on} (M^{-1} s^{-1})	k_{off} (s^{-1})	k_{off} / k_{on} (M)	x_b (%)
CucE–HSA	$(5.0 \pm 1.0) \cdot 10^{-7}$	$(3.6 \pm 0.7) \cdot 10^{5}$	$(3.4 \pm 0.7) \cdot 10^{-1}$ [a]	$(9.5 \pm 1.1) \cdot 10^{-7}$	99.3 ± 0.1
CucE–RSA	$(2.9 \pm 1.0) \cdot 10^{-7}$	– [b]	– [b]	– [b]	99.6 ± 0.1
CucI–HSA	$(1.8 \pm 0.7) \cdot 10^{-6}$	$(4.6 \pm 2.4) \cdot 10^{4}$	$(1.5 \pm 1.2) \cdot 10^{-1}$ [a]	$(3.4 \pm 1.5) \cdot 10^{-6}$	97.4 ± 1.0
CucI–RSA	$(2.8 \pm 0.1) \cdot 10^{-7}$	– [b]	– [b]	– [b]	99.6 ± 0.1

Table 2 | Equilibrium dissociation constant (K_D), kinetic rate constants (k_{on} and k_{off}) and percentages of binding (x_b) derived from the SPR analysis on Cuc–SA binding complexes.

The kinetics of binding between cucurbitacins and HSA was then evaluated by applying a 1:1 kinetic interaction model (eq. 5) to the SPR datasets, in order to extrapolate the k_{on} and k_{off} rate constants (Fig 19).

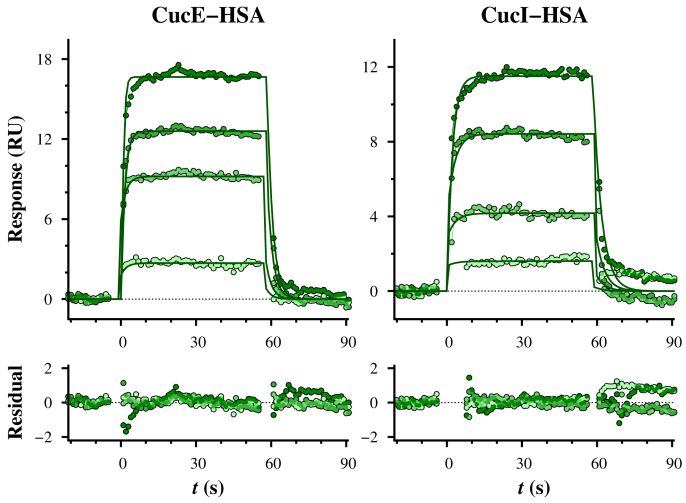

Figure 19 | Kinetic fitting of SPR sensorgrams for CucE and CucI binding to the high-density HSA chip surface. Increasing concentrations of analyte are denoted by different shades of green (*from light to dark*): 0.04, 0.18, 0.70 and 2.80 μM for CucE; 0.04, 0.17, 0.68 and 2.70 μM for CucI.

The residual plots and the χ^2 values were examined to assess the reliability of the theoretical model applied to the experimental data; full details are reported in the Supplementary Material of original manuscript. The K_D values derived from equation 5.2 for the Cuc–HSA interactions ($9.5 \cdot 10^{-7}$ M for CucE, $3.4 \cdot 10^{-6}$ M for CucI) were similar to the ones obtained from the steady-state affinity study; on the other hand, the model failed to provide reliable values for the kinetic parameters of Cuc–RSA interactions. The determined kinetic rate constants allow to hypothesize that part of the higher affinity toward HSA displayed by CucE with respect to CucI is due to a 8-fold faster association (k_{on}= 3.6×10^5 M^{-1} s^{-1} for CucE, k_{on} = 5.0×10^4 M^{-1} s^{-1} for CucI), although the BIAcore evaluation software provided numerical estimates for the k_{off} rate constants which are often outside the optimal range of work of the instrument in the Supplementary Material of the

original article**.** As a consequence, the fast nature of this specific dissociation event may require further examination and more advanced techniques to be measured with greater precision.

CD analysis of Cuc–SA interactions

The cucurbitane skeleton of CucE and CucI (Fig. 17) is characterized by the presence of 8 stereogenic centers of defined absolute configuration at positions 8 (S), 9 (R), 10 (R), 13 (R), 14 (S), 16 (R), 17 (R) and 20 (R). CucE only differs from CucI for the presence of the acetoxy group in place of the hydroxy group at position 25, which is however too distant from the stereogenic centers to be affected by the overall stereochemistry and to display a strong contribution to the chiroptical properties of CucE. The observation of very similar CD signals for CucE and CucI is therefore not surprising (Fig. 20): the spectra in the 450–250 nm spectral range are dominated by the $n \rightarrow n^*$ of the three ketone chromophores and by the $\sigma \rightarrow \sigma^*$ transitions of the two unsaturated ketones, which give rise respectively to a negative CD band centered at 327 nm and a positive CD band centered at 282 nm.

The $n \rightarrow n^*$ CD band of CucE and CucI lies in a spectral region where the spectroscopic contribution of serum albumins is absent, which is an ideal situation for monitoring eventual ICD phenomena. Upon binding to serum albumins, however, the CD profiles of CucE and CucI are not altered, meaning that the binding mechanism is not endowed with a particular stereospecific character (Fig. 20).

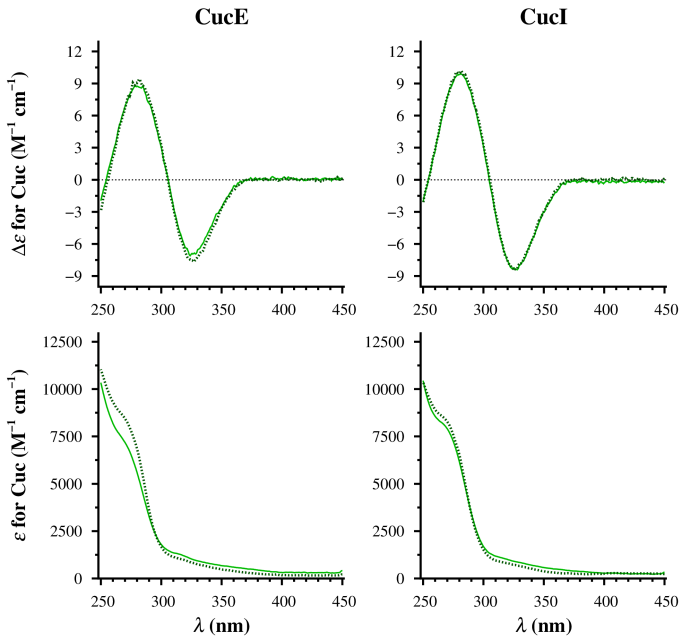

Figure 20 | CD and UV spectra of CucE and CucI in solution (*solid lines*) and protein-corrected spectra of their 2:1 complexes with HSA (*dotted lines*). Experimental conditions are reported in the Materials and Methods section.

The position of the CD bands of CucE and CucI is also a huge limitation for the application of CD spectroscopy to the study of Cuc–SA complexes: the usual ICD markers for high-affinity HSA binding (phenylbutazone for the Sudlow site I in subdomain IIA, diazepam for the Sudlow site II in subdomain IIIA)[66, 149] display their characteristic spectral features between 350 and 250nm. Therefore, competition studies by CD spectroscopy were performed using BV, an ICD marker for the proposed binding site III in subdomain IB of HSA[150].

Upon binding to HSA, the bound conformation of BV displays (M)-axial chirality with the onset of a negative ICD band centered around 670 nm and a

positive ICD band at 385 nm, both outside the spectral range of Cuc absorption (Fig. 21). BV also binds to RSA in (M)-conformation: the resulting positive ICD band for the 1:1 RSA–BV complex lies at the same wavelength as for the 1:1 HSA–BV complex and is relatively more intense (~+50%).

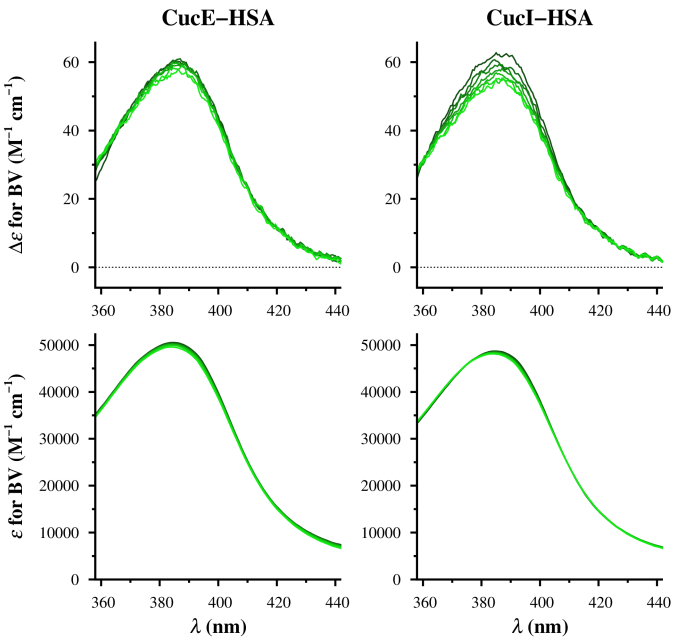

Figure 21 | Protein-corrected CD and UV spectra for the 1:1 HSA–BV binding complex, in the absence (light green) and in the presence of cucurbitacins. Increasing concentrations of cucurbitacins are denoted by different shades of green (from light to dark). Experimental details are given in the Materials and Methods section in the supplementary of the original article.

When CucE and CucI are added to the 1:1 HSA–BV complex, the magnitude of the ICD band for BV at 385 nm slightly increases (Fig. 22): interestingly, the enhancement of the ICD band is more pronounced when CucI is used in the competition study, while the effect of CucE is more limited.

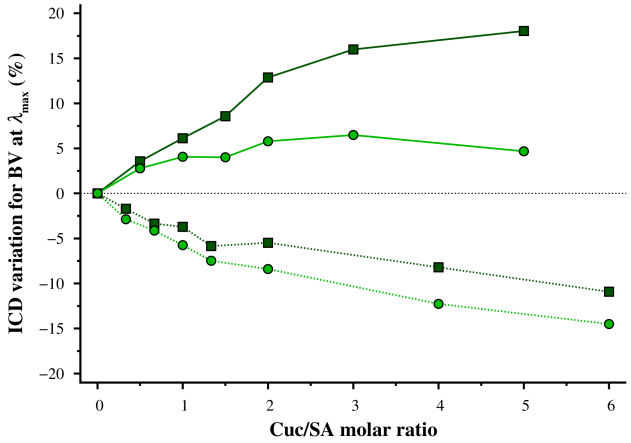

Figure 22 | Effect of increasing concentrations of CucE (*circles*) and CucI (*squares*) on the magnitude of the positive ICD band of HSA–BV (*solid lines*) and RSA–BV (*dotted lines*) complexes. Experimental details are reported in the Materials and Methods section and in Tables S3–S4 in the Supporting Information.

An increase in ICD intensity for a marker is usually indicative of positive allosteric modulation toward the binding site of the marker and an indirect proof of binding for the analyte. Previous investigations on Cuc binding to HSA by fluorescence spectroscopy revealed that CucE enhanced the affinity of bilirubin (BR) toward HSA, while CucI was found to have no effect on HSA–BR binding[151]. BR, the reduced form of BV, binds to the same subdomain IB of HSA and is also, incidentally, one of the most studied ICD markers for high-affinity HSA binding[66, 149]. The different effect of CucI on the binding of BR and BV to HSA may seem contrasting. It must be noted, however, that the additional flexibility of the reduced methylene bridge allows for a different binding mode of BR when compared to BV, even though both molecules bind to the same site of HSA; actually, the different signs of the corresponding ICD bands indicate that the stereoselectivity of binding for BR and BV is opposite, with BR binding to HSA

with a (P)-axial chirality. In some cases, the axial chirality of bound BR can even be inverted through allosteric modulation[152]. The behavior of CucI confirms the high flexibility of the binding site in subdomain IB and the complex allosteric network regulating the binding of drugs to HSA.

Interestingly, the positive ICD band for BV at 385 nm decreased in intensity when CucE and CucI were added to the 1:1 RSA–BV complex (Fig. 22), suggesting either a competition for the same binding site or a negative allosteric modulation. The available data are not sufficient to discriminate between these two different mechanisms, although the limited extent to which the ICD band for BV is decreased supports the hypothesis of negative allosteric modulation. It is worth noting that the binding of CucE and CucI to serum albumins of different species led to different effects on BV binding, confirming the need for careful investigations before translating pharmacokinetic profiles from animal models to humans.

Conclusions

The present article reported the investigation on the binding of cucurbitacins E and I to human and rat serum albumins by means of a combination of SPR-based optical biosensing and CD spectroscopic analysis. The steady state and kinetic analysis of SPR sensorgrams for Cuc–SA complexes unveiled a previously unreported binding event between CucI and HSA, with CucI showing a 3-fold lower affinity than CucE. Moreover, the K_D values of CucE and CucI toward RSA resulted to be slightly higher than those observed for HSA, with both compounds binding to RSA with comparable affinity. The calculated percentages of binding

allow to rank cucurbitacins E and I as high-affinity binders for both serum albumins. CD spectroscopic analysis showed that cucurbitacins E and I are able to modulate the binding of biliverdin to serum albumins, as observed by the concentration-dependent change in intensity of the positive ICD band of biliverdin upon titration with cucurbitacins. Interestingly, the opposite behaviors observed with HSA and RSA suggest a different type of allosteric modulation by cucurbitacins, positive for HSA and negative for RSA. These observations allow to confirm the usefulness of SPR and CD analysis for the characterization of the pharmacokinetic profiles of drugs and the need for caution in the translation of pharmacokinetic data across species for new drug candidates.

Materials and methods

Materials

Cucurbitacin E (CucE; molecular weight, MW: 556.76 Da) and cucurbitacin I (CucI; MW: 514.16 Da) were purchased from Extrasynthese (Genay, France). HSA (essentially fatty acid free, ≥96%, product code A1887; MW: 66.4 kDa), RSA (essentially fatty acid free, essentially globulin free, ≥99%, product code A6414; MW: 64.6 kDa), sodium dihydrogen phosphate (NaH_2PO_4), disodium hydrogen phosphate (Na_2HPO_4), dimethyl sulfoxide (DMSO), sodium naproxen (MW: 252.24 Da), (S)-warfarin (MW: 308.33), biliverdin hydrochloride (BV; MW: 619.12 Da), sodium chloride (NaCl) and sodium acetate were all purchased from Sigma–Aldrich (Milan, Italy). Research-grade CM 5 sensor chips, 10X phosphate buffer saline (PBS) and the amine coupling kit, consisting in N-ethyl-N-(3-dimethylaminopropyl)-carbodiimide (EDC), N- hydroxysuccinimide (NHS) and ethanolamine hydrochloride (pH 8.5; 1M), were all purchased from GE Healthcare Bio-Sciences (Uppsala, Sweden). Water was bi-distillated, de-ionized, filtered and degassed by Millipore Elix 10. Phosphate buffer (PB) (20 mM) + NaCl (150 mM) (pH 7.4) (running buffer A) was used for the immobilization pro- cedure, while 1X PBS–DMSO (95:5, v/v) (pH* 7.4) (running buffer B) was used for the Cuc–SA interaction studies. All buffer solutions were freshly prepared prior to the analysis and filtered through a 0.22 μm pore size membrane made of a mixture of cellulose nitrate and acetate.

SPR analysis

Instrumentation

SPR measurements were performed with a BIAcore X100 system (GE Healthcare Bio-Sciences, Uppsala, Sweden) equipped with an in-line degasser and thermostated at 25 ◦ C. Data were analyzed and processed using the BIAcore X100 2.0 evaluation software.

Surface preparation and validation

Stock solutions of HSA at a 30 g mL^{-1} concentration were prepared in sodium acetate buffers (10 mM) at various pH values (pH 4.0, 4.5, 5.0 and 5.5), and the electrostatic pre-concentration at the chip surface was evaluated by injecting each stock solution for 180 s at a 5 μL min^{-1} flow rate, after which the baseline was re-established by injecting a NaOH solution (50 mM). The best condition was achieved using the pH 5.0 stock solution.

Consequently, HSA was immobilized on two CM 5 sensor chips via amine coupling according to the standard BIAcore procedure, using the pH 5.0 stock solution. Briefly, the chips were equilibrated at room temperature for 30 min before docking, and the system was primed three consecutive times with running buffer A. The carboxymethyl dextran matrix was activated on both channels of the sensor chip by injecting a freshly prepared mixture of EDC (0.4 M) – NHS (0.1 M) (1:1, v/v) at a 5 μL min^{-1} flow rate for 7 min. Then, the pH 5.0 stock solution of HSA was injected over the active flow cell until the desired amount of immobilized protein was reached, i.e. 9000 RU for the first sensor chip (hereafter referred to as high-density chip) and 5000 RU for the second (low-density chip), while running buffer A was injected over the reference flow cell in order to create a surface to account for non-specific binding events. Finally, the remaining active esters were quenched by injecting ethanolamine hydrochloride for 7 min at a 5 μL min^{-1} flow rate (Fig. S1 in the Supplementary Material of the original article). At the end of the whole procedure, the surfaces were allowed to stabilize overnight and, after several buffer injections, a steady baseline was achieved. A single RSA surface was prepared following the same protocol and resulted in an immobilization level of around 8500 RU.

The affinities of naproxen toward HSA and (S)-warfarin toward HSA and RSA were evaluated in order to confirm the correctness of the immobilization procedure and validate the binding capacity of the chip surfaces. 1 mg mL^{-1} stock solutions of (S)-warfarin and naproxen in DMSO were diluted 1:20 (v/v) using 1X PBS to a final concentration of 162 μM and 198 μM, respectively, in running buffer B (pH* 7.4). These solutions were further diluted using running buffer B and injected over the surface at a 30 μL min^{-1} flow rate; association was allowed for 60 s and dissociation was monitored for 120 s.

Solvent refractive index correction

Since DMSO has a high refractive index (addition of 1% DMSO gives a bulk response of around 1200 RU), a solvent correction procedure[146] was performed to account for the small variations of DMSO percentage between samples and in the preparation of running buffers. Eight running buffers, consisting of 1X PBS mixed with different amounts of DMSO ranging from 4.5% to 5.8% (v/v) (pH* 7.4), were injected over the active and reference flow cells and a calibration curve was obtained. This procedure is very important while working with small molecules–macromolecules interactions, especially when the ligand is immobilized at high density (5000 RU or more). In this experimental set-up, the expected response has the same magnitude as, or lower magnitude than,

the signal arising from refractive index mismatches, therefore including a cor- rection protocol during the evaluation of the data becomes of great significance.

Sample preparation

2 mg mL^{-1} stock solutions of CucE and CucI were prepared in DMSO and stored at −20 ◦ C. The stock solutions were then diluted 1:20 (v/v) each day immediately before analysis using 1X PBS, resulting into a final concentration of 50 µg mL^{-1} in running buffer B (pH* 7.4) for both cucurbitacins. All further dilutions were made using freshly prepared running buffer B.

Analysis of Cuc–SA interactions

Affinity assays were carried out during the same day for both cucurbitacins at 25 ◦ C. The flow rate was set at 30 µL min^{-1} and kept constant throughout all the analyses. For the high-density HSA chip and for the RSA chip, association and dissociation were monitored for 60 s and 120 s, respectively, after which additional 300 s of running buffer B (pH* 7.4) were flowed. Every three cycles, a blank injection was performed in order to monitor the baseline stability and account for systematic and random variations. A concentration range from 3.0 µM to 0.04 µM, obtained by a series of two-fold dilutions, was used in order to assess the affinity of CucE and CucI for both serum albumins.

Data for the Cuc–HSA interactions were also collected onto the low-density HSA chip surface, using a concentration range from 9.0 µM to 0.05 µM in a series of four-fold dilutions. Association and dissociation were both monitored for 30 s; subsequently, 120 s of running buffer B (pH* 7.4) were flowed over the surface in order to monitor the stability of the baseline.

Data analysis

Sensorgram datasets for CucE, CucI, naproxen and (S)-warfarin binding to serum albumins were processed according to the same protocol. The responses from the active flow cell were double-referenced against the responses from the reference flow cell and against an average of all the blank injections taken every three cycles of analysis; finally, the solvent refractive index correction was applied[113].

The resulting responses at equilibrium were fitted to a 1:1 isotherm binding model, defined in Eq. (4), in order to extrapolate the equilibrium dissociation constant (K_D) of the ligand-analyte complex.

Each measurement was replicated at least twice and each dataset was fitted in the binding model independently; the resulting parameters were subsequently averaged and expressed with the corresponding standard deviation. Sensorgrams resulting from the Cuc–HSA interaction were also fitted to a simple 1:1 kinetic interaction model, according to which the K_D value is derived from the ratio between the rate constants for association (k_{on}) and dissociation (k_{off}), as shown in Eq. 5.2. The χ^2 parameter was used as a statistical tool to evaluate the closeness of the fitting model to the experimental data. The experimental datasets showing non-negligible residual plots after the statistical fitting were discarded and not taken into account for the determination of the kinetic constants.

CD analysis

Instrumentation

CD and UV spectroscopic analyses were carried out at 25◦C on a Jasco (Tokyo, Japan) J-810 spectropolarimeter equipped with a PTC-423S Peltier-type temperature control system, using a 10 mm pathlength quartz cell (Hellma, Milan, Italy), a 2 nm spectral bandwidth, a 0.5 nm data pitch and an accumulation cycle of 3 runs per measurement. Data were analyzed and processed using the Jasco Spectra Manager 2 software package.

Analysis of Cuc–SA complexes

5 mM stock solutions of CucE and CucI were prepared in DMSO, while stock solutions of HSA (300 μM), RSA (300 μM) and BV (3 mM) were prepared in running buffer B (pH* 7.4). Samples of cucurbitacins (3.75, 7.5, 15, 30 and 60 μM) were prepared by directly diluting appropriate aliquots of 5 mM stock solutions with running buffer B (pH* 7.4). Cuc–SA complexes were analyzed at different drug/protein molar ratios (0.25, 0.5, 1, 2 and 4) by diluting the protein stock solution with running buffer B (pH* 7.4) to a concentration of 15 μM and subsequently adding increasing aliquots of Cuc stock solution. The resulting decrease in final protein concentration during all titration experiments never exceeded 1.5%, and the total content of DMSO in the samples never exceeded 6.5% (v/v).

CD and UV spectra of samples were then measured in the 450–250 nm spectral range using a 50 nm/min^{-1} scanning speed and a 2 s data integration time. The increase in DMSO content did not increase the solvent contribution to the total spectroscopic response of samples in the investigated

spectral range; consequently, solvent corrections for the samples of cucurbitacins were performed by subtracting the signal of running buffer B (pH* 7.4). On the other hand, the spectra of drug/protein samples were corrected by subtracting the spectra of serum albumins, in order to evaluate the eventual onset of ICD signals upon binding.

Competition studies with biliverdin

A similar protocol was used for competition experiments on HSA–biliverdin (BV) complexes (in the Supplementary Material of the original article): HSA and BV were mixed at a molar ratio of 1:1 and diluted to 15 μM in running buffer B (pH* 7.4). Increasing aliquots of Cuc stock solution were subsequently added to the 1:1 HSA–BV complex in order to obtain different Cuc/SA molar ratios (0.5, 1, 1.5, 2, 3 and 5).

For RSA–BV competition experiments (Fig. S5 in the Supplementary Material of the original article), the concentration of the 1:1 protein/marker complex was kept at 7.5 μM in running buffer B (pH* 7.4); subsequently, increasing aliquots of Cuc stock solution were added to the 1:1 RSA–BV complex yielding different Cuc/SA molar ratios (0.33, 0.67, 1, 1.33, 2, 4 and 6).

CD and UV measurements were carried out in the 700–250 nm spectral range using a 100 nm min^{-1} scanning speed and a 1 s data integration time; blank corrections were performed by subtracting the spectra of serum albumins from the spectra of protein/marker and drug/protein/marker samples. The effect of CucE and CucI on the ICD signal of BV was monitored at the wavelength of maximum UV absorption for BV, lying at around 385 nm: the relative variations of the corresponding ICD signal (expressed as percentage) with respect to the HSA–BV and RSA–BV complexes were plotted as a function of the Cuc/SA molar ratio (Tables S3–S4 in the Supplementary Material of the original article).

7. Surface plasmon resonance and isothermal titration calorimetry to monitor the Ni(II)-dependent binding of Helicobacter pylori NikR to DNA

(**Edoardo Fabini,** Barbara Zambelli, Luca Mazzei, Stefano Ciurli, Carlo Bertucci). Analytical and Bioanalytical Chemistry (2016) 408(28):7971–7980.

Doi 10.1007/s00216-016-9894–0.

Abstract

NikR is a transcription factor that regulates the expression of Ni(II)-dependent enzymes and other proteins involved in nickel trafficking. In the human pathogenic bacterium *Helicobacter pylori*, NikR (*Hp*NikR) controls, among others, the expression of the Ni(II) enzyme urease by binding the double-strand DNA (dsDNA) operator region of the urease promoter (OP_{ureA}) in a Ni(II)-dependent mode. This article describes the use of surface plasmon resonance (SPR) spectroscopy in combination with isothermal titration calorimetry (ITC) to carry out a mechanistic characterization of the *Hp*NikR–OP_{ureA} interaction. An active surface was prepared by affinity capture of OP_{ureA} and validated for the recognition process in the SPR experiments. Subsequently, the Ni(II)-dependent affinity of the transcription factor for its operator region was assessed through kinetic evaluation of the binding process at variable Ni(II) concentrations. The kinetic data are consistent with a two-step binding mode involving an initial encounter between the two interactants, followed by a conformational rearrangement of the *Hp*NikR–OP_{ureA} complex, leading to high affinity binding. This conformational change is only observed in the presence of the full set of four Ni(II) ions bound to the protein. Additionally, the SPR assay developed and validated in this study constitutes a suitable method to screen potential drug lead candidates acting as inhibitors of this protein–dsDNA interaction.

Introduction

Ni(II) is an essential micronutrient for several bacteria, archea, plants, fungi, and unicellular eukaryotes[153, 154]. Its limited availability, coupled to its intrinsic toxicity, represents a pressure factor for the development of specific systems for metal accumulation, detoxification, and utilization, governed by Ni(II)-specific cellular responses. These processes are controlled by dedicated transcriptional regulators, whose ability to recognize or bind DNA is modulated in response to the Ni(II)-loaded state of the proteins, acting as fine sensors of intracellular Ni(II) concentration[155].

The most studied Ni(II)-sensor is NikR, a transcription factor that controls Ni(II) metabolism in more than 30 species of bacteria and archea. NikR from *Helicobacter pylori* (*Hp*NikR) is a pleiotropic regulator[156, 157]: it represses its own gene as well as the gene coding for NixA, a Ni(II) permease responsible for the import of Ni(II), and acts as an activator of genes coding for the Ni(II)-dependent urease, a pathogenic factor[158, 159]. Crystal structures of *Hp*NikR, *Escherichia coli* NikR (*Ec*NikR) and *Pyrococcus horikoshii* NikR (*Ph*NikR), established that this protein is a homo-tetramer, made of a dimer of dimers, constituted by two domains: the central metal-binding domain (MBD) and two ribbon-helix-ribbon DNA-binding domains (DBDs)[160-166]. MBD is constituted by dimerization of the C-terminal portion of the protein, it is responsible for tetramerization and hosts four regulatory Ni(II) binding sites; the DBDs are built from the dimerization of the N-terminal portion of the protein, they flank the MBD and are responsible for dsDNA binding.

NikR has been observed in three different conformations in the crystal structures, open, trans, and cis, depending on the conformation of the short link

between the MDB and the DBDs. Notably, the cis conformation is adopted when the protein binds to dsDNA in the presence of Ni(II)[163].

In addition to structure-based design and development of new urease inhibitors[167], the elaboration of new strategies against *H. pylori* could also entail the modulation of its Ni(II)-dependent transcriptional pathways by preventing the functional interaction of the Ni(II)-loaded *Hp*NikR with its dsDNA operator. Protein binding to DNA generally involves large surfaces, and it is therefore more difficult to drug than deep binding pockets present in most enzymes. In addition, transcription factors such as NikR do not generally show enzymatic activity usable as a probe. For this reasons, protein–DNA interactions were previously defined as undruggable[168]. Nevertheless, some examples of small molecules (SMs) targeting these molecular recognition processes are emerging, especially in cancer research[169]. High-throughput screenings have been developed, rendering SM screening possible for this aim[170, 171].

In the last decades, optical-based surface plasmon resonance (SPR) biosensors have become more frequently employed at different stages of the drug discovery process because of their relative ease of use, versatility, small samples consumption, and short analysis time[49, 172, 173]. A typical SPR platform offers the possibility to perform real-time evaluation on unmodified interactants, without the need of a time-consuming labeling step, thus providing a valid tool to monitor a wide range of biological events, such as protein–protein interactions and small molecule–receptor interactions[49]. Furthermore, the real-time measurements allow a reliable determination of kinetic parameters, in addition to steady-state affinity and thermodynamic data[174]. If the technique is fully exploited and the SPR experiments are carefully designed, it is even possible to resolve multi components

reaction mechanisms, thus providing helpful aid to study complex binding events[121, 175]. Additionally, in-solution competition assays can be performed, taking advantage of the experimental set up versatility[176]. For instance, large molecules (e.g., proteins), which possess an intrinsically high SPR signal due to their mass, can compete with small molecules (e.g., therapeutic agents), which feature low SPR signal, for the same binding sites on the ligand; SPR responses are lowered considerably when SMs bind stronger than large molecules, providing a tool to rank inhibition capacity for selected compounds[177, 178].

Along with SPR, isothermal titration calorimetry (ITC) can be used to obtain thermodynamic information of intermolecular interactions, and thanks to its high sensitivity, ITC has become widely used to study biomolecular equilibria involving protein–ligand, protein–protein, protein–metal ions, and protein–DNA interactions[179]. In addition to thermodynamic parameters, kinetic information can also be extrapolated by means of ITC to study enzymatic reactions[180, 181] as well as to provide complete kinetic characterization of biomolecular interactions[182-184].

In the present work, SPR spectroscopy is employed to derive kinetic and thermodynamic parameters of the HpNikR–OPureA system, in order to gain fundamental insights into the reaction mechanism and the role that Ni(II) plays in this protein–dsDNA binding process. A sensor chip surface bearing immobilized dsDNA OPureA was prepared by affinity-capture technique, and its functionality and recognition ability were extensively assessed. Auto-competition experiments were also performed, to further confirm the specificity of the recognition mechanism. These results were complemented and supported by ITC data. Moreover, the outcome of this study is the development of an assay for the

screening of potential lead candidates to target this interaction, paving the way toward rationally designed therapeutic agents.

Results and discussion

Surface plasmon resonance analysis

Surface preparation and validation

Biotinylated-OPureA was immobilized onto a streptavidin-functionalized sensor chip, ensuring a stable surface with an estimated functionality of 60 % (Eq. 3). Interactions were reproducible over 100 analysis cycles, and no significant drift of the baseline was detected.

The magnitude of the SPR signal is proportional to the molecular mass of the interactants according to equation 3, allowing high instrumental responses, up to 1000 RU, for our system. Nevertheless we chose to keep the maximal response at 100 RU, to reduce unspecific binding due to crowding effects. Therefore, streptavidin was covalently immobilized onto a CM5 sensor chip at approximately 2000 RU, corresponding to a density level of 2 ng mm^{-2}, and the OP_{ureA} operator sequence was captured over the streptavidin coated surface at a low level of approximately 30 RU. Capture of OP_{ureA} was performed at low flow rate, using diluted solutions, exploiting the affinity for the biotin residue on the DNA, as this procedure is known to generate an homogeneous surface, where ligand molecules posses a common orientation[113, 185]. Ten base pairs, corresponding to a full helix turn, were added to the operator sequence to better separate the double strand from the dextran layer, allowing *Hp*NikR to bind the sequence without steric hindrance.

The shape of relative sensorgrams for association and dissociation events of the Ni(II)-*Hp*NikR–OP_{ureA} complex are generally smooth and of high quality, without any apparent mass transport limitation (MTL) effect. However, during the optimization process, different sensor chips were prepared with different densities of both streptavidin and OP_{ureA} and the contribution of the MTL was extensively assessed onto the surface, which showed the best interaction profile (Fig. 23). Kinetic rate constants k_{on} and k_{off} for a given interaction are independent from the flow rate applied, therefore if the mass transport limitation (MTL) is negligible, their values should not change with the flow rate. Hence, fix concentration of analyte was injected at different flow rate, 20, 40 and 60 μL min^{-1} and the resulting experimental data were fitted to a 1:1 binding model; then all data were superimposed in the same plot (Fig. 23d). Both experimental and theoretical sensorgrams are overlapping, and their shapes are exponential from the first seconds of the association phase indicating that the MTL is not interfering with the reaction monitored. In addition, the mass transport coefficient k_t being two orders of magnitude larger than the association rate constant k_{on}, further indicates the low contribution of the MTL. Therefore an average flow rate of 30 μL min^{-1} was chosen as best the condition to minimize sample consumption.

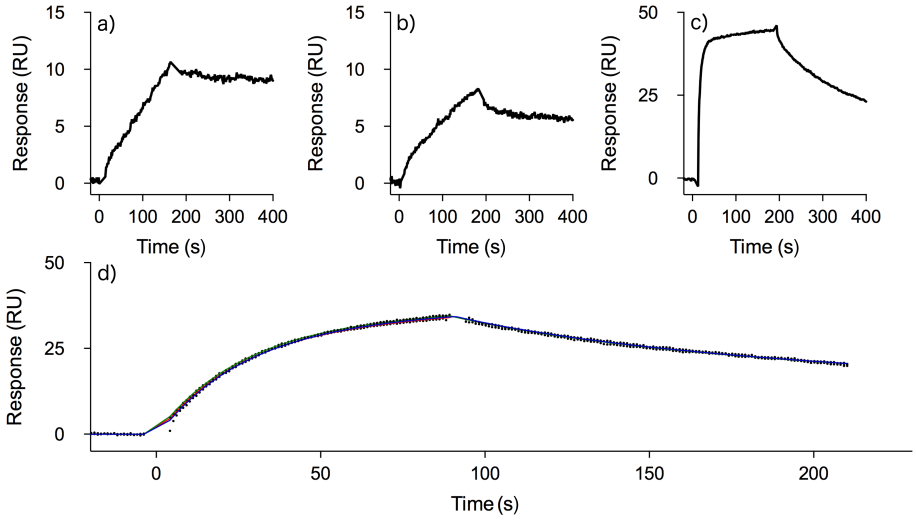

Figure 23 | Different combination of streptavidin and biotinylated–OP_{ureA} were immobilized over the CM5 sensor chip surface. In the preparation (**a**) 4000 RU of streptavidin were covalently attached to the surface through amine coupling reaction and 75 RU of dsDNA were loaded over the surface. Ni(II)-*Hp*NikR 500 nM was then injected at 30 µl min^{-1} flow rate. Similarly two different surfaces were prepared bearing (**b**) 4000 RU of streptavidin, 40 RU of dsDNA and c) 2000 RU of streptavidin, 30 RU of dsDNA, respectively, and the Ni(II) bound protein was injected at a concentration of 1 µM. Since the preparation (**c**) clearly showed the best interaction profile, the mass transport limitation (MTL) on the interaction was assessed with the injection of a fix Ni(II)-*Hp*NikR concentration (125 nM) at different flow rates 20, 40 and 60 µl min^{-1}. Association and the dissociation were monitored for 90 and 120 seconds respectively and the relative sensorgrams were displayed in panel (**d**). The overlaying of the experimental data (black dots) and the theoretical fitting for the different flow rates analyzed in the study (20 µL min^{-1}, red; 40 µL min^{-1}, blue and 60 µL min^{-1}, green) along with the mass transport coefficient k_t being two order of magnitude larger than the association rate constant k_{on} (both obtained from the non-linear regression analysis), can be taken together as an indication of the small influence of the MTL on the interaction monitored.

*Hp*NikR–OP_{ureA} interaction analysis

Since *Hp*NikR in its simplest description is represented by a fully functional protein bound to four Ni(II) ions or by an inactive protein devoid of any bound Ni(II)[186], the biological activity of the sensor chip was evaluated through the

injection of the protein in the absence or in the presence of four Ni(II) ions per tetramer (Fig. 24).

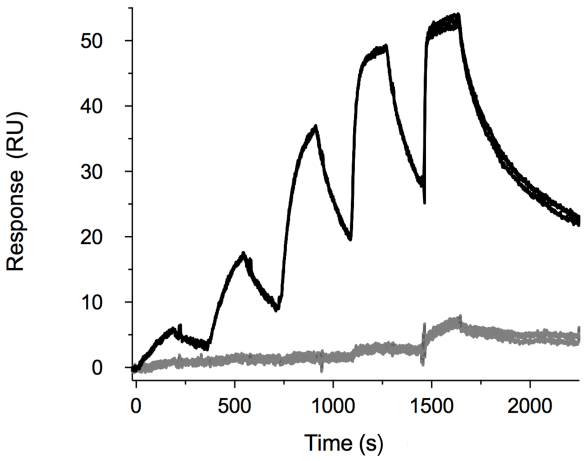

Figure 24 | Double-referenced sensorgrams representing the interaction between the holo form of Ni(II)-*Hp*NikR bound to four Ni(II) ions, (*black lines*) or the apo- *form of Hp*NikR devoid of Ni(II) ions (*light grey*) with the OP_{ureA} tethered to sensor chip surface. Samples were injected in increasing protein concentrations. **Ni(II)-*Hp*NikR / apo-NikR** (2, 10, 50, 250, 1000) nM

The resulting sensorgrams showed that *Hp*NikR does not bind the urease operator in the absence of Ni(II), while holo-*Hp*NikR interacts with dsDNA in the presence of four Ni(II) equivalents per protein tetramer, confirming that OP_{ureA} has retained its functionality after the immobilization procedure. The specificity of the recognition process was also assessed by means of a competition assay: upon incubation of Ni(II)-*Hp*NikR with equimolar concentrations of non-biotinylated OP_{ureA} in solution, no appreciable binding of the protein to the immobilized OP_{ureA} is observed during the injection (Fig. 25).

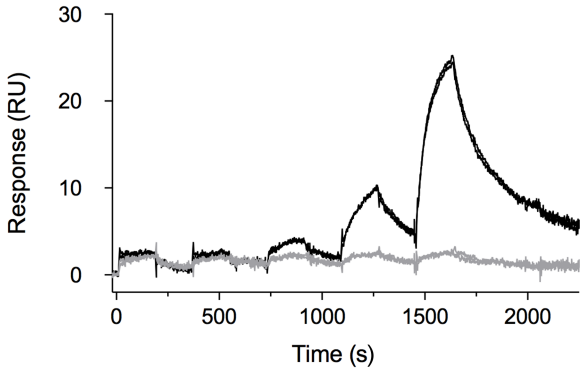

Figure 25. Double-referenced sensorgrams representing the in-solution competition assays experiment. Ni(II)-*Hp*NikR injected in a five-fold serial dilution (black line) and Ni(II)-*Hp*NikR incubated with equimolar non-biotinylated OP_{ureA} (light grey line). The 1:1 complexes were prepared at the same concentration of the Ni(II)-bound protein alone. **Ni(II)-*Hp*NikR** (0.2, 1.0, 5.0, 25.0, 125.0) nM.

Considering the similar affinity of Ni(II)-*Hp*NikR for OP_{ureA} in solution or immobilized on the surface, this observation suggests a slow dissociation between Ni(II)-*Hp*NikR and OP_{ureA} in solution, which prevents further binding of *Hp*NikR to the immobilized operator.

Steady-state affinity between immobilized OP_{ureA} and Ni(II)-*Hp*NikR was then investigated over a broad range of protein concentrations (from 2 nM to 1 μM) injected in a two-fold serial dilutions (Fig. 26). Fitting each independent data set to the 1:1 binding isotherm model (Fig. 26 b, Eq. 4) produced an average K_D value of 55.0 ± 14.4 nM, in full agreement with the value previously obtained using ITC (56 nM)[186], further confirming that the immobilization process did not interfere with the biological activity of the OP_{ureA}. Moreover, a mean R_{max} of 46.4 ± 9.9 RU for the different sensor chip preparations employed during the study showed an

excellent reproducibility of the immobilization protocol and of the analysis conditions (Table 3).

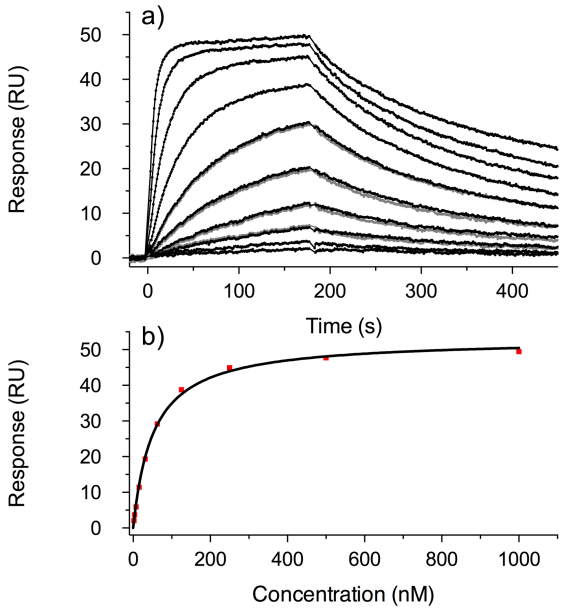

Figure 26 | Double-referenced sensorgrams (**a**) and equilibrium responses fitted to the Eq. 1 (**b**) for the interaction of Ni(II)-*Hp*NikR, with immobilized OP_{ureA}. Protein samples were delivered from the lowest to the highest concentration (2, 4, 8, 16, 31, 63, 125, 250, 500 and 1000 nM). Intermediate concentrations (8, 16, 31, 63 nM) were injected in duplicate. Interaction displayed in the figure is representative of a run carried out on one of the three surface prepared in the study.

Visual inspection of the sensorgrams revealed that the formation of the Ni(II)-*Hp*NikR–OP_{ureA} complex did not reach equilibrium within the 180 s of the injection time; instead, a small but continuous increase of the SPR signal upon binding was detected, suggesting an interaction more complex than a simple binding event. To gain deeper knowledge on the system, a series of holo-protein samples were injected over the dsDNA-functionalized surface in a twofold serial dilution (2.3–300 nM) (Fig. 27), and the resulting curves were fitted to theoretic

interaction models. Non-linear regression analysis using a simple 1:1 binding (eq. 5) model provided sub-optimal description of the experimental data (Fig. 27), requiring the use of more complex theoretical models describing multi-components reaction mechanisms.

Chip	K_D (M)	R (RU)
1	$4.59 \cdot 10^{-8}$	35.69
2	$4.74 \cdot 10^{-8}$	55.19
3	$7.16 \cdot 10^{-8}$	48.45
Average	$(5.5 \pm 1.4) \cdot 10^{-8}$	46.4 ± 9.9

Table 3 Equilibrium dissociation constants K_D obtained from the steady-state affinity analysis carried out on the three different sensor chip surfaces. Ni(II)–*Hp*NikR was injected from 1 μM to 2 nM in a two-fold serial dilution in MCK analysis mode

First, a heterogeneous binding model was applied (Eq. 6), which involves two independent reactions occurring in parallel. This event could arise from two different scenarios: (i) the protein binds to OP_{ureA} in two non-equivalent sites, with a 1:1 stoichiometry and different kinetics, or (ii) the protein binds to OP_{ureA} only in one site, with dsDNA existing in alternative forms that interact differently with the protein, likely reflecting structure heterogeneity on the surface or non-specific binding events[187]. Second, an interaction model that describes a two-step reaction mechanism was considered (Eq. 7), which entails the formation of an initial complex, subsequently switching to a more stable conformation that cannot dissociate directly in the two initial interactants. Both models provided a better description of the experimental data with respect to the 1:1 binding event (Fig. 27b, c, respectively), as expected from models that can fit multiple parameters simultaneously[188].

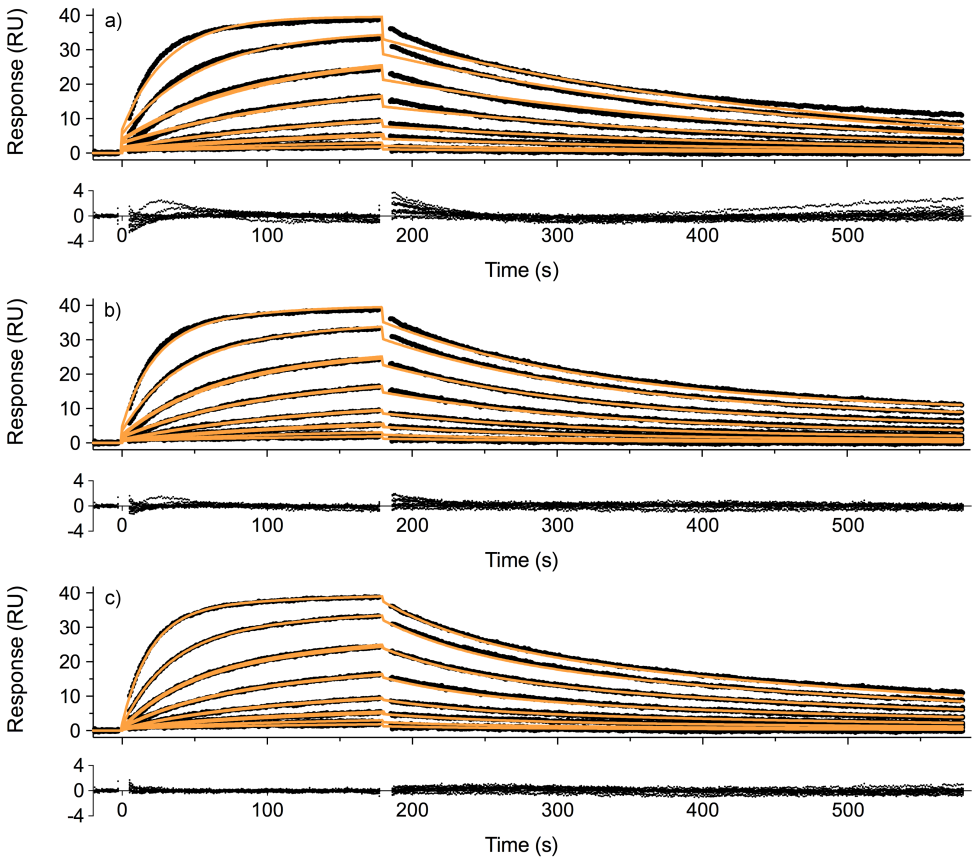

Figure 27 | Double-referenced sensorgrams (*dark*) with different super-imposed theoretical model (*light*) for the same Ni(II)-*Hp*NikR–OP_{ureA} interaction. The residual plot for each non-linear regression analysis is shown below each data set. (**a**) 1:1 binding, (**b**) heterogeneous model, (**c**) two-state interaction mechanism. Samples were delivered from the lowest to the highest concentration (2.3, 4.7, 9.4, 18.8, 37.5, 75, 150, 300 nM), with four intermediate concentrations injected in duplicate in random order.

However, they present similar values of the statistical parameters χ^2 (see Tables S2 and S3 in supplementary of the original article) and similar residual plots, and therefore, it was not possible to choose, at this stage, one model over the other to provide a definitive description of the binding event. The formation and parting of the protein–operator complex was thus further investigated through single cycle

kinetic titration (SCK) titration, where a series of five Ni(II)-*Hp*NikR samples, including a protein concentration able to saturate all the available binding sites, were injected over the functionalized surface, and the final dissociation event was monitored for an extended period of 600 s (Fig. 28).

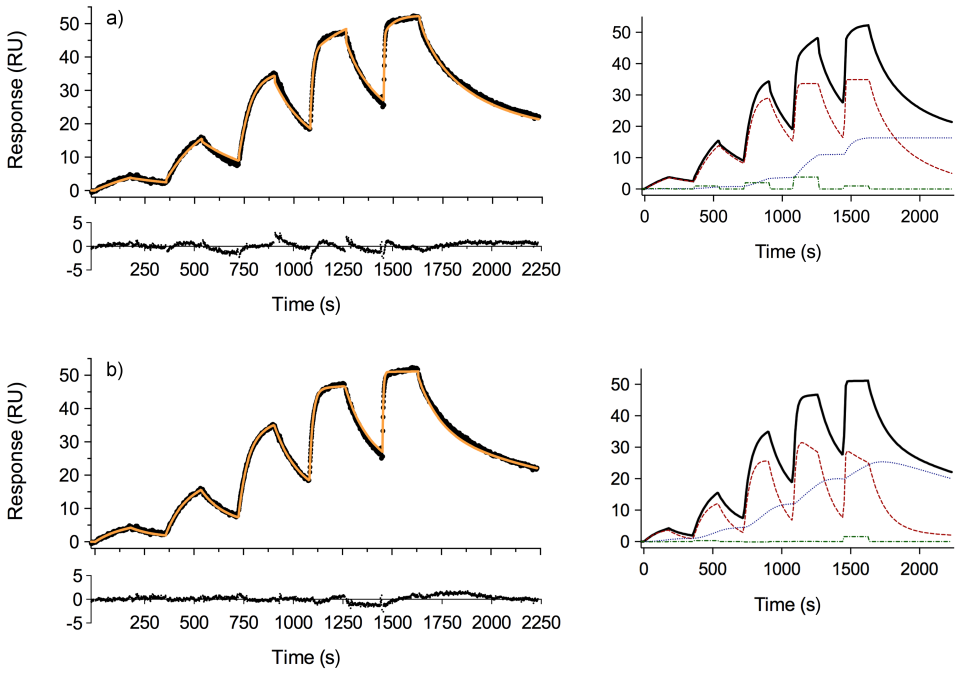

Figure 28 | Double-referenced sensorgrams representing the single cycle kinetic titration (SCK) of Ni(II)-*Hp*NikR–OP_{ureA} interaction. Theoretical curves (*light*) are superimposed to the experimental data (*dark*) and the relative residual plot is displayed below. The protein was injected from the lowest to the highest concentration (2, 10, 50, 250, 1000 nM). On the right side the relative contributions of the different binding components to the total response are displayed. (**a**) Heterogeneous binding model, (c^2 = 0.63): Total response (*black solid*), AB1 complex (*red dashed*), AB2 complex (*blue dotted*), bulk + drift (*green dotted-dashed*) (**b**) Two-state reaction mechanism, with a correlated (c^2 = 0.44. T): total response (*black* solid), AB complex (*red* dashed), AB* complex (*blue* dotted), bulk + drift (*green* dotted-dashed). **Ni(II)-*Hp*NikR** (2, 10, 50, 250, 1000) nM.

This experimental setup provided a more balanced number of data points between the association and dissociation phases with respect to the classical multi-cycle approach, providing support for the interpretation of complex interactions (Fig. 28a, b). Fitting procedures based on the two-step process produced a slightly lower χ^2 value (χ^2 = 0.44) as compared to the heterogeneous model (χ^2 = 0.63), supporting a binding mechanism that involves sequential binding events. In order to establish whether the reaction shows time-dependence and therefore can be described by a two-step mechanism, a fixed concentration of Ni(II)-*Hp*NikR (500 nM) was delivered by varying the length of the injection (Fig. 29).

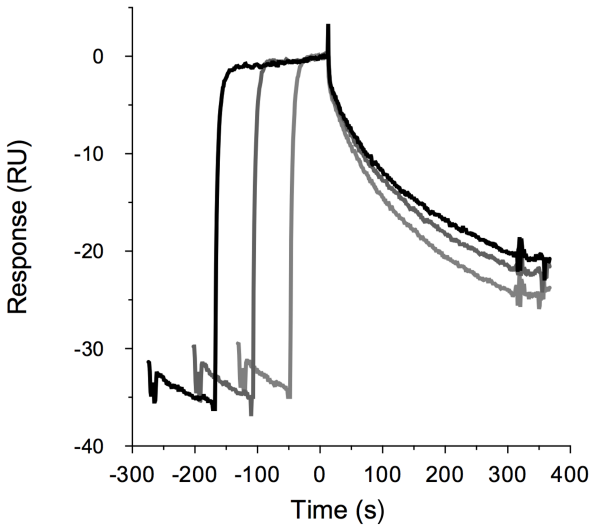

Figure 29. Sensorgrams representing the effect of different injection lengths on the dissociation event of the *Hp*NikR–OP_{ureA} complex in the presence of 4 Ni(II) per tetramer. (From darker to lighter: 180 s, 120 s and 60s). **Ni(II)-*Hp*NikR** 500 nM.

For a simple 1:1 interaction, when all binding sites are occupied, the dissociation curves should be independent from the contact time and therefore

identical when overlaid[116, 188]. In the present case, the dissociation event becomes slower when the two binding partners are left to interact for increasing periods of time (Fig. 29), suggesting a stabilization event involving the Ni(II)-*Hp*NikR–OP_{ureA} complex. In accordance to all evidences provided by the extended experimental setup, the two-state binding model was applied. This scheme was applied to extrapolate the values of kinetic rate constants: $k_{on1} = (1.9 \pm 0.7) \cdot 10^5$ M^{-1} s^{-1}, $k_{off1} = (1.6 \pm 1.1) \cdot 10^{-2}$ s^{-1}, $k_{on2} = (3.3 \pm 1.2) \cdot 10^{-3}$ s^{-1}, and $k_{off2} = (3.4 \pm 0.5) \cdot 10^{-3}$ s^{-1}, with a global associated K_D of 36 ± 11 nM. The entire data sets for the kinetic analysis, showing also rate constants calculated for 1:1 binding and heterogeneous binding models, are collected in Tables S2, S3, and S4 in the supplementary material of the original article.

Isothermal titration calorimetry

Previous data on the Ni(II)-*Hp*NikR interaction with OP_{ureA}, obtained by ITC[186], were re-analyzed by taking advantage of a novel method, named kinITC, that quantifies the kinetics through the analysis of the shape of each ITC injection peak[182, 183]. The presence of a kinetic signal in ITC is revealed by a significant variation of the time required for each heat trace to return to the baseline along the series of multiple ligand injections, with the largest value reached when the 1:1 stoichiometry is approached. Therefore, from the raw data, an equilibration–time curve (ETC) was derived that reports the equilibration times against the stoichiometric ratio corresponding to each injection. A fitting of the curve (χ^2 = 1.8) provided a value for $k_{off} = (6.8 \pm 0.7) \cdot 10^{-3}$ s^{-1}, from which $k_{on} = 1.2 \pm 0.1 \cdot 10^5$ M^{-1} s^{-1} could be derived for the interaction of Ni(II)-*Hp*NikR with OP_{ureA}

using the known value of K_D = 56 nM, provided by ITC steady-state analysis, as well as by EMSA and DNase footprinting[186].

Ni(II) dependence of the binding mechanism

The ITC analysis of Ni(II) binding to *Hp*NikR revealed that the protein binds four Ni(II) with a 2 + 2 stoichiometry[189]. This bi-partite Ni(II) binding mode poses the question of which form of the protein is competent for dsDNA binding, *cis* or *trans*, and whether two Ni(II) ions bound per protein tetramer are sufficient to activate the protein toward this event. This question was addressed by investigating the *Hp*NikR–dsDNA binding in the presence of sub-stoichiometric Ni(II) concentrations, using both ITC and SPR (Fig. 30).

The binding isotherm obtained by ITC for *Hp*NikR binding to OP_{ureA} in the presence of two Ni(II) ions per tetramer (Fig. 30a) provided an affinity constant (K_D = 230 ± 20 nM) higher than, but comparable to, the one calculated for the fully metal-loaded protein (K_D = 56 ± 5 nM). However, the binding stoichiometry was significantly lower (n = 0.16 ± 0.01 as compared to n = 0.9 ± 0.1), indicating that only ca. 16 % of the protein molecules is competent for dsDNA binding.

Calculation of the species distribution under these experimental conditions, indicates that the fraction of the protein containing four Ni(II) per protein tetramer is indeed 18 % at 2:1. The observed stoichiometry is therefore an indicator that only the protein bound to four Ni(II) ions is competent for dsDNA binding with high affinity, while the occupancy of two metal sites is not sufficient to promote protein binding to dsDNA with similarly high constants.

This binding behavior was further assessed using SPR, injecting a fixed protein concentration of 200 nM, which was previously incubated with 0, 1, 2, 3, and 4 equivalents of Ni(II) per tetramer. The results showed that both the response and the subsequent stabilization effect increase with increasing concentration of Ni(II) ions in solution (Fig. 30b and Table in the supplementary material of the original article).

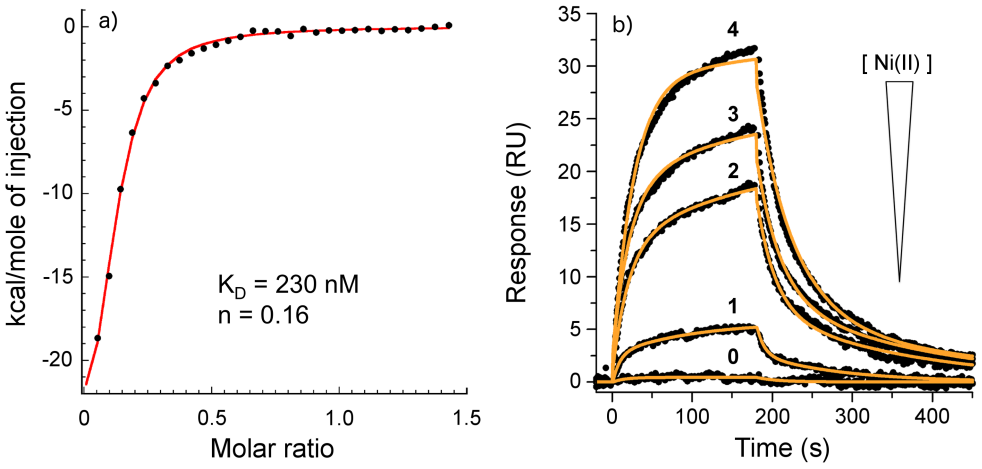

Figure 30 | (a) ITC binding isotherm for OP_{ureA} (40 µM) titration over *Hp*NikR (4 µM) in the presence of 8 µM $NiSO_4$. Fit of the normalized heat of reaction data (dots) is represented as a *red* line. The binding stoichiometry and dissociation constant are K_D = 230 nM and n = 0.16 respectively. (**b**) Representation of the interaction between 200 nM *Hp*NikR incubated with different equivalents of Ni(II) per protein tetramer. Equivalents of Ni(II) in the sample are indicated above each sensorgram. Theoretical fitting to a two-state interaction mechanism (*orange*) are superimposed to the experimental data (*black*). Responses (RU) are proportional to the amount of Nickel in the sample.

Interestingly, in the presence of only one Ni(II) equivalent the calculated amount of *Hp*NikR loaded with four Ni(II) is negligible, while the rest of the protein contains either two or zero Ni(II) bound in comparable amounts. Considering that apo-*Hp*NikR did not show any signal in SPR (Fig. 24), the

response must derive from the fraction of the protein bound to two Ni(II) equivalents. Under these conditions, response is very low and data fitting by a two-step model or by a 1:1 binding produced qualitatively similar theoretic interaction curves (data not shown), suggesting the absence of a stabilization step when only two Ni(II) ions are bound to *Hp*NikR.

Mechanistic analysis of the HpNikR–OPureA interaction

Taken together, the SPR data analysis is consistent with the presence of a two-step binding event; first, an initial encounter between protein and dsDNA establishes an intermediate and subsequently, a conformational rearrangement leads toward the final, highly stable, *Hp*NikR–OP_{ureA} complex. The nature of this stabilization event can be interpreted considering previously reported data: (i) calorimetric experiments indicated that four Ni(II) ions bind to the MBD of *Hp*NikR (and *Ec*NikR) and produce a conformational effect that propagates far away from the metal binding sites[155, 186, 189]; (ii) small angle X-ray light scattering (SAXS)[190, 191], NMR spectroscopy[192] and analysis of protein dynamics[192] consistently show that this conformational change does not correspond to a rearrangement of the protein structure toward a specific *cis* conformation able to bind dsDNA, but rather involves an increase of mobility of the peripheral DBDs through the flexible linker connecting it to the MDB. This phenomenon allows the protein to span more efficiently a larger conformational ensemble and facilitates the search for the protein conformation optimal to bind dsDNA through an induced fit mechanism. Indeed, the isolated MDB and DBD maintain their functional properties of Ni(II) and dsDNA binding, respectively, indicating that the function of the protein as a nickel-dependent dsDNA interactor resides in their relative

position on the dsDNA operator[193]. In this view, we suggest that the stabilization event observed in the SPR analysis is related to the acquired ability of the protein to assume the *cis* conformation, unlocking the N-terminal DBDs as compared to the C-terminal MBD. These findings support the proposition of an adaptive mechanism promoted by the presence of both the OP_{ureA} and four Ni(II) ions per protein tetramer.

Conclusions

The results obtained in the present study extend our knowledge on the mechanism of *Hp*NikR–OP_{ureA} interaction, highlighting a two-step binding mechanism, which leads to the formation of a high stable complex in the presence of 4 Ni(II) equivalents per protein tetramer. Moreover, the implementation of a validated SPR-based assay constitutes a suitable starting point to develop new methods for screening lead candidates to modulate this protein–dsDNA interaction, aimed at the eradication of H. pylori.

Materials and methods

Chemicals and instrumentation

Streptavidin, N-2-hydroxyethylpiperazine-N′-2-ethanesulfonic acid (HEPES), ethylenediaminetetraacetic acid (EDTA), sodium chloride (NaCl), polyoxyethylenesorbitan monolaurate (p-20), sodium dodecyl sulfate (SDS), and Ni(II) sulfate hexahydrate ($NiSO_4 \cdot 6\ H_2O$) were purchased from Sigma-Aldrich (Milan, Italy). Research-grade CM 5 sensor chips, sodium acetate buffer 10 mM pH 5.0, 10X HEPES buffer saline (HBS-EP+) (consisting of HEPES 0.1 M, NaCl 1.5 M, EDTA 30 mM, p-20 0.5 % v/v), and the amine coupling kit, consisting of N-ethyl-N-(3-dimethylaminopropyl)-carbodiimide (EDC), N-hydroxysuccinimide (NHS) and ethanolamine hydrochloride-NaOH (pH 8.5; 1 M), were purchased from GE Healthcare Bio-Sciences (Uppsala, Sweden). All surface plasmon resonance (SPR) measurements were performed with a BiacoreTM X100 system (GE Healthcare Bio-Sciences) equipped with an in-line degasser and thermostated at 25 °C. Data were analyzed and processed using the BIAevaluation 4.1 software. 1X (HBS-EP) (1:9, v/v) (pH 7.4) solution was used as immobilization buffer, while a solution containing HEPES 20 mM, NaC[189]l 150 mM and p-20 0.05 % (v/v) (pH 7.0) was used as running buffer. Interaction analyses were all carried out at constant flow rate of 30 μL min^{-1}. Isothermal titration calorimetry (ITC) experiments were performed using a VP-ITC (Microcal, Malvern) equilibrated at 25 °C as previously described[180].

Surface plasmon resonance

Sample preparation

Apo-HpNikR tetramer (69 kDa) was expressed and purified following a previously described protocol[189] and stored at −80 ° C in 20 mM HEPES buffer at pH 7.0 containing 150 mM NaCl. A 10 mM $NiSO_4$ water solution was diluted at a suitable concentration with running buffer and mixed with apo-NikR each day prior to the analysis to prepare stock solutions of the holo form of the protein, referred as Ni(II)-HpNikR in this work, and containing four Ni(II) ions per tetramer. All further dilutions of both apo- and holo-NikR were performed directly in running buffer.

Single-strand oligos with the sequence of the urease operator (sense: 5′-ATATAACACTAATTCATTTTAAATAATAATTA-3′; antisense: 5′-TAATTATTATTTAAAATGAATTAGTGTTATAT-3′) containing ten additional bases at 5′ end (sense: 5′-CGCTTCAAAA-3′; antisense: 5′-TTTTGAAGCG-3′) were purchased from Life Science

and annealed into the double-strand urease operator (OP_{ureA}). The sense oligo was covalently linked, at the 5′ end, to a biotin molecule required for the surface preparation in the SPR experiments, while the antisense was used as such. Similarly, non-extended and non-biotinylated double-strand OP_{ureA} was purchased and prepared for in-solution experiments.

Surface preparation and validation

Streptavidin was diluted at 100 μg mL^{-1} in sodium acetate buffer 10 mM pH 5.0 and immobilized through amine coupling reaction; subsequently, biotinylated OP_{ureA} was captured over the previously functionalized surface exploiting the biotin–streptavidin affinity[194]. Flow cell 1 (reference flow cell) and flow cell 2 (active flow cell), of a CM5 sensor chip, were activated by injection of a freshly prepared EDC (0.4 M) and NHS (0.1 M) mixture for 7 minutes at a flow rate of 10 μL min^{-1}. Then, the appropriate amount of streptavidin was attached on both channels exploiting the target level function provided from the BIAcore control software. Afterwards, the remaining active esters were quenched by injecting Ethanolamine-HCl (1 M) at pH 8.5 for 7 min at a flow rate of 10 μL min^{-1}. Immediately after streptavidin immobilization, the surface was washed with three consecutive 30 s injections of a 50 mM NaOH/1 M NaCl solution, followed by two 15 s injections of 0.05% SDS and three 60 s injections of running buffer. Then, after a stable baseline was achieved, biotin-bound OP_{ureA}, diluted at 6.25 nM in running buffer, was captured over the active flow cell at 5 μL min^{-1} flow rate. Subsequently, three consecutive 15 s injections of SDS 0.05 % and several 180 s injections of running buffer were performed in order to remove any loosely bound DNA and stabilize the surface.

Following the immobilization process, Ni(II)-*Hp*NikR and apo-*Hp*NikR samples were delivered in a wide range of concentrations (2 to 1000 nM) over the sensor surface in order to assess the biological activity of the tethered OPureA. The specificity of the molecular recognition was also evaluated in a similar experimental setup, where Ni(II)-*Hp*NikR samples prepared at five different concentrations (0.2, 1.0, 5.0, 50, and 125 nM), either in the absence or the presence of equimolar amount of soluble non-biotinylated OP_{ureA}, were incubated for at least 30 min, and injected over the functionalized surface. Finally, the contribution of the mass transport limitation (MTL) to the overall interaction was assessed.

Ni(II)-HpNikR–OPureA interaction analysis.

The Ni(II)-*Hp*NikR–OP_{ureA} interaction was analyzed using classical multi-cycle kinetic (MCK) and single-cycle kinetic (SCK) approaches over a broad series of protein concentrations, ranging from 2 to 1000 nM. Replicates for the interaction were collected over a total of three freshly prepared sensor chip surfaces, and results were independently fit to the appropriate binding model. Protein samples were delivered in a twofold or fivefold serial dilution, with association and dissociation events monitored for 180 and 400 s, respectively. Regeneration was achieved with two consecutive injections of 15 µL of SDS 0.2 % (w/v) and an additional stabilization period of 300 s, during which running buffer was flowed over the sensor chip surface.

For steady state analysis, Ni(II)-HpNikR samples were delivered from the lowest to the highest concentration (2, 4, 8, 16, 31, 63, 125, 250, 500 and 1000 nM). Intermediate concentrations (8, 16, 31, 63 nM) were injected in duplicate.

For MCK experiments, Ni(II)-*Hp*NikR was injected from 2.3 nM to 300 nM in a two-fold serial dilution; intermediate concentrations (9.4, 18.8, 37.5 nM) were injected in duplicate in random order to monitor the stability of the system and buffer was injected every four cycles as blank for double referencing purposes. For SCK experiments, Ni(II)-*Hp*NikR was injected from 2 to 1000 nM in a five-fold dilution, dissociation was monitored for an extended period of 600 s.

In order to investigate the time-dependence of the reaction, the protein was also injected at a fix concentration of 500 nM with three different contact times (60, 120, and 180 s).

The effect of Ni(II) concentration in the environment on the *Hp*NikR–OP_{ureA} interaction was assessed by incubation of 200 nM apo-*Hp*NikR solutions with different equivalents of Ni(II) per tetramer, yielding samples with 0:1, 1:1, 2:1, 3:1, and 4:1 metal-to-protein ratios. Then, the five different solutions were delivered in random order over the active surface. To avoid Ni(II) contamination among samples, a regeneration step, consisting of a 60-s injection of 300 mM EDTA at pH 8.0 in water followed by a 180-s injection of running buffer, and a stabilization period of 300 s, was performed.

Data evaluation

Signals arising from the active flow cell were corrected for the signals generated from the reference flow cell, and against an average of the blank injections performed during the analysis to obtain double-referenced sensorgrams[113]. For the steady state analysis, the equilibrium response (resonance units, RU) reached 5 s before the injection stops was measured and plotted against the

protein concentration to obtain the equilibrium dissociation constant K_D. Data sets were analyzed assuming a 1:1 isotherm binding model, defined by the Eq. (4).

For kinetic and mechanistic analysis, real-time interaction curves (sensorgrams) were globally fitted to three different theoretic models: 1:1 binding, heterogeneous binding, and two-state reaction, equation 5, 6 and 7 respectively. Sensorgrams traces obtained for the Ni(II)*Hp*NikR–OP_{ureA} interaction were globally fitted to three different interaction models: two-state, 1:1 binding and heterogeneous binding. Each fitting model is reported with the associated statistical parameter χ^2, expressing the goodness of fit.

The 1:1 binding, the heterogeneous ligand binding and the two-state binding models are extensively discussed in the results section while the heterogeneous binding scenario has been ruled out. Evidences against its use are presented and will be briefly discussed here. The heterogeneous analyte binding takes place when two species compete for the same binding site on the immobilized ligand, and it is primarily intended to be used when two analytes of different molecular weight are deliberately mixed in solution[195]. In those conditions, the binding of the low molecular weight analyte is hardly detected, but because it involves binding sites on the surface, it will affect the observed sensorgrams. In principle, a situation where two different populations of the same analyte are together in solution can also give rise to a heterogeneous analyte binding scenario. We ruled out this circumstance for the system under investigation, because a fitting procedure based on this model, considering 10% of the total concentration represented by a different analyte of the same molecular weight as holo-NikR, resulted in a quantitatively worse description of the binding process as compared to the other multi-components models applied. Furthermore, this fitting procedure is not able to take into account the time-dependency, which strongly characterizes the monitored interaction. Moreover, the presence of previous data proposing an induced-fit mechanism between holo-*Hp*NikR and OP_{ureA}, strongly supported the proposed two-state reaction, which was employed to extrapolate kinetic rate constants from the SPR analysis. During data evaluation, residual plots and the statistical parameter χ^2 were used to choose the best theoretical description of the experimental results and to extrapolate the kinetic rate constants. Data collected for the samples containing different equivalents of Ni(II) per *Hp*NikR tetramer were fitted independently to the two-step interaction model. Kinetic analysis in these latter experiments should be taken as a qualitative description of the binding event rather than quantitative, because the interactions were monitored for a single protein concentration.

Isothermal titration calorimetry

All ITC experiments were performed in 20 mM HEPES buffer at pH 7.0, containing 150 mM NaCl, under identical conditions as previously reported for the dsDNA titration of apo-*Hp*NikR and Ni(II)-*Hp*NikR[186]. In order to derive the kinetic parameters of the *Hp*NikR–OP_{ureA} interaction, ITC data obtained from the titration of dsDNA onto Ni(II)-*Hp*NikR[186] were used as input for equilibration–time curve (ETC) analysis[182] performed using the AFFINImeters software (https://www.affinimeter.com/). This method provided an ETC curve that shows the equilibration time T (the time that heat trace needs after every injection to go back to baseline) versus the Ni(II)-*Hp*NikR stoichiometric ratio. A fit of the experimental data was performed according to Eq. 8, considering an instrumental response time of 8.2 ± 0.5 s, as indicated by the manufacturer:

$$T = \frac{1/c}{k_{off}\left[(1/c + s + 1)^2 - 4s\right]^{1/2}} \qquad (8)$$

where c = [*Hp*NikR]/K_D, K_D and k_{off} are the equilibrium and kinetic dissociation constants, respectively, and s = [OP_{ureA}]/ [*Hp*NikR]. This method allowed us to calculate k_{off} for a single-step interaction model. The association kinetic constant k_{on} was derived using the equation $K_D = k_{on} / k_{off}$, based on the K_D value previously reported for the Ni(II)-*Hp*NikR–OP_{ureA} interaction[186]. The data points of the ETC that occur after the binding saturation were deleted using the default option of the AFFINImeter software, as they only describe the dsDNA dilution in the protein solution, and have a low signal-to-noise ratio. In order to derive the thermodynamic parameters for the interaction of *Hp*NikR loaded with two equivalents of Ni(II), a OP_{ureA} solution (40 µM, 30 × 10 µL injections) was titrated onto a protein solution (4 µM) in the presence of 8 µM Ni(II), as previously described[186]. Integration of the raw data to obtain the binding isotherm was performed using NITPIC program[196].

8. Stopped-Flow Enantioselective HPLC-CD Analysis and TD-DFT Stereochemical Characterization of Methyl Trans-3-(3,4- Dimethoxyphenyl)Glycidate

(**Edoardo Fabini,** Daniele Tedesco, Vakhtang Barbakadze, Maia Merlani, Riccardo Zanasi, Bezhan Chankvetadze and Carlo Bertucci).

Chirality (2015) 27(12):914–8

Doi: 10.1002/chir.22539

Abstract

Caffeic acid-derived polyethers are a class of natural products isolated from the root extracts of comfrey and bugloss, which are endowed with intriguing pharmacological properties as anticancer agents. The synthesis of new polyether derivatives is achieved through ring-opening polymerization of chiral 2,3-disubstituted oxiranes, whose absolute configurations define the overall stereochemistry of the produced polymer. The absolute stereochemistry of one of these building blocks, methyl trans-3-(3,4-dimethoxy-phenyl)glycidate (3), was therefore characterized by the combination of enantioselective high-performance liquid chromatography (HPLC), electronic circular dichroism (ECD) spectroscopy, and time-dependent density functional theory (TD-DFT) calculations. Initial efforts aiming at the isolation of enantiomers by means of a standard preparative HPLC protocol followed by offline ECD analysis failed due to unexpected degradation of the samples after collection. The stopped-flow HPLC-CD approach, by which the ECD spectra of enantiomers are measured on-line with the HPLC system, was applied to overcome this issue and allowed a fast, reliable, and chemical-saving analysis, while avoiding the risks of sample degradation during the collection and processing of enantiomeric fractions. Subsequent TD-DFT calculations identified (2S,3R)-3 as the first eluted enantiomeric fraction on the Lux Cellulose-2 column, therefore achieving a full stereochemical characterization of the chiral oxirane under investigation.

Introduction

Enantiomerically pure oxiranes are a valuable class of chiral compounds currently employed in synthetic organic chemistry as electrophilic synthons for several industrial and pharmaceutical applications, such as the synthesis of polyethers through ring-opening polymerization[197-200]. A new series of caffeic acid-derived polyethers (Fig. 31), poly[3-(3,4-dihydroxyphenyl)glyceric acid] **(1)** and poly[methyl-3-(3,4-dihydroxyphenyl)glycerate] **(2),** was isolated and identified in the water-soluble, high-molecular weight (>1000 kDa) fraction obtained from root extracts of different species of comfrey (Symphytum asperum, S. caucasicum, and S. officinale) and bugloss (Anchusa italica), all belonging to the Boraginaceae family[201-203].

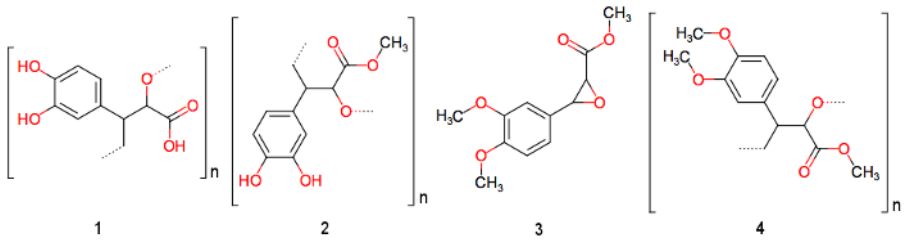

Figure 31 | Chemical structures of the caffeic acid-derived polyethers mentioned in the article (compounds 1, 2, and 4) and of methyl 3-(3,4-dimethoxyphenyl) glycidate (compound 3)

The immunomodulatory properties of polyethers **1** and **2** were assessed by in vitro and in vivo assays, which also unveiled excellent antineoplastic activity against human prostate cancer, as shown by the dose-dependent inhibition of 22Rv1-induced tumor growth in athymic mice, and antimetastatic properties against melanoma cell lines, as demonstrated by the inhibition of B16M cell adhesion to cultured hepatic sinusoidal endothelial cells[204]. Considering the

pharmacological profiles of polyethers 1 and 2, the synthesis of new caffeic acid-derived polyethers would constitute a promising route toward the development of potential drug candidates.

Recently, the use of 3-arylglycidic acid derivatives as chiral building blocks for the production of such polyethers has been reported; in particular, ring-opening polymerization of methyl 3-(3,4-dimethoxyphenyl)glycidate (**3,** Fig. 31) led to the formation of poly[methyl 3-(3,4-dimethoxyphenyl) glycerate] (**4**, Fig. 31), a fully methylated analog of the natural polyethers **1** and **2**[205] (Fig. 31). The structure of polymer **4** was found to be linear, despite the low reactivity of bulky 2,3-disubstituted oxiranes and the possible formation of branched polymers by Friedel-Crafts alkylation of the aromatic substituent. However, the stereoselectivity of the mechanism of ring opening and the stereochemistry of the resulting backbone are not fully characterized; the first step needed for the elucidation of these aspects is the assessment of the absolute configuration of the building block.

Compound 3 can be synthesized by Darzens condensation[206] of veratraldehyde with methyl chloroacetate yielding a racemic mixture of the pure trans-diastereomer as confirmed by 1^{H}-NMR analysis[205], or by Shi epoxidation[207] of methyl 3,4-dimethoxycinnamate with oxone.

In both situations, the relative configuration of the substituents on the oxirane ring is known; as a consequence, a complete stereochemical characterization of trans-3 requires further analyses on its purified enantiomers. If a chiral compound is not obtained as a pure enantiomer through synthesis, as in the case of trans-3, separation techniques such as enantioselective high-performance liquid chromatography (HPLC) can be employed in combination with chiroptical spectroscopies, such as electronic circular dichroism (ECD), in order to assign the

correct absolute configuration to its enantiomers. Two possible strategies can be used for this purpose: 1) isolation of the enantiomers by preparative enantioselective HPLC followed by offline ECD spectroscopic analysis on the purified enantiomeric fractions; 2) hyphenation of HPLC with an ECD detection system (labeled HPLC-CD to avoid confusion with electrochemical detection) and online determination of the ECD spectra of enantiomers during the enantioselective HPLC separation by means of stopped-flow measurements[80, 208]. The preparative HPLC approach is useful beyond the purposes of stereochemical characterization, allowing the preparation of highly pure enantiomeric samples in the absence of enantioselective synthetic procedures[209]. The HPLC-CD approach, on the other hand, provides a valuable analytical tool to avoid the time-consuming collection of pure enantiomers; moreover, the risk of contamination and degradation of collected samples, arising by the necessary step of solvent evaporation, is completely avoided.

ECD spectroscopy is able to provide all the necessary information at the molecular level for discrimination and characterizion of the absolute configuration of chiral molecules[84]; nevertheless, the observed properties cannot be readily translated into the corresponding chemical structures. The chiroptical properties of enantiomers must therefore be derived by means of an appropriate theoretical method and subsequently compared to the experimental results.

Currently, quantum chemical calculations based on time-dependent density functional theory (TD-DFT) is the most popular approach for stereochemical characterization studies on pharmaceutical compounds, thanks to their accurate predictions of the molecular properties (including ECD) for medium-to-large sized molecules with relatively limited computational effort[210, 211].

This article reports the stereochemical characterization of the enantiomers of trans-3, whose absolute configurations have been assessed by means of enantioselective HPLC, ECD spectroscopy, and TD-DFT calculations; both the preparative HPLC and the stopped-flow HPLC-CD strategies were applied, and the advantages of the stopped-flow approach for the analysis of trans-3 are discussed.

Results and Discussion

Preparative HPLC and Offline ECD Analysis

The collection of the enantiomeric fractions of trans-3 was carried out on a Lux Cellulose-4 column (CSP: cellulose tris (3-methyl-4-chlorophenylcarbamate)), which provided long retention times (t_0 = 1.65 min; k_1 = 18.60; k_2 = 35.15) and high enantioselectivity (α = 1.89)[212]; the chromatographic performance of Lux Cellulose-4 was therefore suitable for a preparative HPLC application.

Unfortunately, the offline ECD and UV spectra of the resulting fractions, as obtained after collection, evaporation of the mobile phase, and dissolution in 2-propanol, showed an unexpected behavior (Fig. S1 in the Supporting Information of the original article). Although the ECD profiles in the high-energy spectral region (λ < 250nm) displayed mirror-image bands of equal magnitude and opposite sign, the broad low-energy ECD band was found to be negative for both samples, indicating that the analyzed fractions were not in enantiomeric relationship. Furthermore, the shifts observed for the absorption maxima in the UV spectra of both samples with respect to the racemic mixture was strong

experimental evidence leading to the conclusion that a chemical transformation of the collected enantiomeric fractions of trans-3 had occurred.

Stopped-Flow HPLC-CD Analysis

The enantiomers of trans-3 can be easily separated with high values of enantioselectivity and resolution on most of the commercially available polysaccharide-based chiral stationary phases (CSPs)18; as a consequence, the enantioselective HPLC analyses on trans-3 described in this article were performed on two different columns, namely, Lux Cellulose-4 and Lux Cellulose-2 (CSP: cellulose tris(3-chloro-4-methylphenylcarbamate)). The latter column is able to resolve the enantiomers of trans-3 with slightly lower enantioselectivity than the former (α = 1.81); however, the shorter retention times (t_0 = 2.96 min; k_1 = 6.55; k_2 = 11.86) and the excellent resolution (Rs = 10.24) provided by Lux Cellulose-2 (Fig. 32) were more suitable for analytical purposes and therefore preferred for the application of the stopped-flow HPLC-CD approach.

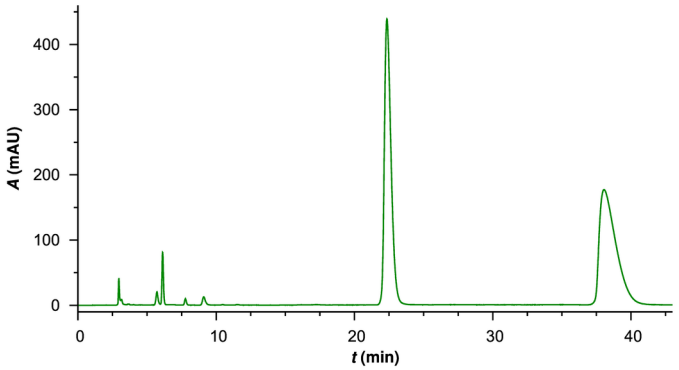

Figure 32 | Enantioresolution of trans-3 on the Lux Cellulose-2 column (mobile phase: n-hexane/2-propanol, 80:20 v/v; flow rate: 1 mL min 1; λ = 240 nm).

The stopped-flow spectra of the two chromatographic fractions show a clear mirror-image relationship of all the ECD bands in the whole spectral range of analysis and a close correspondence of the absorption UV profiles with respect to rac-trans-3, suggesting that the two fractions are indeed in enantiomeric relationship (Fig. 33).

The analytical protocol for stopped-flow measurements was developed in order to reduce the influence of baseline drifts to a minimum and to improve the signal-to-noise ratio of the spectroscopic response, which is an important issue of online HPLC-CD measurements. The developed stopped-flow HPLC-CD strategy was therefore successfully employed to acquire high-quality experimental ECD spectra of the enantiomers of trans-3, bypassing the collection step required by the preparative HPLC approach and drastically reducing the risk of degradation.

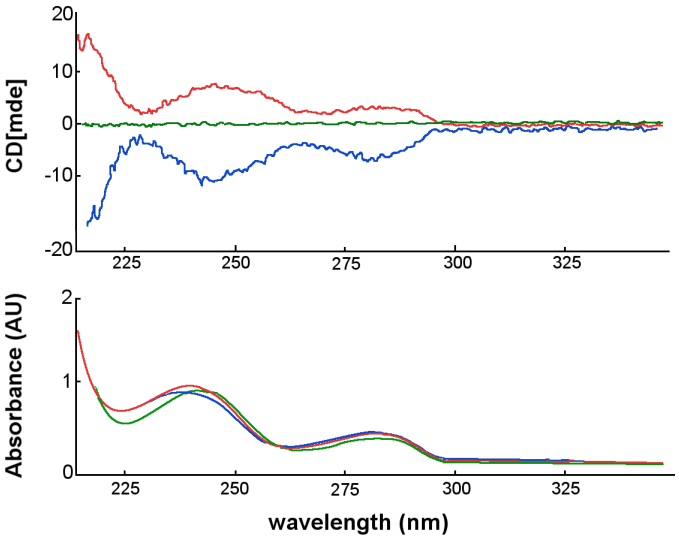

Figure 33. ECD and UV spectra of rac-trans-3 (in 2-propanol) and of the enantiomeric fractions of trans-3 (in mobile phase), as measured by stopped-flow HPLC-CD analysis on the Lux Cellulose-2 column. Solid: first eluted fraction. Dashed: second eluted fraction. Dotted: rac-trans-3

Absolute Configuration Assessment

The last step of the characterization process was aimed at the theoretical determination of the chiroptical properties of (2S, 3R)-3 by means of TD-DFT calculations. The preliminary MM conformational search on (2S, 3R)-3 identified 34 low-energy conformers (Table S1 in the Supporting Information of the original article), which were subsequently optimized at the RI-B97D/ def2-TZVPP'D/IEFPCM level. The conformational flexibility of trans-3 (Figure S2, Table S2, in the Supporting Information of the original article) is limited to the orientation of substituents with respect to the oxirane ring (dihedrals α and β for the methoxycarbonyl and 3,4-dimethoxyphenyl substituents, respectively) and to the orientation of the methoxy groups (dihedrals φ, ω1, and ω2 for the methoxycarbonyl, 3-methoxyphenyl, and 4-methoxyphenyl groups, respectively).

After DFT optimization, some conformers converged to the same geometry, reducing the number of equilibrium conformers to 28 after clustering; the limited flexibility of (2S, 3R)-3 was confirmed by the observation that the four lowest-energy geometries account for almost 90% of equilibrium conformers (Table S3 in the Supporting Information of the original article), with conformer (2S, 3R)-3.25 being by far the most populated (χ^G=45.4%). The subsequent TD-DFT calculations at the PBE0/def2-TZVPP'D/ IEFPCM level were performed on the 10 conformers showing ΔG values within the threshold of 2.5 kcal/mol^{-1}. The conformationally averaged theoretical spectra of (2S,3R)-3 (Fig. 34) show that the three main absorption bands are expected to give rise to positive Cotton effects: although the employed TD-DFT level generally overestimates the transition energies of trans-3, the ECD and UV profiles are reproduced with a reasonable degree of accuracy and allow assigning a (2S, 3R) absolute configuration to the first eluted fraction on the

Lux Cellulose-2 column. Consequently, the elution order of the enantiomers of trans-3 on the Lux Cellulose-2 column, under the chromatographic conditions used in this study, was found to be: (2S, 3R)-3, (2R, 3S)-3.

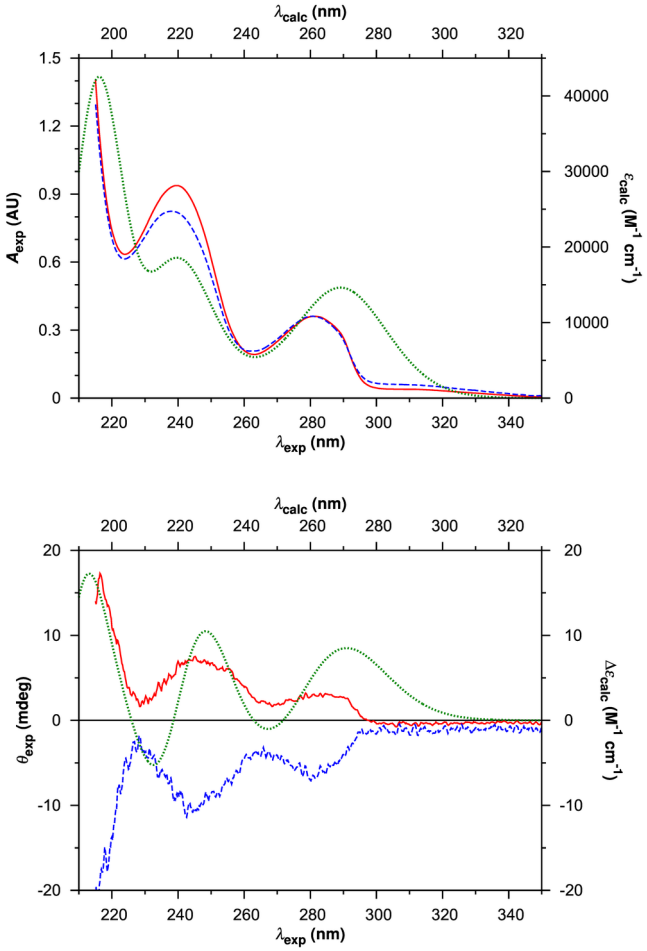

Figure 34 | Stopped-flow ECD and UV spectra of the enantiomeric fractions of trans-3 eluted from Lux Cellulose-2 (bottom/left axes), compared to the theoretical spectra of (2S,3R)-3 (top/right axes). Solid: stopped-flow first eluted fraction. Dashed: stopped-flow second eluted fraction. Dotted: theoretical spectra.

Conclusion

In this article the absolute stereochemistry of the 3-arylglycidic acid derivative trans-3 was successfully characterized by the combination of enantioselective HPLC, ECD spectroscopy, and TD-DFT calculations. Knowledge of the absolute configuration for the enantiomers of this chiral building block is an important prerequisite for elucidating the stereoselectivity of its polymerization by ring opening, ultimately leading to a better stereochemical control in the synthesis of caffeic acid-derived polyethers, a new class of biologically active molecules of natural origin. The discrimination between the enantiomers of trans-3 was initially attempted using a preparative HPLC protocol, in which the enantiomeric fractions were isolated and processed for an offline ECD analysis; unfortunately, the application of this standard approach failed due to the realistic occurrence of incidental sample degradation during the post-collection processing of fractions. The solution to this unexpected problem was provided by the stopped-flow HPLC-CD strategy, which provided a fast, reliable, and chemical-saving alter- native for the acquisition of the experimental ECD and UV spectra of the enantiomers of trans-3 while avoiding the risk of post-collection degradation. In this framework, the hyphenation of enantioselective HPLC methods with detection systems based on ECD spectroscopy was confirmed as a powerful analytical tool for the stereochemical characterization of chiral molecules, in particular when combined with computational methods based on the TD-DFT calculation of theoretical chiroptical properties.

Material and Methods

HPLC-CD analysis

Preparative HPLC Collection

Racemic methyl trans-3-(3,4-dimethoxyphenyl)glycidate (rac-trans-3) was synthesized by Darzens reaction, according to a reported procedure[205]; veratraldehyde and methyl chloroacetate were purchased from TCI (Tokyo, Japan). The enantiomers of trans-3 were then obtained by preparative HPLC collection performed on an Agilent (Waldbronn, Germany) 1200 HPLC system equipped with a G1367C HiP ALS-SL autosampler, a G1316B TCC-SL temperature controller, a G1311A quaternary pump, a G1314D VWD variable wavelength detector (detection wavelength: 220 nm), and the Chemstation software package (v. B.03.02-SR2) for instrument control and data processing. The enantioresolution of trans-3 was achieved on a Lux Cellulose-4 column (250 × 4.6 mm I.D, 5 μm particle size), kindly provided by Phenomenex (Torrance, CA), using a n-hexane/2-propanol 80:20 (v/v) mixture as mobile phase at a 1 mL min^{-1} flow rate, following a previously reported protocol[212]. HPLC-grade solvents were purchased from Carl Roth (Karlsruhe, Germany). The collected fractions were subsequently dried under vacuum and submitted to spectroscopic analysis.

Offline ECD Analysis

Offline ECD and UV analysis was carried out in the 350–200 nm spectral range on rac-trans-3 and on the two enantiomeric fractions collected after resolution on the Lux Cellulose-4 column. Samples were prepared in HPLC-grade 2-propanol (Sigma-Aldrich, Milan, Italy) at a nominal concentration of 0.015 mg mL^{-1} for the two collected enantiomeric fractions, while a 0.05 mg mL^{-1} concentration was used for rac-trans-3. Spectra were measured on a Jasco (Tokyo, Japan) J-810 spectropolarimeter equipped with a PTC-423S Peltier-type temperature control system, using a 1mm pathlength quartz cell (Hellma, Milan, Italy), a 2 nm spectral bandwidth, a 50 nm min^{-1} scanning speed, a 2 s data integration time, a 0.2 nm data pitch and three accumulation cycles. Instrument control and data processing were performed with the Jasco Spectra Manager 2 software package.

Stopped-Flow HPLC-CD Analysis

The spectroscopic analysis was repeated using the stopped-flow HPLC-CD technique on an HPLC system consisting of a Jasco PU-980 pump, a LG-2080-02 ternary gradient unit, a DG-2080-53 degasser, a Jones (Lakewood, CO) model 7955 column chiller, a Rheodyne (Cotati, CA) 7725i syringe loading injector, and a 20 μL sample loop; this system was connected to the Jasco J-810 spectropolarimeter, equipped with a 10 mm pathlength HPLC flow cell and a Rheodyne 7010 injector setup as a three-way valve for stopped-flow measurements. The enantioresolution was achieved on a Lux Cellulose-2 column (250×4.6mm I.D, 3μm particle size), purchased from Phenomenex (Castel Maggiore, Italy), using a n-hexane/2-propanol 80:20 (v/v) mixture as mobile phase at a 1 mL min^{-1} flow rate, in accordance with a previously published study on the enantioresolution of chiral 3-arylglyceric acid derivatives[212]; HPLC-grade solvents were purchased from Sigma-Aldrich. The analysis was carried out on 0.5 mg mL^{-1} samples of rac-trans-3 dissolved in mobile phase. The enantiomeric fractions of rac-trans-3 were then stopped inside the HPLC flow cell during their elution and analyzed by full-spectrum ECD spectroscopy in the 350–215nm spectral range, using a 4 nm spectral bandwidth, a 50 nm min^{-1} scanning speed, a 1 s data integration time, a 0.2 nm data pitch and three accumulation cycles. Stopped-flow spectra were blank-corrected using stopped-flow measurements of the mobile phase in the same conditions, which were repeated before and after each measurement on the fractions in order to correct baseline drifts. Each enantiomeric fraction was analyzed three times according to this protocol, and the resulting stopped-flow spectra were normalized at the maximum of the lowest-energy absorption band (λ_{max} = 281 nm) in order to account for the different instantaneous concentrations inside the HPLC flow cell. Instrument control and data processing were performed with the Jasco ChromNav and Spectra Manager 2 software packages.

Computational spectroscopy

DFT Conformational Analysis

A preliminary molecular mechanics (MM) conformational search was carried out on (2S, 3R)-3 using the MMFF94s force field19 and the Spartan'02 software package[213]. A relative energy (ΔEMM) threshold value of 5 kcal mol 1 was used to identify the lowest-energy conformers. DFT geometry optimization and frequency calculations were carried out on the identified MM conformers using the Gaussian 09 (Rev. D.01) software package[214]. The dispersion-corrected

generalized gradient approximation functional B97D[215] was used in combination with the IEFPCM solvation model for 2-propanol[216], the resolution of identity (RI) approximation[217], and a truncated version of the Ahlrichs-type, triple-ζ valence plus double polarization basis set, devoid of d functions on hydrogen atoms and f functions on heavy atoms and augmented with a set of diffuse functions (def2-TZVPP'D)[211, 218]. Conformational clustering was performed on optimized geometries having root mean square deviations (RMSD) below 0.001 Å for heavy atoms; geometry alignment and RMSD determination were performed using the VMD molecular graphics software[219]. A relative free energy (ΔG) threshold value of 2.5 kcal mol^{-1} was used to identify the low-energy equilibrium conformers for TD-DFT calculations. Boltzmann statistics at 298.15 K and 1 atm was subsequently employed to determine the population of conformers at equilibrium based on ΔG values (χ^G).

TD-DFT Computational Spectroscopy

TD-DFT calculations were performed on the optimized conformers of (2S, 3R)-3 using the Gaussian 09 (Rev. D.01) software package[214]. The exchange-correlation PBE0 functional[220-222] was used in combination with the IEFPCM solvation model for 2-propanol[216] and the truncated def2-TZVPP'D basis set[211, 218]. The theoretical values of rotational strengths (Rj), oscillator strengths (fj), and excitation wavelengths (λj) were calculated for the 50 lowest-energy electronic transitions of each conformer; the corresponding theoretical ECD and UV spectra were derived by approximation of Rj and fj values to Gaussian functions of defined bandwidth (Δσ = 0.3 eV) and summation over all excited states[210, 223]. The overall ECD and UV spectra of (2S,3R)-3 were derived by conformational averaging according to the ΔG-based Boltzmann distribution of conformers, and subsequently compared to the experimental spectra of the enantiomeric fractions recorded in stopped-flow mode during the HPLC analysis on the Lux Cellulose-2 column. Detailed results for the computational study on trans-3 are given in the Supporting Information on the original article.

9. A SMYD3 Small-Molecule Inhibitor Impairing Cancer Cell Growth

This chapter is adapted from: (Alessia Peserico, Aldo Germani, Paola Senese, Armenio J. Barbosa, Valeria Di Virgilio, Raffaele Fittipaldi, **Edoardo Fabini**, Carlo Bertucci, Greta Varchi, Mary P. Moyer, Giuseppina Carretti, Alberto Del Rio and Cristiano Simone)
Journal of Cellular Physiology (2015) 230: 2447–2460.

Doi: 10.1002/jcp.24975

Abstract

SMYD3 is a histone lysine methyltransferase that plays an important role in transcriptional activation as a member of an RNA polymerase complex, and its oncogenic role has been described in different cancer types. In the present study, the expression and activity of SMYD3 was investigated in a preclinical model of colorectal cancer (CRC) and a strong upregulation throughout tumorigenesis both at the mRNA and protein level was found. Results showed that RNAi-mediated SMYD3 ablation impairs CRC cell proliferation indicating that SMYD3 is required for proper cancer cell growth. These data, together with the importance of lysine methyltransferases as a target for drug discovery, prompted a virtual screening to identify new SMYD3 inhibitors by testing several candidate small molecules. One of these compounds (BCI-121) induces a significant reduction in SMYD3 activity in CRC cells, as suggested by the analysis of global H3K4me2/3 and H4K5me levels. SPR analysis further supported the *in silico* and *in vivo* findings. The mode of action for BCI-121 was tested through a competition assay, in which H4 and BCI-121 contend the methylation pocket on SMYD3. The presence of the inhibitor in solution lowered considerably the response of H4 alone, indicating competition for the same binding site occurred. These results represent the proof of principle that SMYD3 is a druggable target and suggest that new compounds capable of inhibiting its activity may prove useful as novel therapeutic agents in cancer treatment.

Introduction

Cancer cell fate is governed by an intricate network of signaling pathways that intersect with epigenetic regulators at the chromatin level. Indeed, any altered signaling cascade can induce a perturbation of chromatin structure and functions, resulting in modulation of gene expression[224, 225]. Major mechanism regulating chromatin dynamics is the post-translational modification of histone proteins. Histone methylation is an important and widespread type of chromatin modification that is known to affect biological processes involved in several types of cancer[226-229].

The histone methyltransferase SET/MYND Domain Type of Zinc Finger (SMYD3), a member of the subfamily of SET domain-containing proteins[230], has been found overexpressed in different types of tumors: breast, gastric, pancreatic, colorectal, lung cancer, and hepatocellular carcinoma[231-233]. Importantly, it has been demonstrated that complete loss of SMYD3 function does not lead to a visible phenotype in mouse models, suggesting that the use of small molecules capable of impairing SMYD3 activity as new anticancer agents might be associated with reduced side effects compared with other chemotherapeutics.

However, SMYD3 overexpression in normal cells is sufficient to accelerate cell growth and has a key role in the activation of genes downstream of pathways involved in tumor cell transformation and migration[234, 235]. Several studies have been designed to explore the oncogenic activity of SMYD3. Initially, SMYD3 was described as a histone H3K4-specific di- and tri-methyltransferase eliciting its oncogenic effect through transcriptional activation of its downstream target genes[236-238]; however, recent studies identified histone H4K5 as a preferred substrate in *in vitro* binding assays. Besides, it has been shown that SMYD3 is

required for H4K5 methylation in culture and that its enzymatic activity is important for maintaining the transformed cellular phenotype associated with high SMYD3 expression[239].

SMYD3 oncogenic activity also involves functional interactions with non-histone proteins (e.g., VEGFR1, estrogen receptor [ER]) in the cytoplasm that regulate cancer cell proliferation and survival. Indeed, SMYD3 methylates VEGFR1, thereby enhancing its kinase activity in cancer cells, and acts as a coactivator of ER in breast cancer cells[240-242]. Furthermore, mutated KRAS correlates with SMYD3 upregulation in CRC, and methylation of MAP3K2 by SMYD3 increases MAP kinase signaling, thereby promoting the development of lung and pancreatic cancer[232, 243].

Indeed, while other epigenetics drugs targeting EZH2, another component of the lysine(K)-methyltransferases (KMTs) family, are currently in clinical trials for the treatment of various human cancers, no SMYD3-specific compound has been identified so far. After testing several compounds, we identified a piperidine-4-carboxamide acetanilide compound (BCI-121) that was effective in cell lines at low micromolar concentrations and was able to impair SMYD3-mediated H4 methylation in vitro, showed antiproliferative properties in cancer cell lines overexpressing SMYD3 and, in general, replicated the effects of SMYD3-targeted RNAi.

By means of molecular docking techniques we identified a small-molecule compound (BCI-121) which significantly inhibits SMYD3-substrate interaction and chromatin recruitment and is effective in reducing proliferation in various cancer cells types. These findings were supported with SPR analysis, where the

compounds and natural SMYD3 substrate H4K5, were tested for competition for the methylation pocket on the enzyme.

Results and Discussion

Molecular modeling & Dose-dependence of BCI-121 treatment in cells line

Based on the crystallography structure of SMYD3, we took advantage of molecular design techniques to search for new small molecules that could inhibit its catalytic activity. Since no previous knowledge on specific SMYD3 inhibitors was available, our selection was based on the conformations of the substrate binding site and on the possibility to accommodate specific molecules.

The substrate binding site is formed within the SET and post-SET domains and consists in a deep and narrow substrate binding pocket where the structure of BCI-121 is predicted to bind. A closer look at this binding mode suggests that the 4-carboxamide moiety of the piperidine ring is oriented toward the cofactor binding site and forms two hydrogen bonding interactions with Ser202. The carbamoyl group undergoes another hydrogen bonding between the nitrogen of the amide group and the backbone of Tyr239. All other interactions are basically formed with the hydrophobic residues that comprise the narrow binding pocket of the histone lysine residue, consistent with the hydrophobic nature of its alkylic side chain **(**Fig. 35 and in the Supporting Information of the original article).

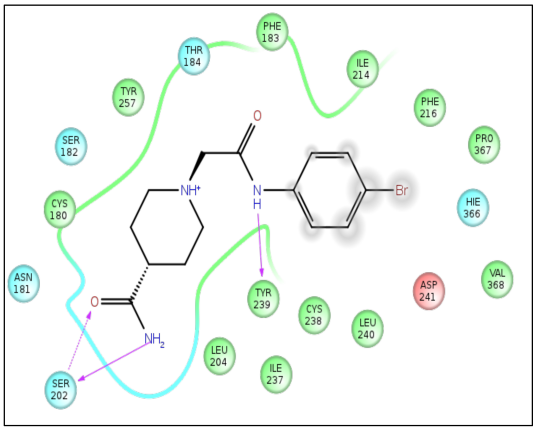

Figure 35 | Chemical scaffold and interactions made in the binding pocket of SMYD3 by BCI-121.

These results prompted us to test the ability of BCI-121 to affect histone binding to SMYD3 in cell line models. Thus, we envisioned to specifically target SMYD3 catalytic function by means of small-molecule inhibitors in order to preferentially target cancer cells.

Hence, we analyzed SMYD3 occupancy at binding sites located in the promoters of its target genes in two different cancer cell lines (HCT116 and OVCAR-3) treated or not with BCI-121. Our data confirmed that BCI-121 competes with histones for binding to SMYD3 also in a cellular setting, as shown by its reduced binding to the promoter region of target genes (Fig. 36a, b).

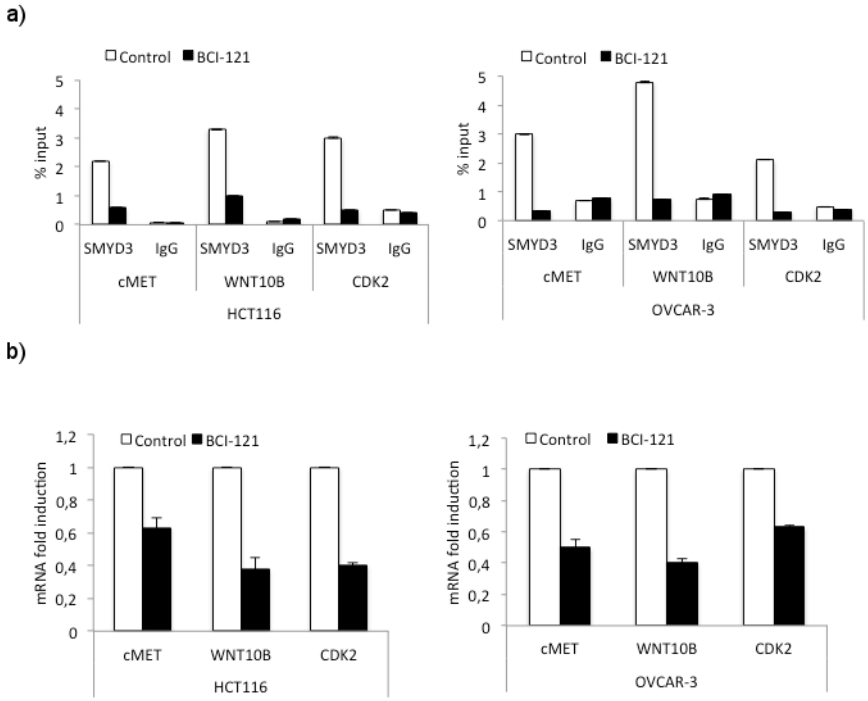

Figure 36 | (a) SMYD3 binding to the promoter of its target genes is abolished by the presence of BCI-121 in cancer cells. ChIP was performed in HCT116 and OVCAR-3 cells treated or not with BCI-121 (100 mM) for 72 h. Cells were cross-linked and immunoprecipitated with anti-SMYD3 and anti-IgG antibodies. The precipitated DNA was subjected to real-time PCR with specific primers, which amplify SMYD3 binding site elements of human target gene promoters (cMET, WNT10B, and CDK2). IgGs were used as an immunoprecipitation control. (**b)** Transcriptional activation of target genes correlates with impaired binding of SMYD3. b-actin was used for real-time PCR data normalization. Statistical analysis was performed using Student's t-tail test; *P < 0.05 was considered statistically significant.

In order to find the lowest concentration affecting SMYD3 activity in cell cultures, we established a dose-dependent curve for BCI-121 (1, 10, 30, 60, 100 mM) and evaluated its anticancer activity in a CRC cell line (HT29) by measuring the cell proliferation index and by evaluating the global level of methylation at SMYD3-targeted (H4K5me and H3K4me2) and non-targeted (H3K27me3) sites.

Our results show that there is a dose-dependent relationship between SMYD3 impairment and both inhibition of proliferation (Fig. 37a) and reduction of targeted methyl marks (H4K5me and H3K4me2) (Fig. 37b).

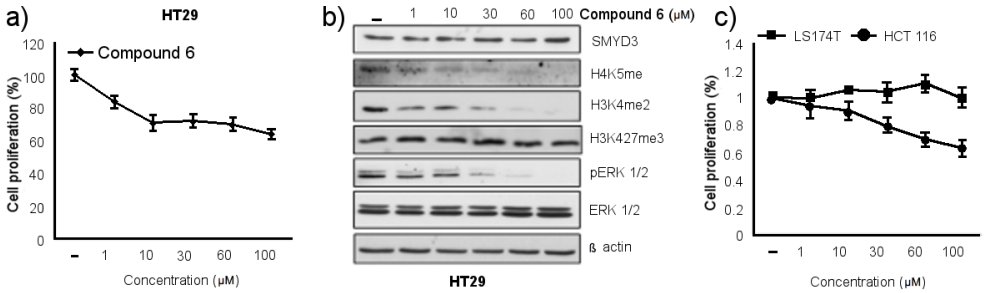

Figure 37 | Dose-dependence of BCI-121 treatment in CRC cell lines. (**a)** BCI-121 treatment for 48 h induces a concentration-dependent reduction of CRC cell proliferation and (**b**) decreases the global levels of targeted histone methyl marks [H4K5me, H3K4me2] and ERK 1/2 activation. A non-targeted methyl mark [H3K27me3] was not affected. b-actin was used as a loading control for immunoblotting. (**c**) The dose-dependent effect of BCI-121 treatment (72 h) on cell growth is observed in cells expressing high levels of SMYD3 (HCT116), but not in cells with low levels of SMYD3 (LS174T). Cell proliferation was calculated using the WST-1 assay. Statistical analysis was performed using Student's t-tail test; *P < 0.05, **P < 0.01, and ***P < 0.001 were considered statistically significant.

A similar correlation was also observed with the level of MEK-ERK signaling activity (Fig. 37b). Consistent with previous results, the dose-dependent effect on cell growth was detected in cancer cells expressing high levels of SMYD3 (HCT116 cells). while BCI-121 treatment failed to inhibit proliferation in cancer cells with low levels of SMYD3 (LS174T cells) (Fig. 38c). Collectively, these data indicate that BCI-121 reproduces the effects of SMYD3-targeted RNAi.

Collectively, these data indicate that BCI-121 reproduces the effects of SMYD3-targeted RNAi. Based on these data, we speculated that the use of specific inhibitors might help to gain a better understanding of the role of SMYD3

in tumorigenesis and could also be the basis for future pharmacological interventions.

Binding competition experiments in vitro by means of surface plasmon resonance.

In order to get further insight into the mechanisms underlying SMYD3 inhibition by BCI-121, we performed surface plasmon resonance experiments to investigate the binding modes of this compound with molecular modeling techniques.

The target protein SMYD3 was immobilized through an affinity capture method as a SMYD3-GST fusion protein to an anti-GST antibody covalently bound to a CM5 sensor chip. This oriented immobilization approach ensured that the histone binding site of SMYD3 was accessible for interaction. H4 histone binding to SMYD3 was analyzed at different analyte concentrations, and an affinity K_D of $1.18 \cdot 10^{-5}$ M was determined based on the association and dissociation rate constants ($k_{on} = 357.7 \pm 28.0$ M^{-1} s^{-1}; $k_{off} = 4.23 \times 10^{-3} \pm 2.9$ 10^{-5} s^{-1}; $K_D = k_{off} / k_{on}$, data in the supplementary material of the original manuscript).

Then, compound BCI-121 was assessed as a potential inhibitor of SMYD3/histone binding. H4 histone was injected at 72.03 µM, alone or in the presence of BCI-121, in 1:1 and 1:2.5 [histone peptide]:[BCI-121] molar ratios. At these ratios, BCI-121 inhibited histone H4 binding by 36.5% and 51.0%, respectively (Fig 38 and table 4), indicating that the mechanism foreseen by docking calculation can indeed occur through competition at the histone binding site.

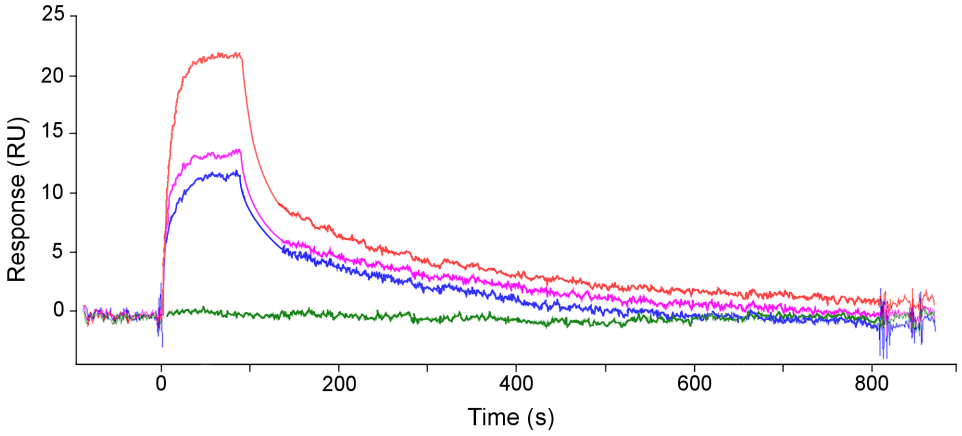

Figure 38 | Representative sensorgrams for BCI-121 competing with histones protein for SMYD3 binding in vitro. Sensorgrams of H4 histone binding to SMYD3 alone (red trace) and in the presence of BCI-121 at 1:1 molar ratio (magenta) and 2.5 :1 molar ratio (blue line).

	Response decrease (%)		
[BCI-121] : [Histone]	**1st replicate**	**2nd replicate**	**Total**
1 : 1	34.9	38.1	36.5
2.5 : 1	55.2	46.8	51.0

Table 4. Percentage of response decreasing when the histone protein binds to SMYD3 in the presence of BCI-121.

Conclusion

The US FDA recently approved three new epigenetic drugs for the treatment of specific human cancers, and small-molecule inhibitors targeting the KMT family component EZH2 are currently in clinical trials. However, despite the emerging pathophysiological role of SMYD3 in human cancer and its potential as a therapeutic target, no SMYD3 inhibitors have been identified so far[244]. A better understanding of the role of SMYD3 in tumorigenesis might prove useful for the

design of future pharmacological interventions. Indeed, a SMYD3-based therapeutic approach capable of inducing a cytostatic effect on different types of tumor cells could be a valuable tool in cancer treatment. The ability of BCI-121 to arrest cancer cells at the S/G2 boundary of the cell cycle suggests that this small molecule could improve the effects of conventional chemotherapy by acting on the DNA damage checkpoints, and it can be hypothesized that BCI-121 could also sensitize cancer cells to S/G2 phase-specific chemotherapeutic agents. Our study provides an important advancement in this research area, since it describes for the first time a non-peptide inhibitor of SMYD3. Indeed, these data represent the proof of principle that SMYD3 can be pharmacologically modulated by means of small-molecule inhibitors. We believe that these results may have a strong impact on the identification of new molecules amenable to use as novel therapeutic agents.

Overall, the results presented here hold the basis for the development of new classes of SMYD3 inhibitors for therapeutic use in different cancer types.

Indeed, cancer cells treated with BCI-121 showed a significant reduction in their growth ability and accumulated in the S phase of the cell cycle, suggesting that SMYD3 might be required for proper cell cycle progression through the S/G2 boundary. Efficacy of the selected compound was also demonstrated with histone competition experiments through SPR techniques.

Material and methods

Surface plasmon resonance (SPR)

Measurements were performed with a Biacore X100 optical biosensor (Uppsala, Sweden), thermostated at 25 °C. Evaluation of sensorgrams and data analysis was performed using the BiacoreTMX100 2.0.1 software. SMYD3 immobilization was obtained through affinity capture. The two flow cells were loaded independently with an anti-GST antibody using the amine coupling kit from BIAcore according to the standard procedure. The CM5 sensor chip was equilibrated at 25 °C and the system was primed three times using running buffer. A mixture of 1-ethyl-3-(3-dimethylaminopropyl)-carbodiimide hydrochloride (EDC) 0.4 M and N-hydroxysuccinimide (NHS). 0.1 M was freshly prepared and injected at 5 ml/min for 7 min. The anti-GST antibody was diluted at 30 mg/ml in sodium acetate pH 5.0 and injected at 5 ml/min for 180 sec, resulting in approximately 3,000 RUs for each flow cell. Injecting ethanolamine at 5 ml/min for 7 min deactivated the remaining active esters. The active flow cell was loaded with the SMYD3-GST fused protein solution, 2 mg/ml, until reaching approximately 300 RUs and the reference cell was loaded with an equimolar recombinant GST protein to reach approximately 150 RUs. The H4 peptide stock solution was prepared at 128.66 µM and serial dilutions at 64.82 µM, 32.41 µM, 16.21 µM, 1.47 µM were injected at 30 µl/min for 60 s over the surface and then the complex was allowed to dissociate for 720 s until reaching a level ` 2.0 RU relative to the baseline. The affinity K_D of the H4 peptide was derived from kinetic parameters (association and dissociation rate constants, k_{on} and k_{off}). Inhibition of H4 binding to SMYD3 by BCI-121 was obtained by dissolving the compound in running buffer and mixing it with the histone peptide at 1:1 and 2.5:1 ratios. The final concentrations were 72.03 µM for the histone peptide and 72.03 and 183.33 µM for the BCI-121 compound. The resulting solutions were injected at 30 µl/min and association was monitored for 100 sec, after which the running buffer was flowed and dissociation was monitored for 900 sec. Measurements were performed in duplicate and averaged; final results were obtained by subtracting the unspecific binding given by the reference flow cell and normalizing to the baseline injection.

Molecular biology and Docking studies

All details can be consulted on the original research article

10. Determination of levamisole and tetramisole in seized cocaine samples by enantioselective high-performance liquid chromatography and circular dichroism detection

(Carlo Bertucci, Daniele tedesco, **Edoardo Fabini**, Anna Maria Di Pietra, Francesca Rossi, Marco Garagnani, Elia Del Borrello, Vincenza Andrisano).

Journal of Chromatography A (2014) 1363: 150–154.

Doi: http://dx.doi.org/10.1016/j.chroma.2014.07.069

Abstract

Levamisole, an anthelmintic drug, has been increasingly employed as an adulterant of illicit street cocaine over the last decade; recently, the use of tetramisole, the racemic mixture of levamisole and its enantiomer dexamisole, was also occasionally observed. A new enantioselective high-performance liquid chromatography (HPLC) method, performed on cellulose tris(3,5-dimethylphenylcarbamate) chiral stationary phases in normal-phase mode, was validated to determine the enantiomeric composition of tetramisole enantiomers in seized cocaine samples. Furthermore, the hyphenation of the validated HPLC method with a circular dichroism (CD) detection system allowed the direct determination of elution order and a selective monitoring of levamisole and dexamisole in the presence of possible interferences. The method was applied to the identification and quantitation of the two enantiomers of tetramisole in seized street cocaine samples.

Introduction

Levamisole (Fig. 39) is a veterinary anthelmintic drug which was employed as a therapeutic agent for humans until the end of the 20th century, when it was withdrawn due to adverse side effects such as agranulocytosis, cutaneous vasculopathy and leukoencephalopathy[245].

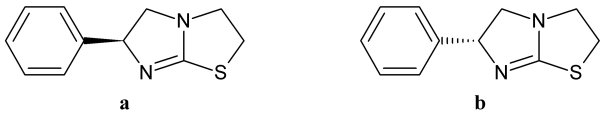

Figure 39 | Chemical structures of tetramisole enantiomers; **a**: levamisole; **b**: dexamisole.

Levamisole gained forensic interest after the increase of its use as an adulterant in illicit cocaine samples; as a result, levamisole is now found in the majority of cocaine seized worldwide, linked to debilitating and eventually fatal immunologic effects in cocaine abusers[246]. The use of levamisole as adulterant is likely due to its physicochemical properties, which are quite similar to those of cocaine, although being a much cheaper and more easily accessible substance[247].

Moreover, the presence of levamisole should hypothetically enhance the effects of cocaine, since a possible synergism for their interaction has been proposed[248]. Therefore, the health risks associated to the use of levamisole as adulterant are worth highlighting, due to possible high contents in some illicit street cocaine samples which can eventually exceed the content in pure cocaine[247]. The presence of levamisole determines an additional health threat due to aminorex, one of its main metabolites[249, 250]. Analytical assays for the determination of levamisole have been reported by gas chromatography–mass spectrometry (GC–MS) in human

urine samples[249] and by high-performance liquid chromatography–mass spectrometry (HPLC–MS) in cocaine samples[250].

Quite recently, the analysis on seized illicit cocaine samples showed that some manufacturing laboratories have begun using tetramisole, a racemic mixture of levamisole and its enantiomer dexamisole (Fig. 39), as a substitute for levamisole as adulterant. Therefore, the identification and determination of both enantiomers is essential for a better evaluation of the health risks arising from the presence of these adulterants, in view of the different biological activity of the two enantiomers[251] and the stronger adverse effects of dexamisole in humans. Furthermore, the enantiomeric composition of adulterants in seized samples of cocaine may help determining the origin of the illicit drug[251]. Enantioselective analyses on tetramisole have already been developed and performed by capillary GC with flame ionization detection (FID) using fused silica columns coated with cyclodextrin[252], by HPLC[253] and capillary electrophoresis (CE)[254] using cyclodextrins as chiral selectors, and by HPLC on polysaccharide-based chiral stationary phases (CSPs)[254]; the advantages of enantioselective separation methods over polarimetric methods for the determination of tetramisole enantiomers were also experimentally demonstrated[254].

In the following study, an enantioselective HPLC method has been validated and applied for the detection and determination of levamisole and tetramisole in cocaine samples in the presence of some of the more frequently used adulterants; a cellulose tris(3,5-dimethylphenylcarbamate) CSP was used in the normal-phase mode. To enhance the selectivity of the HPLC assay, an online HPLC–circular dichroism (CD) method was developed and used for the identification and determination of the elution order levamisole and dexamisole in seized cocaine

samples, in the presence of several adulterants. Indeed, the well-established hyphenation of enantioselective HPLC and CD detection[255-258] allows determining the stereochemistry of the eluted fractions with high detection selectivity; this feature is particularly important when dealing with complex matrices[80], as in the case of street samples of cocaine.

Results and Discussion

Enantioselective HPLC analysis

Enantioresolution of tetramisole enantiomers

The separation of tetramisole enantiomers was obtained on the Chiralcel OD-H column by using a mobile phase consisting of (n-hexane)–(2-propanol)–diethylamine (80:20:0.1, v/v/v) at a 0.7 mL min^{-1} flow rate. On the Lux Cellulose-1 column, the same mobile phase at a 1.4 mL min^{-1} flow rate ensured excellent Enantioresolution within 12 min. The elution order of the two enantiomers was established by injection of levamisole and tetramisole samples: dexamisole and levamisole were resolved with moderate enantioselectivity (α =1.18 on Chiralcel OD-H, 1.20 on Lux Cellulose-1). The tested columns have similar characteristics (same CSP, particle and column sizes) but different performances; the Lux Cellulose-1 column provided higher resolution and efficiency and was therefore chosen for the subsequent validation of the method. CD detection revealed a positive CD signal at 230 nm for dexamisole and a negative signal for levamisole (Fig. 40a).

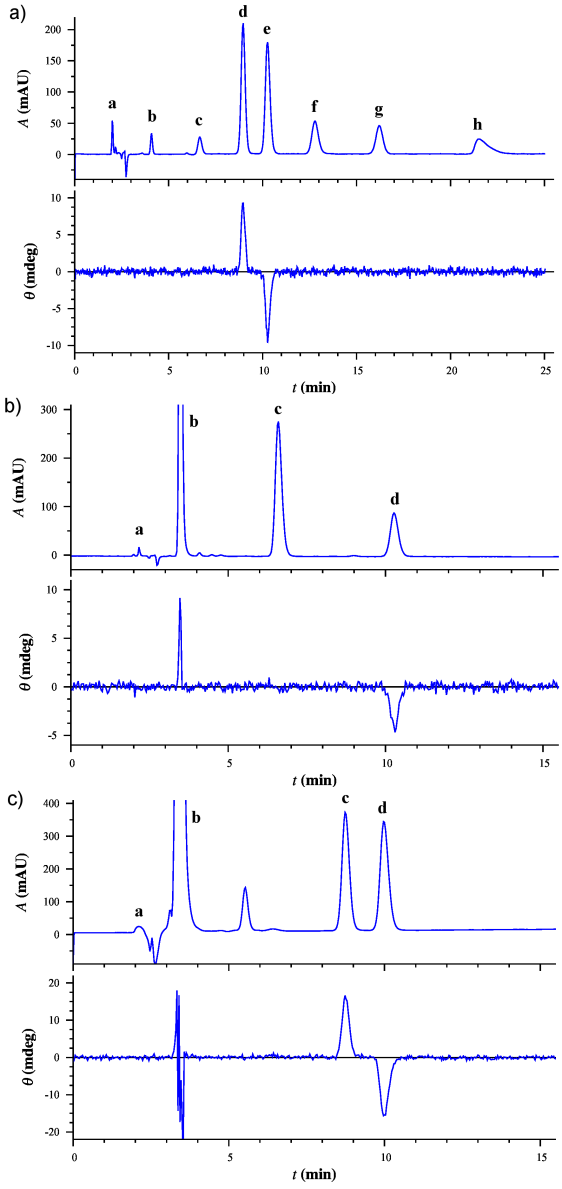

Figure 40 | UV (absorbance A in mAU) and CD (ellipticity in mdeg) chromatograms for the enantioselective HPLC analysis of tetramisole. (**a)** standard mix of tetramisole and common adulterantc found in street cocaine samples. (**b**) seized street cocaine sample containing levamisole (X_3). (**c**) seized street cocaine sample containing tetramisole (X_1). Analytes: a: levamisole; b: dexamisole; c: solvent; d: cocaine; e: lidocaine; f: norcocaine; g: phenacetin; h: procaine; i: benzocaine; j: caffeine. Details of HPLC condition in material and methods.

Method validation

The developed enantioselective HPLC method shows appropriate separation selectivity: cocaine, norcocaine, lidocaine, phenacetin, procaine, benzocaine and caffeine did not interfere with the elution times of tetramisole enantiomers (Fig. 40 a, and the Supporting Information of original articles). The calibration curve derived from the average peak areas for levamisole in the selected concentration range (a = 13.007; b = 9.763) provides satisfactory values of correlation and quality coefficients (r^2 = 0.9991; QC_{mean} = 3.094 %), and therefore the method shows a high degree of linearity. The resulting LOD and LOQ values (LOD = 0.84 g mL^{-1}; LOQ = 2.52 g mL^{-1}) are adequately low. Moreover, the method shows reasonable intra- assay precision (peak area RSD = 0.64%), inter-assay precision (peak area RSD = 1.16 %), and accuracy (average recovery: 101.71 %; RSD = 1.02 %); further details on the results obtained in validation assays are reported in the Supporting Information of the original article.

UV and CD spectroscopy

On-line UV and CD measurements showed a very simple spectroscopic behavior for tetramisole enantiomers: broad, mirror-image CD bands in the 270–220 nm region, positive for dexamisole and negative for levamisole, were observed. Off-line spectroscopic analysis on levamisole hydrochloride in 2-propanol showed a clear hypsochromic shift of the CD band with respect to the stopped-flow spectrum on levamisole, but the sign of the band is unchanged and the intensity is comparable (Fig. 41).

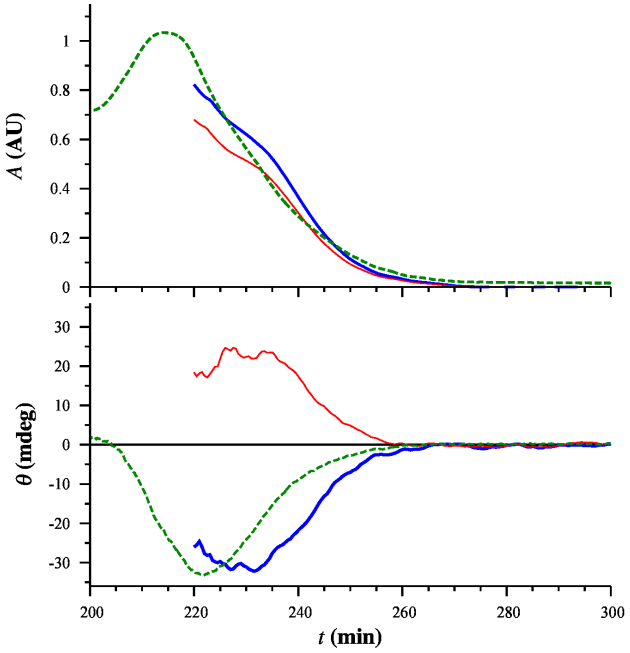

Figure 41 | On-line UV (absorbance A in AU) and CD (ellipticity in mdeg) spectra of levamisole (dark) and dexamisole (light), compared to the off-line spectra of levamisole hydrochloride in 2-propanol (dashed).

Street drug samples analysis

The presence of levamisole or tetramisole was observed in most of the seized cocaine samples analyzed; the quantitation of levamisole/tetramisole and cocaine for a limited set of seized cocaine samples containing levamisole or tetramisole is reported in Table 5.

Sample	Levamisole (wt%)	Tetramisole (wt%)	Cocaine (wt%)[a]
X_1	17.97		42.41
X_2	2.36		6.20
X_3		5.93	60.78
X_4		11.70	30.40

Table 5. Content of levamisole/tetramisole and cocaine in a set of street cocaine samples, given as percentage by weight (wt%). a. Determined with method reported in "Recommended Methods for the Identification and Analysis of Cocaine in Seized Materials (ST/NAR/7/REV.1), United Nations Office on Drugs and Crime (UNODC), Vienna, 2012".

Interestingly, the content in levamisole was extremely variable for the analyzed samples, irrespective of the content in pure cocaine. The CD detection system has a much higher selectivity with respect to diode array detection, since the monitoring is limited to chiral, non-racemic compounds. Figure 40a shows the CD and UV chromatographic profiles for the enantioselective HPLC analysis of a mixture of tetramisole and possible interfering analytes: under the adopted experimental conditions, only the two enantiomers of tetramisole are detected in the CD profile. The selectivity provided by CD detection was particularly useful when applied to street cocaine samples, allowing an easy monitoring of levamisole and dexamisole. The analyses of two seized cocaine samples are reported in Figure 40b and c, with both the UV and CD chromatographic profiles. One sample shows the presence of levamisole, being the only analyte monitored by the CD detection system (Fig. 40b), while the second sample shows the presence of tetramisole, as selectively monitored by CD (Fig. 40c).

Conclusions

An enantioselective HPLC method has been validated for the identification and determination of tetramisole enantiomers, levamisole and dexamisole, and then applied to the analysis of seized samples of cocaine. Most of the examined street samples showed the presence of levamisole or tetramisole: the content in adulterant was relatively high in some cases, when compared to the amount of pure cocaine in the illicit drug. The use of a CD detection system allowed to monitor levamisole and dexamisole with very high selectivity, even in the case of street cocaine samples, where several additional compounds are present. The usefulness of the method arises from the increasingly common use of both levamisole and tetramisole as adulterants in street cocaine: a reliable detection and determination of the two enantiomers of tetramisole is therefore essential to evaluate the health risks related to the composition of cocaine samples, to promote a deeper understanding on the causes of acute intoxications, and provide useful comparative information on the origin of seized samples.

Materials and methods

Materials

Compounds rac-6-phenyl-2,3,5,6-tetrahydroimidazo[2,1-b]- [1,3]thiazole hydrochloride (tetramisole), (−)-(S)-6-phenyl- 2,3,5,6-tetrahydroimidazo[2,1-b][1,3]thiazole hydrochloride (levamisole), N-(4-ethoxyphenyl)acetamide (phenacetin), 2-(diethylamino)-N-(2,6-dimethylphenyl)acetamide (lidocaine), 2-(diethylamino)ethyl 4-aminobenzoate hydrochloride (procaine), ethyl 4-aminobenzoate (benzocaine) and 3,7-dihydro-1,3,7- trimethyl-1H-purine-2,6-dione (caffeine) were purchased from Sigma–Aldrich (Milan, Italy). Analytical-grade solvents (n-hexane, 2-propanol, ethanol 99.7% and diethylamine) were purchased from Sigma–Aldrich (Milan, Italy). Stock solutions of analytes were prepared in ethanol at a 1.00 mg mL^{-1} concentration. The standard solutions used for method validation were prepared by dilution of stock solutions with mobile phase.

Enantioselective HPLC analysis

Instrumentation

The enantioselective HPLC analysis was carried out on a chromatographic system consisting of a Jasco (Tokyo, Japan) PU-980 HPLC pump, a MD-910 diode array detector, a LG-2080-02 ternary gradient unit, a DG-2080-53 degasser, a Jones (Lakewood, CO, USA) model 7955 HPLC column chiller, a Rheodyne 7725i syringe loading injector and a 20 L sample loop; a Chiralcel® OD-H column (CSP: cellulose tris(3,5-dimethylphenylcarbamate) coated on silica gel; 250 × 4.6 mm I.D., 5 m particle size; Daicel, Illkirch, France) and a LuxTM Cellulose-1 column (CSP: cellulose tris(3,5-dimethylphenylcarbamate) coated on silica gel; 250 × 4.6 mm I.D., 5 m particle size; Phenomenex, Castel Maggiore, Italy) were used. CD detection was implemented by connecting the system to a Jasco J-810 spectropolarimeter equipped with a 10 mm pathlength HPLC flow cell and a Rheodyne 7010 injector set up as a three-way valve for stopped-flow measurements. Single-wavelength chromatograms were recorded at 230 nm in both diode array and CD detection modes; CD detection was carried out using a 2s data pitch, a 5 nm spectral bandwidth and a 2 s time constant.

Chromatographic conditions

The enantioselective HPLC analysis was performed using a mobile phase consisting of a n-hexane–2-propanol mixture (80:20, v/v) in isocratic conditions; 0.1% (v/v) diethylamine was added to the mobile phase to neutralize the cationic forms of analytes and improve the chromatographic resolution. Constant flow rates (0.7 mL min^{-1} on Chiralcel OD-H column, 1.4 mL min^{-1} on Lux Cellulose-1) and column temperature (15° C) were used.

Method validation

The enantioselective HPLC method was validated using the Lux Cellulose-1 column and diode array detection. Selectivity was assessed by analysis of a 150 μg mL^{-1} standard solution of tetramisole hydrochloride; the relevant chromatographic parameters (capacity factor k, number of plates N, asymmetry factor A, selectivity α and resolution R) were determined according to the half-height method using the Jasco ChromNav software. Interference from other analytes was investigated by analysis of a mix of frequent adulterants found in street cocaine samples (lidocaine, phenacetin, procaine, benzocaine and caffeine) with tetramisole; different concentrations were used depending on the spectroscopic response of analytes at 230 nm. Capacity factors for cocaine and its metabolite norcocaine were derived from the chromatograms of analyzed street cocaine samples; their identity was confirmed by GC–MS analysis (Figs. S1–S3 in the Supporting Information of the original article) according to "Recommended Methods for the Identification and Analysis of Cocaine in Seized Materials (ST/NAR/7/REV.1), United Nations Office on Drugs and Crime (UNODC), Vienna, 2012". Linearity (n = 3) was evaluated by analyzing six standard sam- ples of levamisole hydrochloride (6.25, 9.375, 18.75, 37.5, 75 and 150 μg mL^{-1}); triplicate injections were performed for each solution. A calibration curve was obtained by plotting the peak areas (in mAU min) against the correspondent concentrations of neutral analyte (μg mL^{-1}) and applying a linear regression model ($y = a + bx$), for which the correlation coefficient (r^2) and the quality coefficient (QC_{mean}) were determined[259, 260]. Sensitivity was assessed by calculating the limit of detection (LOD) and limit of quantitation (LOQ) for levamisole from the calibration curve using the standard deviation of the y-intercept (s_a) and the slope (b) obtained by linear regression ($LOQ = 10s_a /b$; $LOD = LOQ/3$). Intra-assay and inter-assay precision (n = 6) was determined by repeated injections of a 75 g mL^{-1} standard solution of levamisole hydrochloride. The average capacity factors and peak areas, with the corresponding relative standard deviations (%RSD), were determined for both assays.

Accuracy (n = 3) was evaluated by spiking a 0.5 mg mL^{-1} solution of seized street cocaine powder (see next subsection for sample preparation) with three different concentrations (60, 75 and 90 g mL^{-1}) of levamisole hydrochloride; duplicate injections were performed for each sample. The average recoveries and relative standard deviation (% RSD) were determined for each concentration.

Street drug samples analysis

The validated HPLC method with diode array detection was applied to the analysis on samples of street cocaine powders (X_1–X_4) seized by Italian law enforcement agencies. Aliquots of 100 mg of finely ground samples were dissolved in ethanol by sonication to obtain a concentration of 10 mg mL^{-1}, diluted to 1 mg mL^{-1} with mobile phase and immediately injected in the HPLC system. The content of levamisole and tetramisole were determined by means of peak area interpolation with calibration curves and expressed as percentage by weight (wt %) of street cocaine sample.

UV and CD measurements

Off-line UV and CD spectra of levamisole hydrochloride (1 mM in 2-propanol) were recorded at 25° C in the 300–195 nm spectral range on a Jasco (Tokyo, Japan) J-810spectropolarimeter equipped with a PTC-423S Peltier-type temperature control system, using a 0.5 mm pathlength cell. Measurements were carried out at 0.2 nm intervals using a 2 nm spectral bandwidth, a 20 nm min^{-1} scan rate and a 2 s time constant. On-line UV and CD spectra of levamisole and dexamisole were recorded in the 300–220nm range by stopped-flow measurements, using a 0.5 nm data pitch, a 2 nm spectral bandwidth, a 200 nm min^{-1} scan rate and a 1 s time constant.

11. Conclusion and Perspective

Conclusion and future perspective

In the present dissertation, two spectroscopic analytical technologies – surface plasmon resonance (SPR) and circular dichroism (CD) – were described in term of detection principle, instrumentation available, experimental set-up and data analysis. Advantages and limitations of each approach are critically reviewed and their relevance for the field of pharmaceutical science is discussed. Description is complemented by a short presentation of the theory behind biological activity of exogenous and endogenous compounds in living organisms and the role that pharmaceutical analysis exerts in drug discovery. Then, few selected experimental applications of SPR and CD methodologies, carried out during the course of the PhD program, are illustrated and commented.

In particular, cross-species (human and rat) serum albumins binding for two naturally occurring triterpenoids, Cucurbitacin E and I (CucE and CucI) were evaluated in perspective of using the two compounds as therapeutics. The steady state and kinetic analysis of SPR sensorgrams for Cuc–serum albumins complexes unveiled a previously unreported binding event between CucI and human serum albumin (HSA), with CucI showing a 3-fold lower affinity than CucE. From K_D values measured all compounds were classified as high affinity binders for both serum albumins. However, both compounds bind slightly tighter to rat serum albumin (RSA) with respect to HSA. CD spectroscopic analysis showed that CucE and I are able to modulate the binding of biliverdin to serum albumins, as observed by the concentration-dependent change in intensity of the positive ICD band of biliverdin upon titration with cucurbitacin. Two different behaviors were detected, positive modulation for HSA and negative for RSA. Overall, the findings

suggested that a different *in vivo* action for CucE and I in the two different animal species could exist and it needs to be carefully assessed in translational medicine.

The binding of the pleiotropic gene regulator of *Helycobacter Pylori* NikR (*Hp*NikR) to the operator region of the urease promoter (OP_{ureA}) was investigated through an extended SPR experimental set-up in combination with isothermal titration calorimetry. An active surface bearing immobilized OP_{ureA} was prepared *via* affinity capture procedure and its functionality was extensively assessed. A kinetic analysis of the biorecognition event revealed an isomerization of the *Hp*NikR–OP_{ureA} complex occurring over time. After the first encounter between the two interactants to form the first complex, it undergoes a conformational rearrangement that in the presence of stoichiometric Nickel (II) ions in the environment leads to high-affinity binding. Combination of the new SPR data with previous NMR, light scattering and molecular dynamics simulations data was able to confirm that the stoichiometric presence of Ni(II) "unlock" *Hp*NikR structure and allows it to span the surrounding more efficiently in search of the dsDNA sequence. This behavior allows the bacteria to finely regulate expression of enzyme related to the Nickel homeostasis in response to high concentration of the metal in the environment.

The combination of enantioselective high performance liquid chromatography (HPLC), electronic circular dichroism (ECD) spectroscopy, and time-dependent density functional theory (TD-DFT) calculations was successfully employed to characterize the absolute stereochemistry of a trans-3-arylglycidic acid derivative. In perspective of using this natural building block as starting material for the production of polymers endowed with pharmaceutical activity it is essential to know its absolute configuration. In the present study the full stereochemical

characterization was achieved through the stopped-flow method. With this approach the fractions eluting from the HPLC were directly trapped into a tailor-made sample chamber and the CD spectra recorded in the 350–200 nm spectral range. With this method the step of collecting pure enantiomers and dry the solvent out was excluded, drastically reducing the likelihood of degradation for the collected fractions.

SPR competition assay was employed to monitor the inhibition capacity of a selected small molecule (BCI-121) towards an epigenetic regulator involved in several cancer malignancies, SMYD3. Through molecular docking techniques the methylation gorge of the enzyme was inspected and a molecule with suitable chemical scaffold was synthesized. The compound was tested on a selected cell line, and a concentration-dependent reduction of the proliferation of tumor cells was observed, indicating a potential therapeutic effect could exist. The mode of action for the drug was then tested *via* SPR assay, in which BCI-121 and SMYD3 natural substrate H4K5 were injected together over a SMYD3 bioactive surface. A lower SPR response was detected when the histone residue binds to the protein in the presence of BCI-121, suggesting that a competition for the same binding site could indeed take place and be the main mechanism of inhibition.

Combination of HPLC-CD and ECD spectroscopy was employed to determine the presence of two adulterants dexamisole and its enantiomer levamisole in seized street cocaine samples. The use of a CD detection system allowed monitoring levamisole and dexamisole with very high selectivity, even in the case of street cocaine samples, where several additional compounds are present. This practical method developed here provides a fast means to evaluate the health risks related to the composition of cocaine samples, to promote a deeper understanding on the

causes of acute intoxications and to provide useful comparative information on the origin of seized samples.

The selected applications of SPR and CD spectroscopies illustrated in the present dissertation serve as a small sample of all the possibilities that the two approaches provide.

It is important to stress that SPR and CD spectroscopies greatly benefit from their combination and synergy since the two techniques allow extrapolating complementary information on the same biological system; SPR can provide dynamic data on biorecognition events, while CD can provide conformational insight on the guest-host complex in solution.

They demand for different material consumption, as SPR can perform a whole analysis with few μg of both interactants while CD needs higher material consumption. Nonetheless, CD can provide valuable information on the conformation of complexes in solution and could, in principle, be used to "see" the conformational rearrangement indirectly measured with SPR assays. If spectroscopic properties are favorable the isomerization of a bimolecular complex could be follow in real-time as a change in optical activity, and the rate for the conformational rearrangement quantified and directly related to SPR measurements. Moreover, CD is solely based on light absorption of species in solution while SPR detection principle relies on specific adsorption phenomena at the surface of a sensor chip. Therefore, while the latter is not able to discern what causes refractivity change, the former will only produce signal upon specific binding, resulting in a highly selective detection method and a cleaner means to eventually extrapolate affinity constants.

As conclusive remarks, is important to note that the SPR assays developed during the course of the PhD program and presented in this thesis can serve as platform for inhibitor screening.

Regarding SMYD3 epigenetic regulator, the findings reported in this dissertation prompted further evaluation of molecules' libraries through SPR analysis. The experimental set-up was expanded and different isoforms of the enzyme were immobilized taking advantage of different chemistries. Other binding partners were tested for the binding to the protein and encouraging outcomes were used as a background research to apply, and subsequently obtain, a research grant from Italian Association for Cancer Research – AIRC (starting 2017).

The SPR assay developed for the monitoring of *Hp*NikR – OP_{ureA} interaction is, at best of my knowledge, the only SPR method to probe inhibition of protein–dsDNA binding, as this type of interactions were previously defined as undruggable. The competition assay employed to validate the protein–dsDNA recognition event, can be easily translated in an inhibition assay employing soluble molecules with potential therapeutic properties. If binding between *Hp*NikR and OP_{ureA} is prevented, key Nickel-related enzymes cannot be synthesized and considering that most of them are pathogenic factors for *Helycobacter Pylori*, this could result in a highly selective therapeutic effect.

12. Reference set

Reference set

1. Brownlee, M. Biochemistry and molecular cell biology of diabetic complications. *Nature* **414**, 813-820 (2001).
2. Sioutos, N. et al. NCI Thesaurus: a semantic model integrating cancer-related clinical and molecular information. *Journal of biomedical informatics* **40**, 30-43 (2007).
3. Manolio, T.A. et al. Finding the missing heritability of complex diseases. *Nature* **461**, 747-53 (2009).
4. Harvey, D. Analytical chemistry 2.0--an open-access digital textbook. *Anal Bioanal Chem* **399**, 149-52 (2011).
5. Petrovska, B.B. Historical review of medicinal plants' usage. *Pharmacogn Rev* **6**, 1-5 (2012).
6. Kaufmann, S.H. Paul Ehrlich: founder of chemotherapy. *Nat Rev Drug Discov* **7**, 373 (2008).
7. Schwartz, R.S. Paul Ehrlich's magic bullets. *N Engl J Med* **350**, 1079-80 (2004).
8. Stephenson, R.P. A modification of receptor theory. *Br J Pharmacol Chemother* **11**, 379-93 (1956).
9. Copeland, R.A., Pompliano, D.L. & Meek, T.D. Drug-target residence time and its implications for lead optimization. *Nat Rev Drug Discov* **5**, 730-9 (2006).
10. Copeland, R.A. The drug-target residence time model: a 10-year retrospective. *Nat Rev Drug Discov* **15**, 87-95 (2016).
11. Morrison, J.F. & Walsh, C.T. The behavior and significance of slow-binding enzyme inhibitors. *Adv Enzymol Relat Areas Mol Biol* **61**, 201-301 (1988).
12. Copeland, R.A. Evaluation of enzyme inhibitors in drug discovery. A guide for medicinal chemists and pharmacologists. *Methods Biochem Anal* **46**, 1-265 (2005).
13. Gooljarsingh, L.T. et al. A biochemical rationale for the anticancer effects of Hsp90 inhibitors: slow, tight binding inhibition by geldanamycin and its analogues. *Proc Natl Acad Sci U S A* **103**, 7625-30 (2006).
14. Tummino, P.J. & Copeland, R.A. Residence time of receptor-ligand complexes and its effect on biological function. *Biochemistry* **47**, 5481-92 (2008).
15. Schiele, F., Ayaz, P. & Fernandez-Montalvan, A. A universal homogeneous assay for high-throughput determination of binding kinetics. *Anal Biochem* **468**, 42-9 (2015).
16. Fabini, E., Zambelli, B., Mazzei, L., Ciurli, S. & Bertucci, C. Surface plasmon resonance and isothermal titration calorimetry to monitor the Ni(II)-dependent binding of Helicobacter pylori NikR to DNA. *Anal Bioanal Chem* **408**, 7971-7980 (2016).
17. Makrides, S.C. Strategies for achieving high-level expression of genes in Escherichia coli. *Microbiol Rev* **60**, 512-38 (1996).
18. Sørensen, H.P. & Mortensen, K.K. Advanced genetic strategies for recombinant protein expression in Escherichia coli. *Journal of Biotechnology* **115**, 113-128 (2005).
19. Rosano, G.L. & Ceccarelli, E.A. Recombinant protein expression in Escherichia coli: advances and challenges. *Front Microbiol* **5**, 172 (2014).
20. Banker, M.J., Clark, T.H. & Williams, J.A. Development and validation of a 96-well equilibrium dialysis apparatus for measuring plasma protein binding. *J Pharm Sci* **92**, 967-74 (2003).
21. Waters, N.J., Jones, R., Williams, G. & Sohal, B. Validation of a rapid equilibrium dialysis approach for the measurement of plasma protein binding. *J Pharm Sci* **97**, 4586-95 (2008).

22. Jacobson, D.R. & Saleh, O.A. Quantifying the ion atmosphere of unfolded, single-stranded nucleic acids using equilibrium dialysis and single-molecule methods. *Nucleic Acids Research* **44**, 3763-3771 (2016).
23. Liu, J., Andya, J.D. & Shire, S.J. A critical review of analytical ultracentrifugation and field flow fractionation methods for measuring protein aggregation. *AAPS J* **8**, E580-9 (2006).
24. Cole, J.L. Methods in Enzymology. Analytical Ultracentrifugation. Preface. *Methods Enzymol* **562**, xix-xx (2015).
25. Cohen, L.H. Plasma protein-binding methods in drug discovery. *Optimization in Drug Discovery: In Vitro Methods*, 111-122 (2004).
26. Quaglia, M. & De Lorenzi, E. Capillary electrophoresis in drug discovery. *Methods Mol Biol* **572**, 189-202 (2009).
27. Espada, A. & Molina-Martin, M. Capillary electrophoresis and small molecule drug discovery: a perfect match? *Drug Discov Today* **17**, 396-404 (2012).
28. Pellecchia, M., Sem, D.S. & Wuthrich, K. NMR in drug discovery. *Nat Rev Drug Discov* **1**, 211-9 (2002).
29. Pellecchia, M. et al. Perspectives on NMR in drug discovery: a technique comes of age. *Nat Rev Drug Discov* **7**, 738-45 (2008).
30. Simmler, C., Napolitano, J.G., McAlpine, J.B., Chen, S.N. & Pauli, G.F. Universal quantitative NMR analysis of complex natural samples. *Curr Opin Biotechnol* **25**, 51-9 (2014).
31. Wallace, B.A. & Janes, R.W. Circular dichroism and synchrotron radiation circular dichroism spectroscopy: tools for drug discovery. *Biochem Soc Trans* **31**, 631-3 (2003).
32. Zhang, Y., Watts, W., Nogle, L. & McConnell, O. Rapid method development for chiral separation in drug discovery using multi-column parallel screening and circular dichroism signal pooling. *J Chromatogr A* **1049**, 75-84 (2004).
33. Bertucci, C., Pistolozzi, M. & De Simone, A. Circular dichroism in drug discovery and development: an abridged review. *Anal Bioanal Chem* **398**, 155-66 (2010).
34. Wesolowski, S.S. & Pivonka, D.E. A rapid alternative to X-ray crystallography for chiral determination: case studies of vibrational circular dichroism (VCD) to advance drug discovery projects. *Bioorg Med Chem Lett* **23**, 4019-25 (2013).
35. Burke, T.J., Loniello, K.R., Beebe, J.A. & Ervin, K.M. Development and application of fluorescence polarization assays in drug discovery. *Comb Chem High Throughput Screen* **6**, 183-94 (2003).
36. Hesterkamp, T., Barker, J., Davenport, A. & Whittaker, M. Fragment based drug discovery using fluorescence correlation: spectroscopy techniques: challenges and solutions. *Curr Top Med Chem* **7**, 1582-91 (2007).
37. Martinez, N.J., Titus, S.A., Wagner, A.K. & Simeonov, A. High-throughput fluorescence imaging approaches for drug discovery using in vitro and in vivo three-dimensional models. *Expert Opin Drug Discov* **10**, 1347-61 (2015).
38. Tian, L., Wei, W. & Mao, Y. Kinetic studies of the interaction between antitumor antibiotics and DNA using quartz crystal microbalance. *Clin Biochem* **37**, 120-7 (2004).
39. Fee, C.J. Label-free, real-time interaction and adsorption analysis 2: quartz crystal microbalance. *Methods Mol Biol* **996**, 313-22 (2013).
40. Bertucci, C., Pistolozzi, M., Felix, G. & Danielson, U.H. HSA binding of HIV protease inhibitors: a high-performance affinity chromatography study. *J Sep Sci* **32**, 1625-31 (2009).

41. Vuignier, K., Guillarme, D., Veuthey, J.L., Carrupt, P.A. & Schappler, J. High performance affinity chromatography (HPAC) as a high-throughput screening tool in drug discovery to study drug-plasma protein interactions. *J Pharm Biomed Anal* **74**, 205-12 (2013).
42. Rowland, R.S. Using X-ray crystallography in drug discovery. *Curr Opin Drug Discov Devel* **5**, 613-9 (2002).
43. Zheng, H. et al. X-ray crystallography over the past decade for novel drug discovery - where are we heading next? *Expert Opin Drug Discov* **10**, 975-89 (2015).
44. Wright, P. et al. Evolution of an open-access quantitative bioanalytical mass spectrometry service in a drug discovery environment. *Biomed Chromatogr* **20**, 585-96 (2006).
45. Pacholarz, K.J., Garlish, R.A., Taylor, R.J. & Barran, P.E. Mass spectrometry based tools to investigate protein-ligand interactions for drug discovery. *Chem Soc Rev* **41**, 4335-55 (2012).
46. Pedro, L. & Quinn, R.J. Native Mass Spectrometry in Fragment-Based Drug Discovery. *Molecules* **21** (2016).
47. Hura, G.L. et al. Robust, high-throughput solution structural analyses by small angle X-ray scattering (SAXS). *Nat Methods* **6**, 606-12 (2009).
48. Lange, K., Blaess, G., Voigt, A., Gotzen, R. & Rapp, M. Integration of a surface acoustic wave biosensor in a microfluidic polymer chip. *Biosens Bioelectron* **22**, 227-32 (2006).
49. Cooper, M.A. Optical biosensors in drug discovery. *Nature reviews Drug discovery* **1**, 515-528 (2002).
50. Danielson, U.H. Integrating surface plasmon resonance biosensor-based interaction kinetic analyses into the lead discovery and optimization process. *Future Med Chem* **1**, 1399-414 (2009).
51. Singh, P. SPR Biosensors: Historical Perspectives and Current Challenges. *Sensors and Actuators B-Chemical* **229**, 110-130 (2016).
52. Ward, W.H. & Holdgate, G.A. Isothermal titration calorimetry in drug discovery. *Prog Med Chem* **38**, 309-76 (2001).
53. Keller, S. et al. High-precision isothermal titration calorimetry with automated peak-shape analysis. *Anal Chem* **84**, 5066-73 (2012).
54. Linkuviene, V., Krainer, G., Chen, W.Y. & Matulis, D. Isothermal titration calorimetry for drug design: Precision of the enthalpy and binding constant measurements and comparison of the instruments. *Anal Biochem* **515**, 61-64 (2016).
55. Stewart, P.L. Integrating cryo-electron microscopy into drug-design strategies. *Trends Biotechnol* **12**, 429-31 (1994).
56. Merino, F. & Raunser, S. Electron Cryo-microscopy as a Tool for Structure-Based Drug Development. *Angew Chem Int Ed Engl* (2016).
57. Wienken, C.J., Baaske, P., Rothbauer, U., Braun, D. & Duhr, S. Protein-binding assays in biological liquids using microscale thermophoresis. *Nat Commun* **1**, 100 (2010).
58. Seidel, S.A. et al. Microscale thermophoresis quantifies biomolecular interactions under previously challenging conditions. *Methods* **59**, 301-15 (2013).
59. Dau, T. et al. Quantitative analysis of protease recognition by inhibitors in plasma using microscale thermophoresis. *Sci Rep* **6**, 35413 (2016).
60. Folmer, R.H. Integrating biophysics with HTS-driven drug discovery projects. *Drug Discov Today* **21**, 491-8 (2016).
61. Renaud, J.P. et al. Biophysics in drug discovery: impact, challenges and opportunities. *Nat Rev Drug Discov* **15**, 679-98 (2016).

62. Bohacek, R.S. & McMartin, C. Modern computational chemistry and drug discovery: structure generating programs. *Curr Opin Chem Biol* **1**, 157-61 (1997).
63. Rabal, O., Urbano-Cuadrado, M. & Oyarzabal, J. Computational medicinal chemistry in fragment-based drug discovery: what, how and when. *Future Med Chem* **3**, 95-134 (2011).
64. Desai, P.V. The integration of computational chemistry during drug discovery to drive decisions: are we there yet? *Future Med Chem* **8**, 1717-20 (2016).
65. Fischer, P.M. Computational chemistry approaches to drug discovery in signal transduction. *Biotechnol J* **3**, 452-70 (2008).
66. Tedesco, D. & Bertucci, C. Induced circular dichroism as a tool to investigate the binding of drugs to carrier proteins: Classic approaches and new trends. *J Pharm Biomed Anal* **113**, 34-42 (2015).
67. Goodmans, L. Theory and Applications of Ultraviolet Spectroscopy. *Journal of the American Chemical Society* **85**, 4056-4057 (1963).
68. Drake, A.F. The measurement of electronic absorption spectra in the ultraviolet and visible. *Methods Mol Biol* **22**, 173-82 (1994).
69. Harvey, D. Modern analytical chemistry (McGraw-Hill New York, 2000).
70. Sathyanarayana, D.N. Electronic absorption spectroscopy and related techniques. **Universities Press: Hyderabad**, 209–237 (2001).
71. Korger, J. et al. The polarization properties of a tilted polarizer. *Opt Express* **21**, 27032-42 (2013).
72. Drake, A.F. Optical spectroscopy. Principles and instrumentation. *Methods Mol Biol* **22**, 151-71 (1994).
73. Drake, A.F. Circular dichroism. *Methods Mol Biol* **22**, 219-44 (1994).
74. Masson, J.B. & Gallot, G. Terahertz achromatic quarter-wave plate. *Opt Lett* **31**, 265-7 (2006).
75. Drake, A.F., Harding, S.E. & Chowdhry, B.Z. Protein Ligand Interactions: Structure and Spectroscopy. *Eds.; Oxford University* (2001).
76. Brittain, H.G. Applications of chiroptical spectroscopy for the characterization of pharmaceutical compounds. *J Pharm Biomed Anal* **17**, 933-40 (1998).
77. Arvinte, T. et al. The multi-mode polarization modulation spectrometer: part 1: simultaneous detection of absorption, turbidity, and optical activity. *Analytical biochemistry* **332**, 46-57 (2004).
78. Nina Berova, K.N., Robert W. Woody. Circular Dichroism: Principles and Applications, 2nd Edition (Wiley, 2001).
79. Kelly, S.M., Jess, T.J. & Price, N.C. How to study proteins by circular dichroism. *Biochimica et Biophysica Acta (BBA)-Proteins and Proteomics* **1751**, 119-139 (2005).
80. Bertucci, C. & Tedesco, D. Advantages of electronic circular dichroism detection for the stereochemical analysis and characterization of drugs and natural products by liquid chromatography. *J Chromatogr A* **1269**, 69-81 (2012).
81. Bertucci, C. et al. Determination of levamisole and tetramisole in seized cocaine samples by enantioselective high-performance liquid chromatography and circular dichroism detection. *J Chromatogr A* **1363**, 150-4 (2014).
82. Tedesco, D. et al. Stopped-Flow Enantioselective HPLC-CD Analysis and TD-DFT Stereochemical Characterization of Methyl Trans-3-(3,4-Dimethoxyphenyl)Glycidate. *Chirality* **27**, 914-8 (2015).
83. Francotte, E.R. Enantioselective chromatography as a powerful alternative for the preparation of drug enantiomers. *Journal of Chromatography A* **906**, 379-397 (2001).

84. Berova N., P.P.L., Nakanishi K., Woody R.W. Comprehensive chiroptical spectroscopy vol. 1. (Hoboken, NJ: John Wiley & Sons, 2012).
85. Sreerama, N. & Woody, R.W. Protein secondary structure from circular dichroism spectroscopy. Combining variable selection principle and cluster analysis with neural network, ridge regression and self-consistent methods. *J Mol Biol* **242**, 497-507 (1994).
86. Kelly, S.M. & Price, N.C. The use of circular dichroism in the investigation of protein structure and function. *Curr Protein Pept Sci* **1**, 349-84 (2000).
87. Greenfield, N.J. Using circular dichroism spectra to estimate protein secondary structure. *Nature protocols* **1**, 2876-2890 (2006).
88. Barrow, C.J., Yasuda, A., Kenny, P.T. & Zagorski, M.G. Solution conformations and aggregational properties of synthetic amyloid beta-peptides of Alzheimer's disease. Analysis of circular dichroism spectra. *J Mol Biol* **225**, 1075-93 (1992).
89. Khan, M.Q. et al. Prion disease susceptibility is affected by beta-structure folding propensity and local side-chain interactions in PrP. *Proc Natl Acad Sci U S A* **107**, 19808-13 (2010).
90. Chiti, F. & Dobson, C.M. Amyloid formation by globular proteins under native conditions. *Nat Chem Biol* **5**, 15-22 (2009).
91. Allenmark, S. Induced circular dichroism by chiral molecular interaction. *Chirality* **15**, 409-22 (2003).
92. Zsila, F., Bikádi, Z. & Simonyi, M. Induced circular dichroism spectra reveal binding of the antiinflammatory curcumin to human α 1-acid glycoprotein. *Bioorganic & medicinal chemistry* **12**, 3239-3245 (2004).
93. Zsila, F. & Iwao, Y. The drug binding site of human alpha1-acid glycoprotein: insight from induced circular dichroism and electronic absorption spectra. *Biochim Biophys Acta* **1770**, 797-809 (2007).
94. Fabini, E., Fiori, G.M., Tedesco, D., Lopes, N.P. & Bertucci, C. Surface plasmon resonance and circular dichroism characterization of cucurbitacins binding to serum albumins for early pharmacokinetic profiling. *J Pharm Biomed Anal* **122**, 166-72 (2016).
95. Knoll, W. Interfaces and thin films as seen by bound electromagnetic waves. *Annu Rev Phys Chem* **49**, 569-638 (1998).
96. Barnes, W.L., Dereux, A. & Ebbesen, T.W. Surface plasmon subwavelength optics. *Nature* **424**, 824-30 (2003).
97. Liedberg, B., Nylander, C. & Lundstrom, I. Biosensing with surface plasmon resonance--how it all started. *Biosens Bioelectron* **10**, i-ix (1995).
98. Jonsson, U. et al. Real-time biospecific interaction analysis using surface plasmon resonance and a sensor chip technology. *Biotechniques* **11**, 620-7 (1991).
99. Hahnefeld, C., Drewianka, S. & Herberg, F.W. Determination of kinetic data using surface plasmon resonance biosensors. *Methods Mol Med* **94**, 299-320 (2004).
100. Di Primo, C. & Lebars, I. Determination of refractive index increment ratios for protein-nucleic acid complexes by surface plasmon resonance. *Anal Biochem* **368**, 148-55 (2007).
101. Homola, J., Yee, S.S. & Gauglitz, G. Surface plasmon resonance sensors: review. *Sensors and Actuators B: Chemical* **54**, 3-15 (1999).
102. Guo, X. Surface plasmon resonance based biosensor technique: a review. *J Biophotonics* **5**, 483-501 (2012).
103. Spoto, G. & Minunni, M. Surface Plasmon Resonance Imaging: What Next? *J Phys Chem Lett* **3**, 2682-91 (2012).

104. Wang, X., Zhan, S., Huang, Z. & Hong, X. REVIEW: ADVANCES AND APPLICATIONS OF SURFACE PLASMON RESONANCE BIOSENSING INSTRUMENTATION. *Instrumentation Science & Technology* **41**, 574-607 (2013).
105. Anker, J.N. et al. Biosensing with plasmonic nanosensors. *Nature Materials* **7**, 442-453 (2008).
106. Puiu, M. & Bala, C. SPR and SPR imaging: Recent trends in developing nanodevices for detection and real-time monitoringof biomolecular events. *Sensors (Switzerland)* **16** (2016).
107. Jason-Moller, L., Murphy, M. & Bruno, J. Overview of Biacore systems and their applications. *Curr Protoc Protein Sci* **Chapter 19**, Unit 19 13 (2006).
108. Rich, R.L. et al. A global benchmark study using affinity-based biosensors. *Anal Biochem* **386**, 194-216 (2009).
109. Chavanieu, A. & Pugnière, M. Developments in SPR Fragment Screening. *Expert Opinion on Drug Discovery* **11**, 489-499 (2016).
110. Löfås, S. & McWhirter, A. in Surface Plasmon Resonance Based Sensors (ed. Homola, J.) 117-151 (Springer Berlin Heidelberg, Berlin, Heidelberg, 2006).
111. Wear, M.A. et al. A surface plasmon resonance-based assay for small molecule inhibitors of human cyclophilin A. *Anal Biochem* **345**, 214-26 (2005).
112. Nordstrom, H. et al. Identification of MMP-12 inhibitors by using biosensor-based screening of a fragment library. *J Med Chem* **51**, 3449-59 (2008).
113. Myszka, D.G. Improving biosensor analysis. *J Mol Recognit* **12**, 279-84 (1999).
114. Karlsson, R., Katsamba, P.S., Nordin, H., Pol, E. & Myszka, D.G. Analyzing a kinetic titration series using affinity biosensors. *Anal Biochem* **349**, 136-47 (2006).
115. Rich, R.L. & Myszka, D.G. Survey of the year 2007 commercial optical biosensor literature. *J Mol Recognit* **21**, 355-400 (2008).
116. Rich, R.L. & Myszka, D.G. Grading the commercial optical biosensor literature-Class of 2008: 'The Mighty Binders'. *J Mol Recognit* **23**, 1-64 (2010).
117. Rich, R.L. & Myszka, D.G. Survey of the 2009 commercial optical biosensor literature. *J Mol Recognit* **24**, 892-914 (2011).
118. Rich, R.L., Day, Y.S., Morton, T.A. & Myszka, D.G. High-resolution and high-throughput protocols for measuring drug/human serum albumin interactions using BIACORE. *Anal Biochem* **296**, 197-207 (2001).
119. Geitmann, M. & Danielson, U.H. Studies of substrate-induced conformational changes in human cytomegalovirus protease using optical biosensor technology. *Anal Biochem* **332**, 203-14 (2004).
120. Geitmann, M. & Danielson, U.H. Additional level of information about complex interaction between non-nucleoside inhibitor and HIV-1 reverse transcriptase using biosensor-based thermodynamic analysis. *Bioorg Med Chem* **15**, 7344-54 (2007).
121. Seeger, C., Gorny, X., Reddy, P.P., Seidenbecher, C. & Danielson, U.H. Kinetic and mechanistic differences in the interactions between caldendrin and calmodulin with AKAP79 suggest different roles in synaptic function. *Journal of Molecular Recognition* **25**, 495-503 (2012).
122. Jayaprakasam, B., Seeram, N.P. & Nair, M.G. Anticancer and antiinflammatory activities of cucurbitacins from Cucurbita andreana. *Cancer Lett* **189**, 11-6 (2003).
123. Chen, J.C., Chiu, M.H., Nie, R.L., Cordell, G.A. & Qiu, S.X. Cucurbitacins and cucurbitane glycosides: structures and biological activities. *Nat Prod Rep* **22**, 386-99 (2005).

124. Yuan, G., Wahlqvist, M.L., He, G., Yang, M. & Li, D. Natural products and anti-inflammatory activity. *Asia Pac J Clin Nutr* **15**, 143-52 (2006).
125. Lee, D.H., Iwanski, G.B. & Thoennissen, N.H. Cucurbitacin: ancient compound shedding new light on cancer treatment. *ScientificWorldJournal* **10**, 413-8 (2010).
126. Duncan, K.L., Duncan, M.D., Alley, M.C. & Sausville, E.A. Cucurbitacin E-induced disruption of the actin and vimentin cytoskeleton in prostate carcinoma cells. *Biochem Pharmacol* **52**, 1553-60 (1996).
127. Dong, Y. et al. Cucurbitacin E, a tetracyclic triterpenes compound from Chinese medicine, inhibits tumor angiogenesis through VEGFR2-mediated Jak2-STAT3 signaling pathway. *Carcinogenesis* **31**, 2097-104 (2010).
128. van Kester, M.S. et al. Cucurbitacin I inhibits Stat3 and induces apoptosis in Sezary cells. *J Invest Dermatol* **128**, 1691-5 (2008).
129. Jeong, M.H. et al. Cucurbitacin I Attenuates Cardiomyocyte Hypertrophy via Inhibition of Connective Tissue Growth Factor (CCN2) and TGF- beta/Smads Signalings. *PLoS One* **10**, e0136236 (2015).
130. Peters, T. All about albumin : biochemistry, genetics, and medical applications (Academic Press, San Diego, 1996).
131. Sudlow, G., Birkett, D.J. & Wade, D.N. The characterization of two specific drug binding sites on human serum albumin. *Mol Pharmacol* **11**, 824-32 (1975).
132. Sudlow, G., Birkett, D.J. & Wade, D.N. Further characterization of specific drug binding sites on human serum albumin. *Mol Pharmacol* **12**, 1052-61 (1976).
133. Noctor, T.A.G., Diaz-Perez, M.J. & Wainer, I.W. Use of a human serum albumin-based stationary phase for high-performance liquid chromatography as a tool for the rapid determination of drug-plasma protein binding. *Journal of pharmaceutical sciences* **82**, 675-676 (1993).
134. Vuignier, K., Schappler, J., Veuthey, J.-L., Carrupt, P.-A. & Martel, S. Drug–protein binding: a critical review of analytical tools. *Analytical and bioanalytical chemistry* **398**, 53-66 (2010).
135. S Hage, D. et al. Characterization of drug interactions with serum proteins by using high-performance affinity chromatography. *Current drug metabolism* **12**, 313-328 (2011).
136. Ascoli, G.A., Domenici, E. & Bertucci, C. Drug binding to human serum albumin: Abridged review of results obtained with high-performance liquid chromatography and circular dichroism. *Chirality* **18**, 667-679 (2006).
137. Zsila, F., Bikadi, Z., Fitos, I. & Simonyi, M. Probing protein binding sites by circular dichroism spectroscopy. *Curr Drug Discov Technol* **1**, 133-53 (2004).
138. Frostell-Karlsson, Å. et al. Biosensor analysis of the interaction between immobilized human serum albumin and drug compounds for prediction of human serum albumin binding levels. *Journal of medicinal chemistry* **43**, 1986-1992 (2000).
139. Bertucci, C., Piccoli, A. & Pistolozzi, M. Optical biosensors as a tool for early determination of absorption and distribution parameters of lead candidates and drugs. *Combinatorial chemistry & high throughput screening* **10**, 433-440 (2007).
140. De Simone, A. et al. Surface plasmon resonance, fluorescence, and circular dichroism studies for the characterization of the binding of BACE-1 inhibitors. *Analytical and bioanalytical chemistry* **405**, 827-835 (2013).
141. Fortugno, C., van der Gronde, T., Varchi, G., Guerrini, A. & Bertucci, C. Species-dependent binding of new synthesized bicalutamide analogues to albumin by optical biosensor analysis. *Journal of pharmaceutical and biomedical analysis* **111**, 324-332 (2015).

142. Rich, R.L. & Myszka, D.G. Advances in surface plasmon resonance biosensor analysis. *Current opinion in biotechnology* **11**, 54-61 (2000).
143. Myszka, D.G. & Rich, R.L. Implementing surface plasmon resonance biosensors in drug discovery. *Pharmaceutical science & technology today* **3**, 310-317 (2000).
144. Zhang, D., Luo, G., Ding, X. & Lu, C. Preclinical experimental models of drug metabolism and disposition in drug discovery and development. *Acta Pharmaceutica Sinica B* **2**, 549-561 (2012).
145. Lien, E.A., Solheim, E. & Ueland, P.M. Distribution of tamoxifen and its metabolites in rat and human tissues during steady-state treatment. *Cancer Res* **51**, 4837-44 (1991).
146. Frostell-Karlsson, A. et al. Biosensor analysis of the interaction between immobilized human serum albumin and drug compounds for prediction of human serum albumin binding levels. *J Med Chem* **43**, 1986-92 (2000).
147. Herve, F., Rajkowski, K., Martin, M.T., Dessen, P. & Cittanova, N. Drug-binding properties of rat alpha 1-foetoprotein. Binding of warfarin, phenylbutazone, azapropazone, diazepam, digitoxin and cholic acid. *Biochem J* **221**, 401-6 (1984).
148. Abou-Khalil, R. et al. Interaction of cucurbitacins with human serum albumin: Thermodynamic characteristics and influence on the binding of site specific ligands. *J Photochem Photobiol B* **95**, 189-95 (2009).
149. Simonyi, M. in Comprehensive Chiroptical Spectroscopy 665-705 (John Wiley & Sons, Inc., 2012).
150. Zsila, F. Subdomain IB is the third major drug binding region of human serum albumin: toward the three-sites model. *Mol Pharm* **10**, 1668-82 (2013).
151. Greige-Gerges, H. et al. Effect of cucurbitacins on bilirubin-albumin binding in human plasma. *Life Sci* **80**, 579-85 (2007).
152. Bertucci, C. Enantioselective inhibition of the binding of rac-profens to human serum albumin induced by lithocholate. *Chirality* **13**, 372-8 (2001).
153. Zambelli, B. & Ciurli, S. Nickel and human health. *Met. Ions Life Sci.* **13**, 321-357 (2013).
154. Chivers, P.T. in Binding, Transport and Storage of Metal Ions in Biological Cells (eds. Maret, W. & Wedd, A.) 381-428 (The Royal Society of Chemistry, 2014).
155. Musiani, F., Zambelli, B., Bazzani, M., Mazzei, L. & Ciurli, S. Nickel-responsive transcriptional regulators. *Metallomics* **7**, 1305-1318 (2015).
156. van Vliet, A.H. et al. NikR mediates nickel-responsive transcriptional induction of urease expression in Helicobacter pylori. *Infect. Immun.* **70**, 2846-2852 (2002).
157. Muller, C. et al. Hierarchical regulation of the NikR-mediated nickel response in Helicobacter pylori. *Nucleic Acids Res.* **39**, 7564-7575 (2011).
158. van Vliet, A.H., Ernst, F.D. & Kusters, J.G. NikR-mediated regulation of *Helicobacter pylori* acid adaptation. *Trends Microbiol* **12**, 489-494 (2004).
159. Maroney, M.J. & Ciurli, S. Nonredox Nickel Enzymes. *Chem. Rev.* (2013).
160. Schreiter, E.R. et al. Crystal structure of the nickel-responsive transcription factor NikR. *Nat. Struct. Biol.* **10**, 794-799 (2003).
161. Chivers, P.T. & Tahirov, T.H. Structure of *Pyrococcus horikoshii* NikR: nickel sensing and implications for the regulation of DNA recognition. *J. Mol. Biol.* **348**, 597-607 (2005).
162. Dian, C. et al. Structural basis of the nickel response in *Helicobacter pylori*: crystal structures of HpNikR in Apo and nickel-bound states. *J. Mol. Biol.* **361**, 715-730 (2006).
163. Schreiter, E.R., Wang, S.C., Zamble, D.B. & Drennan, C.L. NikR-operator complex structure and the mechanism of repressor activation by metal ions. *Proc. Natl. Acad. Sci. U.S.A.* **103**, 13676-13681 (2006).

164. Phillips, C.M. et al. Structural Basis of the Metal Specificity for Nickel Regulatory Protein NikR. *Biochemistry* **47**, 1938-1946 (2008).
165. West, A.L. et al. Holo-Ni(II)*Hp*NikR is an asymmetric tetramer containing two different nickel-binding sites. *J. Am. Chem. Soc.* **132**, 14447-14456 (2010).
166. Benini, S., Cianci, M. & Ciurli, S. Holo-Ni2+ *Helicobacter pylori* NikR contains four square-planar nickel-binding sites at physiological pH. *Dalton Trans.* **40**, 7831-7833 (2011).
167. Kosikowska, P. & Berlicki, L. Urease inhibitors as potential drugs for gastric and urinary tract infections: a patent review. *Expert Opin Ther Pat* **21**, 945-57 (2011).
168. Yan, C. & Higgins, P.J. Drugging the undruggable: transcription therapy for cancer. *Biochim. Biophys. Acta* **1835**, 76-85 (2013).
169. Lazo, J.S. & Sharlow, E.R. Drugging Undruggable Molecular Cancer Targets. *Annu. Rev. Pharmacol. Toxicol.* **56**, 23-40 (2016).
170. Chan, L.L., Pineda, M., Heeres, J.T., Hergenrother, P.J. & Cunningham, B.T. A general method for discovering inhibitors of protein-DNA interactions using photonic crystal biosensors. *ACS Chem. Biol.* **3**, 437-48 (2008).
171. Alonso, N., Guillen, R., Chambers, J.W. & Leng, F. A rapid and sensitive high-throughput screening method to identify compounds targeting protein-nucleic acids interactions. *Nucleic Acids Res.* **43**, e52 (2015).
172. Rich, R.L. & Myszka, D.G. Higher-throughput, label-free, real-time molecular interaction analysis. *Analytical biochemistry* **361**, 1-6 (2007).
173. Nguyen, H.H., Park, J., Kang, S. & Kim, M. Surface plasmon resonance: a versatile technique for biosensor applications. *Sensors* **15**, 10481-10510 (2015).
174. Myszka, D.G. et al. The ABRF-MIRG'02 study: assembly state, thermodynamic, and kinetic analysis of an enzyme/inhibitor interaction. *Journal of biomolecular techniques: JBT* **14**, 247 (2003).
175. Geitmann, M. & Danielson, U.H. Studies of substrate-induced conformational changes in human cytomegalovirus protease using optical biosensor technology. *Analytical biochemistry* **332**, 203-214 (2004).
176. Nordström, H. et al. Identification of MMP-12 inhibitors by using biosensor-based screening of a fragment library. *Journal of medicinal chemistry* **51**, 3449-3459 (2008).
177. Wear, M.A. et al. A surface plasmon resonance-based assay for small molecule inhibitors of human cyclophilin A. *Analytical biochemistry* **345**, 214-226 (2005).
178. Peserico, A. et al. A SMYD3 Small-Molecule Inhibitor Impairing Cancer Cell Growth. *J Cell Physiol* **230**, 2447-60 (2015).
179. Ghai, R., Falconer, R.J. & Collins, B.M. Applications of isothermal titration calorimetry in pure and applied research--survey of the literature from 2010. *J Mol Recognit* **25**, 32-52 (2012).
180. Mazzei, L., Ciurli, S. & Zambelli, B. Hot biological catalysis: isothermal titration calorimetry to characterize enzymatic reactions. *J Vis Exp* (2014).
181. Hansen, L.D., Transtrum, M.K., Quinn, C. & Demarse, N. Enzyme-catalyzed and binding reaction kinetics determined by titration calorimetry. *Biochim Biophys Acta* **1860**, 957-66 (2016).
182. Burnouf, D. et al. kinITC: a new method for obtaining joint thermodynamic and kinetic data by isothermal titration calorimetry. *J. Am. Chem. Soc.* **134**, 559-565 (2012).
183. Dumas, P. et al. Extending ITC to Kinetics with kinITC. *Methods Enzymol* **567**, 157-80 (2016).

184. Guedich, S. et al. Quantitative and predictive model of kinetic regulation by E. coli TPP riboswitches. *RNA Biol* **13**, 373-90 (2016).
185. Davis, T.M. & David Wilson, W. in Methods in Enzymology 22-51 (Academic Press, 2001).
186. Zambelli, B. et al. High-affinity Ni2+ binding selectively promotes binding of Helicobacter pylori NikR to its target urease promoter. *J Mol Biol* **383**, 1129-43 (2008).
187. Seeger, C., Gorny, X., Reddy, P.P., Seidenbecher, C. & Danielson, U.H. Kinetic and mechanistic differences in the interactions between caldendrin and calmodulin with AKAP79 suggest different roles in synaptic function. *J Mol Recognit* **25**, 495-503 (2012).
188. Karlsson, R. & Falt, A. Experimental design for kinetic analysis of protein-protein interactions with surface plasmon resonance biosensors. *J Immunol Methods* **200**, 121-33 (1997).
189. Zambelli, B., Bellucci, M., Danielli, A., Scarlato, V. & Ciurli, S. The Ni2+ binding properties of Helicobacter pylori NikR. *Chem Commun (Camb)*, 3649-51 (2007).
190. Bahlawane, C. et al. Structural and mechanistic insights into Helicobacter pylori NikR activation. *Nucleic acids research* **38**, 3106-3118 (2010).
191. West, A.L. et al. Ni (II) coordination to mixed sites modulates DNA binding of HpNikR via a long-range effect. *Proceedings of the National Academy of Sciences* **109**, 5633-5638 (2012).
192. Musiani, F. et al. Computational Study of the DNA-Binding Protein Helicobacter pylori NikR: The Role of Ni2+ 2 2 Francesco Musiani and Branimir Bertoša contributed equally to the simulations presented here. *Journal of chemical theory and computation* **6**, 3503-3515 (2010).
193. Mazzei, L., Dobrovolska, O., Musiani, F., Zambelli, B. & Ciurli, S. On the interaction of Helicobacter pylori NikR, a Ni (II)-responsive transcription factor, with the urease operator: in solution and in silico studies. *JBIC Journal of Biological Inorganic Chemistry* **20**, 1021-1037 (2015).
194. de Mol, N.J. & Fischer, M.J.E. Surface plasmon resonance; methods and protocols (eds. de Mol, N.J. & Fischer, M.J.E.) (Springer, 2010).
195. Karlsson, R., Roos, H., Fägerstam, L. & Persson, B. Kinetic and Concentration Analysis Using BIA Technology. *Methods* **6**, 99-110 (1994).
196. Scheuermann, T.H. & Brautigam, C.A. High-precision, automated integration of multiple isothermal titration calorimetric thermograms: new features of NITPIC. *Methods* **76**, 87-98 (2015).
197. Kolb, H.C., VanNieuwenhze, M.S. & Sharpless, K.B. Catalytic asymmetric dihydroxylation. *Chemical Reviews* **94**, 2483-2547 (1994).
198. Plucińska, K., Kasprzykowski, F. & Kozian, E. Synthesis of enantiomerically pure forms of trans-3-phenylglycidic acid. *Tetrahedron letters* **38**, 861-864 (1997).
199. Veronese, F.M. & Mero, A. The impact of PEGylation on biological therapies. *BioDrugs* **22**, 315-329 (2008).
200. Nuyken, O. & Pask, S.D. Ring-opening polymerization—an introductory review. *Polymers* **5**, 361-403 (2013).
201. Barbakadze, V. et al. Poly [3-(3, 4-dihydroxyphenyl) glyceric acid], a new biologically active polymer from Symphytum asperum Lepech. and S. caucasicum Bieb.(Boraginaceae). *Molecules* **10**, 1135-1144 (2005).
202. Barbakadze, V., van den Berg, A.J.J., Beukelman, C.J., Kemmink, J. & van Ufford, H.C.Q. Poly [3-(3, 4-dihydroxyphenyl) glyceric acid] from Symphytum officinale roots and its biological activity. *Chemistry of natural compounds* **45**, 6-10 (2009).

203. Barbakadze, V. et al. Poly [3-(3, 4-dihydroxyphenyl) glyceric acid] from Anchusa italica roots. *Natural product communications* **5**, 1091-1095 (2010).
204. Barbakadze, V., Gogilashvili, L., Amiranashvili, L., Merlani, M. & Mulkijanyan, K. Novel biologically active phenolic polymers from different species of genera Symphytum and Anchusa (Boraginaceae). *J Chem Eng Chem Res* **1**, 47-53 (2014).
205. Merlani, M. et al. Ring-opening polymerization of a 2, 3-disubstituted oxirane leading to a polyether having a carbonyl–aromatic π-stacked structure. *Polym. Chem.* **6**, 1932-1936 (2015).
206. Li, J.J. Darzens glycidic ester condensation. *Name Reactions: A Collection of Detailed Reaction Mechanisms*, 183-184 (2006).
207. Tu, Y., Wang, Z.-X. & Shi, Y. An efficient asymmetric epoxidation method for trans-olefins mediated by a fructose-derived ketone. *Journal of the American Chemical Society* **118**, 9806-9807 (1996).
208. Bringmann, G., Gulder, T.A.M., Reichert, M. & Gulder, T. The online assignment of the absolute configuration of natural products: HPLC-CD in combination with quantum chemical CD calculations. *Chirality* **20**, 628-642 (2008).
209. Francotte, E.R. Enantioselective chromatography as a powerful alternative for the preparation of drug enantiomers. *Journal of Chromatography A* **906**, 379-397 (2001).
210. Autschbach, J. Computing chiroptical properties with first-principles theoretical methods: Background and illustrative examples. *Chirality* **21** (2009).
211. Goerigk, L., Kruse, H. & Grimme, S. Theoretical electronic circular dichroism spectroscopy of large organic and supramolecular systems. *Comprehensive Chiroptical Spectroscopy: Instrumentation, Methodologies, and Theoretical Simulations, Volume 1*, 643-673 (2012).
212. Lomsadze, K., Merlani, M., Barbakadze, V., Farkas, T. & Chankvetadze, B. Enantioseparation of chiral epoxides with polysaccharide-based chiral columns in HPLC. *Chromatographia* **75**, 839-845 (2012).
213. Irvine, C.A. et al. (Inc, 2002).
214. Frisch, M.J. et al. (Gaussian, Inc., Wallingford CT, 2009).
215. Grimme, S. Semiempirical GGA-type density functional constructed with a long-range dispersion correction. *Journal of computational chemistry* **27**, 1787-1799 (2006).
216. Tomasi, J., Mennucci, B. & Cances, E. The IEF version of the PCM solvation method: an overview of a new method addressed to study molecular solutes at the QM ab initio level. *Journal of Molecular Structure: THEOCHEM* **464**, 211-226 (1999).
217. Dunlap, B.I. Robust and variational fitting: Removing the four-center integrals from center stage in quantum chemistry. *Journal of Molecular Structure: THEOCHEM* **529**, 37-40 (2000).
218. Rappoport, D. & Furche, F. Property-optimized Gaussian basis sets for molecular response calculations. *The Journal of chemical physics* **133**, 134105 (2010).
219. Humphrey, W., Dalke, A. & Schulten, K. VMD: visual molecular dynamics. *Journal of molecular graphics* **14**, 33-38 (1996).
220. Perdew, J.P., Burke, K. & Ernzerhof, M. Generalized gradient approximation made simple. *Physical review letters* **77**, 3865 (1996).
221. Burke, K., Perdew, J.P. & Ernzerhof, M. Generalized Gradient Approximation Made Simple [Phys. Rev. Lett. 77, 3865 (1996)]. *Phys. Rev. Lett* **78**, 1396 (1997).
222. Adamo, C. & Barone, V. Toward reliable density functional methods without adjustable parameters: The PBE0 model. *The Journal of chemical physics* **110**, 6158-6170 (1999).

223. Stephens, P.J. & Harada, N. ECD cotton effect approximated by the Gaussian curve and other methods. *Chirality* **22**, 229-233 (2010).
224. Suganuma, T. & Workman, J.L. MAP kinases and histone modification. *J Mol Cell Biol* **4**, 348-50 (2012).
225. Klein, A.M., Zaganjor, E. & Cobb, M.H. Chromatin-tethered MAPKs. *Curr Opin Cell Biol* **25**, 272-7 (2013).
226. Copeland, R.A., Solomon, M.E. & Richon, V.M. Protein methyltransferases as a target class for drug discovery. *Nat Rev Drug Discov* **8**, 724-32 (2009).
227. Chi, P., Allis, C.D. & Wang, G.G. Covalent histone modifications--miswritten, misinterpreted and mis-erased in human cancers. *Nat Rev Cancer* **10**, 457-69 (2010).
228. Varier, R.A. & Timmers, H.T. Histone lysine methylation and demethylation pathways in cancer. *Biochim Biophys Acta* **1815**, 75-89 (2011).
229. Greer, E.L. & Shi, Y. Histone methylation: a dynamic mark in health, disease and inheritance. *Nat Rev Genet* **13**, 343-57 (2012).
230. Foreman, K.W. et al. Structural and functional profiling of the human histone methyltransferase SMYD3. *PLoS One* **6**, e22290 (2011).
231. Tsuge, M. et al. A variable number of tandem repeats polymorphism in an E2F-1 binding element in the 5' flanking region of SMYD3 is a risk factor for human cancers. *Nat Genet* **37**, 1104-7 (2005).
232. Mazur, P.K. et al. SMYD3 links lysine methylation of MAP3K2 to Ras-driven cancer. *Nature* **510**, 283-7 (2014).
233. Liu, Y. et al. SMYD3 overexpression was a risk factor in the biological behavior and prognosis of gastric carcinoma. *Tumour Biol* **36**, 2685-94 (2015).
234. Luo, X.G. et al. Histone methyltransferase SMYD3 promotes MRTF-A-mediated transactivation of MYL9 and migration of MCF-7 breast cancer cells. *Cancer Lett* **344**, 129-37 (2014).
235. Cock-Rada, A.M. et al. SMYD3 promotes cancer invasion by epigenetic upregulation of the metalloproteinase MMP-9. *Cancer Res* **72**, 810-20 (2012).
236. Hamamoto, R. et al. SMYD3 encodes a histone methyltransferase involved in the proliferation of cancer cells. *Nat Cell Biol* **6**, 731-40 (2004).
237. Zou, J.N. et al. Knockdown of SMYD3 by RNA interference down-regulates c-Met expression and inhibits cells migration and invasion induced by HGF. *Cancer Lett* **280**, 78-85 (2009).
238. Hamamoto, R. et al. Enhanced SMYD3 expression is essential for the growth of breast cancer cells. *Cancer Sci* **97**, 113-8 (2006).
239. Van Aller, G.S. et al. Smyd3 regulates cancer cell phenotypes and catalyzes histone H4 lysine 5 methylation. *Epigenetics* **7**, 340-3 (2012).
240. Kunizaki, M. et al. The lysine 831 of vascular endothelial growth factor receptor 1 is a novel target of methylation by SMYD3. *Cancer Res* **67**, 10759-65 (2007).
241. Kim, H. et al. Requirement of histone methyltransferase SMYD3 for estrogen receptor-mediated transcription. *J Biol Chem* **284**, 19867-77 (2009).
242. Biggar, K.K. & Li, S.S. Non-histone protein methylation as a regulator of cellular signalling and function. *Nat Rev Mol Cell Biol* **16**, 5-17 (2015).
243. Gaedcke, J. et al. Mutated KRAS results in overexpression of DUSP4, a MAP-kinase phosphatase, and SMYD3, a histone methyltransferase, in rectal carcinomas. *Genes Chromosomes Cancer* **49**, 1024-34 (2010).
244. Helin, K. & Dhanak, D. Chromatin proteins and modifications as drug targets. *Nature* **502**, 480-488 (2013).

245. Buchanan, J.A. & Lavonas, E.J. Agranulocytosis and other consequences due to use of illicit cocaine contaminated with levamisole. *Current opinion in hematology* **19**, 27-31 (2012).
246. Auffenberg, C., Rosenthal, L.J. & Dresner, N. Levamisole: a common cocaine adulterant with life-threatening side effects. *Psychosomatics* **54**, 590-593 (2013).
247. Tallarida, C.S., Tallarida, R.J. & Rawls, S.M. Levamisole enhances the rewarding and locomotor-activating effects of cocaine in rats. *Drug and alcohol dependence* **149**, 145-150 (2015).
248. Raymon, L.P. & Isenschmid, D.S. The possible role of levamisole in illicit cocaine preparations. *Journal of analytical toxicology* **33**, 620-622 (2009).
249. Bertol, E. et al. Determination of aminorex in human urine samples by GC–MS after use of levamisole. *Journal of pharmaceutical and biomedical analysis* **55**, 1186-1189 (2011).
250. Hofmaier, T. et al. Aminorex, a metabolite of the cocaine adulterant levamisole, exerts amphetamine like actions at monoamine transporters. *Neurochemistry international* **73**, 32-41 (2014).
251. Vanhoutte, P.M., Van Nueten, J.M., Verbeuren, T.J. & Laduron, P.M. Differential effects of the isomers of tetramisole on adrenergic neurotransmission in cutaneous veins of dog. *Journal of Pharmacology and Experimental Therapeutics* **200**, 127-140 (1977).
252. Casale, J.F., Colley, V.L. & LeGatt, D.F. Determination of Phenyltetrahydroimidazothiazole Enantiomers (Levamisole/Dexamisole) in Illicit Cocaine Seizures and in the Urine of Cocaine Abusers via Chiral Capillary Gas Chromatography–Flame-Ionization Detection: Clinical and Forensic Perspectives. *Journal of analytical toxicology* **36**, 130-135 (2012).
253. Doležalová, M. & Tkaczyková, M. LC determination of the enantiomeric purity of levamisole using stationary phase with bonded naphthylethylcarbamoylated-β-cyclodextrin. *Journal of pharmaceutical and biomedical analysis* **25**, 407-415 (2001).
254. Chankvetadze, B., Burjanadze, N., Santi, M., Massolini, G. & Blaschke, G. Enantioseparation of tetramisole by capillary electrophoresis and high performance liquid chromatography and application of these techniques to enantiomeric purity determination of a veterinary drug formulation of L-levamisole. *Journal of separation science* **25**, 733-740 (2002).
255. Drake, A.F., Grould, J.M. & Mason, S.F. Simultaneous monitoring of ligh-absorption and optical activity in the liquid chromatography of chiral substance. *Journal of Chromatography A* **202**, 239-245 (1980).
256. Salvadori, P., Bertucci, C. & Rosini, C. Circular dichroism detection in HPLC. *Chirality* **3**, 376-385 (1991).
257. Mannschreck, A. Chiroptical detection during liquid chromatography: applications to stereoanalysis and stereodynamics. *Chirality* **4**, 163-169 (1992).
258. Bertucci, C., Andrisano, V., Cavrini, V. & Castiglioni, E. Reliable assay of extreme enantiomeric purity values by a new circular dichroism based HPLC detection system. *Chirality* **12**, 84-92 (2000).
259. Van Loco, J., Elskens, M., Croux, C. & Beernaert, H. Linearity of calibration curves: use and misuse of the correlation coefficient. *Accreditation and Quality Assurance: Journal for Quality, Comparability and Reliability in Chemical Measurement* **7**, 281-285 (2002).
260. De Beer, J.O., De Beer, T.R. & Goeyens, L. Assessment of quality performance parameters for straight line calibration curves related to the spread of the abscissa values around their mean. *Analytica chimica acta* **584**, 57-65 (2007).

Contributions at National and International Conferences

Oral communications

1. "Surface plasmon resonance spectroscopy as a tool to investigate molecular recognition processes" **Edoardo Fabini**. Summer School Pharmaceutical Analysis – SSPA2016

2. "Cucurbitacins binding to serum albumins from different species: a surface plasmon resonance and circular dichroism study" **Edoardo Fabini**, G. M Lanchoti Fiori, D. Tedesco, N. P. Lopes and C. Bertucci. National Meeting Medicinal Chemistry 2016 – NMMC 2016

3. "Characterization of the Helycobacter Pylori NikR (*Hp*NikR) interaction with the promoter of the Urease Operon (ureOP) by Surface Plasmon Resonance based optical biosensor" **Edoardo Fabini**, D. Tedesco, L. Mazzei, B. Zambelli, S. Ciurli, C. Bertucci. Recent Development Pharmaceutical Analysis 2015 – RDPA 2015

Poster presentations

1. Naldi, M.; **Fabini, Edoardo**; Tedesco, D.; Baldassarre, M.; Domenicali, M.; Tramarin, A.; Caraceni, P. and Bertucci, C. "Characterization of high quality human serum albumin non-oncotic properties". National Meeting Medicinal Chemistry – NMMC (2016)

2. **Edoardo Fabini**, G. Lanchoti, D. Tedesco, Lopes N.P., C. Bertucci "A Surface Plasmon Resonance characterization of human and rat binding of albumins to cucurbitacins for the early ADMET profiling". Recent Development in Pharmaceutical Analysis – RDPA 2015 (2015)

3. **Edoardo Fabini**, Carlo Bertucci, Daniele Tedesco, Anna Maria Di Pietra, Francesca Rossi, Marco Garagnani, Elia Del Borrello, Vincenza Andrisano "Determination of levamisole and tetramisole in seized cocaine samples by enantioselective high-performance liquid chromatography and circular dichroism detection". XIV Giornata di Chimica dell'Emilia Romagna – XIV GdC (2014).

Medaglione

Dott. Edoardo Fabini

Supervisore: Prof. Carlo Bertucci

Dottorato: Scienze Biochimiche e Biotecnologiche, ciclo XXIX

Titolo tesi di Dottorato: Characterization of pharmaceutically relevant systems through surface plasmon resonance and circular dichroism spectroscopies

Il dott. Edoardo Fabini si è laureato in Chimica e Tecnologia Farmaceutiche (CTF) presso l'Università di Bologna nel 2013 con una tesi sulla preparazione e caratterizzazione di polimeri ad impronta molecolare svolta presso il Green Chemistry Center, Monash University, Melbourne, Australia.

Durante i tre anni di Dottorato in Scienze Biochimiche e Biotecnologiche, l'attività di ricerca del dott. Edoardo Fabini, si è rivolta allo studio di processi di riconoscimento molecolare di interesse in chimica farmaceutica. In particolare, l'attenzione del dottorando si è concentrata sull'utilizzo del biosensore ottico, basato sul fenomeno SPR (Surface Plasmon Resonance) in combinazione con la spettroscopia di dicroismo circolare elettronico (ECD) per la caratterizzazione del legame farmaco–proteina bersaglio e proteina–proteina.

I progetti svolti durante il triennio hanno portato i) alla caratterizzazione del legame di molecole farmacologicamente attive alla sieroalbumina, ii) allo sviluppo di metodi per lo screening di inibitori diretti contro importanti target farmacologici, quali SMYD3 e iii) alla caratterizzazione del legame, Ni(II) dipendente, di Helicobacter pylori NikR al DNA, fornendo in tutti i casi importanti informazioni sui meccanismi dei processi studiati. L'attività del dott. Fabini ha inoltre previsto la caratterizzazione stereochimica di vari composti di sintesi.

Nell'ambito del dottorato ha ottenuto un contributo con il progetto Marco Polo 2015 per un periodo di ricerca all'estero di sei mesi presso l'Università di Uppsala (Svezia), dove è stato ospite del gruppo di ricerca della Prof. Helena Danielson, svolgendo un progetto volto ad approfondire lo studio del sistema SMYD3 e ad ottimizzare il metodo di espressione e purificazione della proteina.

L'attività svolta si è finora concretizzata in 5 pubblicazioni su riviste internazionali (Journal of Chromatography A, Journal of Pharmaceutical and Biomedical Analalysis, Chirality, Analytical and Bioanalytical Chemistry, Journal of Cell Physiology) e 5 presentazioni in congressi nazionali e internazionali, di cui 3 comunicazioni orali (Recent Development in Pharmaceutical Analysis – RDPA 2015, National Meeting in Medicinal Chemistry – NMMC 2016, Summer School in Pharmaceutical Analysis – SSPA 2016).

Il dott. Fabini è risultato vincitore di 3 borse di studio: 2 borse della Società Chimica Italiana (SCI) per partecipazione a congressi e una borsa di studio nel merito del bando Unipharma-Graduates (bando 2016).

Nell'ambito del suo progetto di ricerca, il dottorando ha sviluppato una solida conoscenza delle tecniche spettroscopiche con particolare attenzione alla determinazione di parametri termodinamici e cinetici in processi di riconoscimento molecolare. Il dott. Fabini ha dimostrato ottime capacità di organizzazione del proprio lavoro ed ampia autonomia, riuscendo a sviluppare soluzioni originali ai problemi.

Oltre alle doti scientifiche, il dottorando ha dimostrato un'elevata attitudine al lavoro di gruppo e al trasferimento delle conoscenze, essendo correlatore di due tesi sperimentali di laurea in CTF; ha infine svolto attività didattica, ottenendo

cinque contratti di tutorato per i laboratori didattici di analisi farmaceutica del corso di studi in CTF.